University of Alberta

Helium Mixtures in 87% Porous Aerogel

by

Mark Paetkau

©

A thesis submitted to the Faculty of Graduate Studies and Research in partial fulfillment
of the requirements for the degree of Doctor of Philosophy

in

Low Temperature Physics
Department of Physics

Edmonton, Alberta
Spring, 1998

National Library
of Canada

Acquisitions and
Bibliographic Services

395 Wellington Street
Ottawa ON K1A 0N4
Canada

Bibliothèque nationale
du Canada

Acquisitions et
services bibliographiques

395, rue Wellington
Ottawa ON K1A 0N4
Canada

Your file Votre référence

Our file Notre référence

The author has granted a non-exclusive licence allowing the National Library of Canada to reproduce, loan, distribute or sell copies of this thesis in microform, paper or electronic formats.

The author retains ownership of the copyright in this thesis. Neither the thesis nor substantial extracts from it may be printed or otherwise reproduced without the author's permission.

L'auteur a accordé une licence non exclusive permettant à la Bibliothèque nationale du Canada de reproduire, prêter, distribuer ou vendre des copies de cette thèse sous la forme de microfiche/film, de reproduction sur papier ou sur format électronique.

L'auteur conserve la propriété du droit d'auteur qui protège cette thèse. Ni la thèse ni des extraits substantiels de celle-ci ne doivent être imprimés ou autrement reproduits sans son autorisation.

0-612-29088-3

Canada

University of Alberta

Faculty of Graduate Studies and Research

The undersigned certify that they have read, and recommend to the Faculty of Graduate Studies and Research for acceptance, a thesis entitled Helium Mixtures in 87% Porous Aerogel submitted by Mark Jeffrey Paetkau in partial fulfillment of the requirements for the degree of Doctor of Philosophy in Low Temperature Physics.

John Beamish

J. R. Beamish (Supervisor)

J. P. Franck

M. R. Freeman

J. A. Tuszynski

Arthur Mar

A. Mar

J. M. Parpia

Date: Oct. 10, 1997

DEDICATION

To Nicola and Owen, and in loving memory of Soren Blythe.

ABSTRACT

Ultrasonic velocity and attenuation measurements are used to study the phase separation of ^{3}He-^{4}He mixtures confined in a silica aerogel with a porosity of 87%. The superfluid transition is accompanied by a velocity increase due to decoupling and by a critical attenuation peak. At low ^{3}He concentrations (X), phase separation occurs at a temperature below the superfluid transition and causes systematic jumps in the velocity and hysteresis in both the velocity and attenuation. Analysis of the velocity jumps at phase separation suggest that they are due to the inertial coupling of ^{3}He atoms to the superfluid; the resulting effective mass is found to be $(2.5\pm0.2)m_3$ g/mol, in excellent agreement with calculations and measurements on bulk mixtures. At high ^{3}He concentrations, in contrast to measurements on higher porosity aerogel but in agreement with the bulk mixture phase diagram, there is only a single transition which displays the same characteristic signatures of the superfluid transition that occurs at low ^{3}He concentration (velocity increase due to decoupling and critical attenuation peak). While there is only a single transition in this concentration region, it is found to be different from phase separation in bulk mixtures which is a first order transition; a critical attenuation peak at the transition indicates it is a continuous (second order) transition. Furthermore, the temperature dependence of the superfluid density in mixtures and pure ^{4}He films are different indicating the transition is also different from that of a ^{4}He film. At intermediate concentrations, the signature of phase separation disappears at the same concentration where a kink in the superfluid transition line occurs. Furthermore at this same concentration a kink in the tortuosity is also found;

below this concentration the tortuosity parallels ^{4}He film behavior, but above it the tortuosity increases much faster with ^{3}He concentration. This is interpreted as due to a change in the morphology of the superfluid and lends strong support to the idea that the two transition lines join. These results are discussed in terms of a recent "capillary condensation" model.

ACKNOWLEDGEMENTS

First and foremost I would like to thank my supervisor, John Beamish, for his support throughout my tenure here; without his patience and perseverance this thesis would not have been possible, also for his depth and breadth of knowledge, which never ceased to amaze me. An extended thanks to Moses Chan and Norbert Mulders for interest in my work and for the aerogel they most graciously supplied. Also, my thanks to L. Hrubresh for suppling the higher density aerogel.

I also thank Don Mullin for showing me the finer points of soldering, vacuum systems and contributing (often) to the "better graduate student handbook"; also Ken Marsh for his helpful ideas and general knowledge. Yolande Peske and Steve Rogers supplied me with (my favorite element) helium throughout my stay, sometimes on unreasonably short notice. I would also like to thank those people that are indispensable to the daily operations of the department, specifically Lynn Chandler who made my stay here that much more enjoyable, but also Rose and Phyllis.

On a more personal side, I would like to thank Nicola for all her love and support and to Owen for making my days much brighter. I would also thank Loran and Erena, who pointed out the benefits of Edmonton and for 4 years of good friendship.

Financial support for this work is acknowledged from the Natural Science and Engineering Research Council of Canada, as well as support from the University of Alberta.

TABLE OF CONTENTS

Chapter

1 Introduction 1

2 Phase Separation, Superfluidity and Ultrasonic Measurements in Porous Materials 8

- **2.1. Superfluid Helium** 8
  - 2.1.1. The two fluid model 9
  - 2.1.2. Criticality and Superfluid Helium 11
  - 2.1.3. Ultrasonic attenuation in helium 13
  - 2.1.4. Mixtures of ^{3}He and ^{4}He 14
- **2.2. Phase Separation in Helium Mixtures** 17
- **2.3. Aerogel** 22
  - 2.3.1. Structure of Aerogel 23
  - 2.3.2. Surface Area and Capillary Condensation 25
- **2.4. Helium in Porous Media** 29
- **2.5. Propagation if Ultrasound in Porous Media** 34
  - 2.5.1. Ultrasonic Modes 34
  - 2.5.2. Low and High Frequency Regimes 37
  - 2.5.3. Propagation in Helium Filled Pores 38
  - 2.5.4. Tortuosity 39
  - 2.5.5. Longitudinal Modes 40
  - 2.5.6 Ultrasonic Attenuation 43

3 Experimental Methods 45

- **3.1. Ultrasonic System** 45
- **3.2. Thermometry and Temperature Control** 49
- **3.3. Sample Preparation** 49
- **3.4. Mass Spectrometer and Gas Handling System** 53
- **3.5 Dilution Refrigerator** 55
- **3.6 Computer Control** 57

4 Helium Films in Aerogel 58

- **4.1. Previous Measurements** 59
- **4.2. General Trends in Ultrasonic Velocity and Attenuation** 59
- **4.3 ^{4}He Inert Layer** 64
- **4.4 Tortuosity Measurements** 66
- **4.5 Tortuosity of Films** 73
- **4.6 Conclusions** 85

5 Helium Mixtures in Aerogel 86

- **5.1. The Superfluid Transition in Aerogel** 87
- **5.2. Mixtures in Aerogel** 89
- **5.3. Helium Mixture Phase Diagram in 87% Aerogel** 107
- **5.4. Modeling the Density Effects in Helium Mixtures** 111
- **5.5. Comparison with Film Data** 127
- **5.6. Tortuosity of Helium Mixtures** 132
  - 5.6.1 Tortuosity Measurements 134
  - 5.6.2 Tortuosity near T_λ 136
  - 5.6.3 Discussion 141
  - 5.6.4 Conclusion 148
- **5.7. Discussion** 148
  - 5.7.1. Torsional Oscillator and Heat Capacity Measurements 149
  - 5.7.2. Capillary Condensation and Higher Porosity Aerogel 153
  - 5.7.3. Summary 156

6 Summary 159

References 163

LIST OF TABLES

5.6.3.1 Comparison of Equivalent Porosity and Tortuosity 147

LIST OF FIGURES

1.1 Phase diagram of Helium Mixtures in 98% aerogel 5
2.1.2.1 Two Fluid Model 11
2.2.1 Theoretical Coexistence Curve for Binary Solution 18
2.2.2 Bulk Phase Diagram of Helium Mixtures 20
2.3.1.1 TEM Micrograph of 87% Aerogel 24
2.3.2.1 ^{4}He Liquid-Vapor Isotherm in 87% aerogel 27
2.4.2 Heat Capacity Data, Mixtures in 98% aerogel ($0.4<X^*<0.55$) 33
2.5.1.1 Sound Coupling 36
2.5.4.1 Decoupling of Shear and Longitudinal Modes 42
3.1.1 Schematic of Ultrasonic System 48
3.3.1 Schematic of Epoxied Aerogel and Cu Cell 51
3.3.2 Liquid Nitrogen BET Isotherm Plot 52
3.4.1 Gas Handling System 54
3.5.1 Schematic of Dilution Refrigerator 56
4.2.1 General Trends in Velocity for ^{4}He Films 60
4.2.2 General Trends in Attenuation for ^{4}He Films 62
4.2.3 Velocity and Attenuation for 500 μmol Film 63
4.3.1 T_λ vs. ^{4}He Adsorption 65
4.4.1 Definitions of Velocity Measurements 68
4.4.2. Example of Background Subtraction Procedure 70
4.4.3 Velocity Data for Series of Helium Films 72
4.5.1 6.5 MHz Velocity Data 74
4.5.2 11 MHz Velocity Data 75
4.5.3 Limiting Tortuosity of Thin Films 77
4.5.4 Change in Tortuosity: Thin-Thick Films 78
4.5.5a&b Determination of the Inert Layer 80
4.5.6 Tortuosity of Helium Films 84

5.1.1 Full Pore Aerogel 88
5.1.2 Log-log Plot of the velocity versus reduced temperature 90
5.2.1 Mixture Velocity and Attenuation, X~0.08 91
5.2.2 11 MHz Velocity Data for X=0.12 to 0.69 92
5.2.3 11 MHz Velocity Data for X=0.06 to 0.27 94
5.2.4 11 MHz Velocity Data for X=0.27 to 0.39 96
5.2.5 11 MHz Velocity Data for X=0.4 to 0.5 97
5.2.6 Velocity and Attenuation for X=0.69 98
5.2.7 General Trends in Attenuation 100
5.2.8 Hysteresis in Velocity and Attenuation 102
5.3.1 Phase Diagram: Helium Mixture in 87% Aerogel 103
5.3.2 Phase Diagram: Corrected 105
5.3.3 Tricritcal Region of Lambda Line 107
5.3.4 Raw Attenuation Data 109
5.3.5 Background Subtracted Attenuation 110
5.4.1 Velocity "Jumps" at T_s for 6.5, 11, 12.5 MHz 112
5.4.2 Temperature Dependence of c_2 113
5.4.3 Measurements of ΔT and Velocity Jump 116
5.4.4 Comparison of Temperature Spans 117
5.4.5 Determination of the Effective Mass 119
5.4.6 Model and Experimental Velocity Data 122
5.4.7 11 MHz Velocity Data 123
5.4.8 PSU Torsional Oscillator Data (ΔP) for 98% aerogel 124
5.4.9 Model and Mixture Velocity Data - Scaled 126
5.5.1 Film and Mixture Velocity Data 129
5.5.2 Scaled Comparison of Film and Mixture Velocity 131
5.5.3 Film and Mixture Transition Temperatures vs. X* 133
5.6.1.1 6.5 MHz Velocity Evolution with X* 135
5.6.1.2 Tortuosity of Mixtures and Films 137
5.6.2.1 11 MHz Mixture Velocity vs. Reduced Temperature 139

5.6.2.2 Superfluid Density Exponent and Critical Amplitude 140
5.6.3.1 Residual ^{3}He in Low X^* Mixtures 144
5.6.3.2 Inert Layer Correction 146
5.7.1.1 Torsional Oscillator T-X^* Diagram 150
5.7.1.2 Heat Capacity Data, Mixtures in 87% aerogel $0.4 \le X^* \le 0.55$ 151
5.7.1.3 Heat Capacity Data, Mixtures in 87% aerogel $(0.59 \le X^* \le 1)$ 152

Chapter 1

Introduction

Helium continues to be *the* paradigm for investigations of phase transitions. Since its first liquefaction, where it was used in the discovery of the superconducting transition in mercury [1], helium has played an important role in the study of phase transitions. The primary incentive for this inexhaustible interest is the importance of quantum effects on the properties of helium. Due to its diminutive mass, helium has a large zero point energy. Helium also has a weak inter-particle interaction due to its filled electronic shell. These two properties of the helium atom lead to intriguing behavior in collections of atoms. The most common isotope is ^{4}He, an end product of hydrogen fusion which powers suns; the other isotope, ^{3}He, is only a millionth as naturally abundant and is a result of tritium decay [2]. This thesis is concerned with mixtures of these two isotopes and with two significant differences between them. The first is that, due to its smaller mass, the zero point energy of ^{3}He is larger than that of ^{4}He. The zero point energy can be estimated using the Heisenberg uncertainty principle, $E_o \sim h^2/2mV_a^{2/3}$, where m is the mass of the isotope in question and V_a is the atomic volume. The larger zero point motion is reflected in ^{3}He's larger molar volume. The second difference is in the statistics obeyed by the isotopes, which become important at low temperatures. ^{3}He has a single neutron resulting in a spin of ½ and is consequently a fermion, obeying Fermi-Dirac statistics. ^{4}He on the other hand has spin zero and obeys Bose-Einstein statistics. As a result of these differences liquid ^{3}He and ^{4}He behave very differently. ^{4}He is a bose liquid, and becomes superfluid below the lambda transition at T_λ=2.17 K. This is related to Bose-Einstein condensation (BEC) [3], as predicted by Bose and Einstein in 1924 [4,5], which can only occur in a collection of bosons. ^{3}He, on the other hand , is a Fermi liquid and so has no such transition; above about 2 mK it is an ordinary (quantum) fluid.

The lambda transition has several salient features [2]. It is a continuous, or second order, transition with no latent heat. The specific heat diverges approximately logarithmically at T_λ; the name 'lambda transition' is derived from the shape of this curve. Visually what is seen as the temperature is cooled through the lambda point is a sudden cessation of boiling; the thermal conductivity of the superfluid is so high that vapor bubbles cannot nucleate in the liquid. Below the lambda point, the liquid, He II, is a superfluid with vanishing viscosity.

The concept of universality has been very successful classifying the critical behavior of pure systems in terms of their dimensionality and the number of components of their order parameter. The limiting behavior of systems close (in temperature) to continuous phase transitions can be described in terms of a few critical exponents. For the lambda transition in ^{4}He , the measured and calculated exponents for the heat capacity (α=−0.013) and for the superfluid density (order parameter) (ζ=0.67) agree very well with universality predictions (in phase transition theory this exponent is typically β). This detailed understanding of the lambda transition in pure ^{4}He provides the basis for investigations of the effects of impurities, confinement and disorder. One approach to investigating these effects is to confine the helium in channels of pores with very small dimensions and study the effects on the lambda transition. Two primary results came from these studies. The first was a suppression of the lambda transition temperature (T_λ); the second was that measurements of parameters that changed very sharply in bulk systems (e.g., heat capacity peak) became rounded or completely disappeared when the helium was confined. Both the amount by which T_λ was suppressed and the rounding depended on the nature of the pores. Early studies were plagued with uncertainties in the structure of the material [6] since many porous materials have a distribution of pore sizes. Advances in lithography techniques have made possible a systematic approach to the problem of confinement of superfluid helium [7].

The effects of confinement in porous media on other transitions are also of immense interest. For example, the freezing and melting of liquids in porous materials such as Vycor (a porous glass characterized by interconnected worm-like pores with radius r_p~15 nm) have been studied for many years and are still of interest [8-12]. Adsorption of gas onto the surface of porous materials and the liquid-vapor critical point have been studied in porous materials. The effect of porous media on binary solutions is closely related to this. de Gennes pointed out that phase separation in porous materials may be an experimental realization of a random field phase transition [13]. He predicted the major effects would be the preferential adsorption of one of the species and the reduction of the inter-species coupling in the vicinity of the pore walls. Liquid-vapor systems and binary solutions are of considerable interest since they are in the same universality class and so may display similar behavior under random field conditions. Measurements have generally found a much narrower coexistence region when mixtures are contained within porous media, and the critical behavior is altered from that of bulk systems [14-16].

Recent work on liquid helium has turned to porous media as a way to study the effects of impurities (due to its low boiling point, liquid helium is inherently pure, so introduction of impurities is not trivial) and those of pore structure on the lambda transition [17, 18]. Within the last 10 years, attention has been focused on a material called aerogel. Aerogel is an ideal material with which to investigate the effects of impurities due to its unique structure and very low density. Silica aerogel can be made with densities from 0.33 g/cc to 0.004 g/cc. The latter is only 4 times the density of air with only 0.2% of the volume occupied by silica, so is extremely porous. Such dilute amounts of silica suggest the system might be described as a quenched impurity (the silica provides spatially fixed, or quenched, impurities) [18] in liquid helium, rather than as helium confined in pores. Aerogel has a structure of interconnected strands that form self similar structures over length scales 10-150 nm [17].

Measurements of the critical behavior (behavior near the lambda transition) of ^{4}He in aerogel produced intriguing results. The heat capacity of ^{4}He in aerogel displays a cusp-like singularity, as opposed to the logarithmic singularity of bulk helium [17]. Simultaneous measurements of heat capacity and superfluid fraction showed that the superfluid density vanished at the same temperature as the cusp in heat capacity. Further, the lambda transition moved to lower temperatures for higher density aerogels and the critical exponents of the helium-aerogel system were different from those of bulk, suggesting the possibility of a new universality class [18]. Thus began the aerogel revolution.

This activity led to a recent study of ^{3}He-^{4}He mixtures in a 98% porous aerogel at the Pennsylvania State University (Penn State). Figure 1.1 shows the resulting temperature versus concentration ($X \equiv X3 = n_3/(n_3+n_4)$ is the molar ^{3}He concentration) phase diagram and that for bulk mixtures (solid lines). Bulk helium mixtures display two transitions, the lambda transition and phase separation. As ^{3}He is added to pure ^{4}He the lambda transition is suppressed and the lambda point becomes a "lambda line" in the T-X plane. At a temperature of T_{tr}=0.872 K and concentration X_{tr}=0.67, the lambda line terminates in a tricritical point at the top of the phase separation curve [19]. Below 0.872 K, mixtures phase separate into coexisting ^{4}He-rich and ^{3}He-rich phases. The ^{4}He-rich phase (the left side of the coexistence curve) is superfluid but the ^{3}He-rich phase is not. Mixtures with $X<0.064$ do not phase separate, even at $T=0$. If $X>0.064$, the two coexisting regions at $T=0$ are a normal phase of pure ^{3}He and a superfluid phase containing 6.4% ^{3}He [20, 21]. When the mixture is diluted with 2% aerogel impurity,

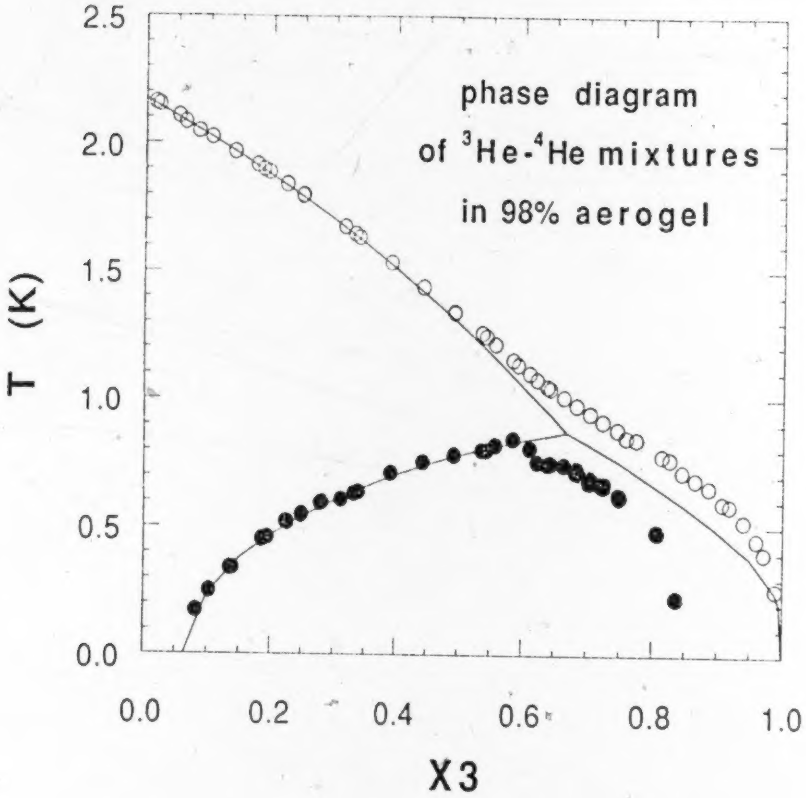

Figure 1.1. Phase diagram of helium mixtures in 98% aerogel as determined by torsional oscillator measurements. The open symbols are the superfluid transition, the filled symbols are the phase separation line. Data courtesy of M. Chan.

however, the phase diagram changes significantly (Fig. 1.1). S.B. Kim and J. Ma, working with M. Chan, used a torsional oscillator to probe the aerogel mixture system [16]. The basic principle behind the torsional oscillator method is to measure the superfluid density. The symbols in Figure 1.1 are transitions at temperatures determined from the torsional oscillator data. There are two departures from bulk mixture behavior: the phase separation line (filled symbols) is detached from the lambda line (open symbols) so the tricritical point is replaced by an ordinary critical point at the top of the phase separation curve. The lambda transition extends beyond the bulk tricritical point, apparently to zero temperature at high ^{3}He concentrations. Fig. 1.1 shows that the topology of the phase diagram is altered by the addition of 2% impurity.

The detachment of the phase separation line has fascinating implications. At high ^{3}He concentrations there is the possibility of a very dilute Bose gas superfluid. At very low temperature (~1 mK) the ^{3}He should also become superfluid and two interpenetrating superfluids may coexist.

A flurry of theoretical investigations followed [22-25]. These modeled the effects of confinement and of random quenched impurities introduced by the aerogel [23, 25]. Experiments continued, including measurements on different densities of aerogel, intending to answer several questions. If this dramatic result occurred in 98% porosity systems, what would happen for lower porosities where the density of impurities was much higher? What was the mechanism, or microscopic distribution of the isotopes in aerogels that allowed superfluidity at high ^{3}He concentrations?

At this time preliminary ultrasonic measurements on a few mixtures contained in 87% porous aerogel [26] showed promise in studying helium mixtures in aerogels. As will be discussed in detail in Chapter 2, ultrasonic velocities generally depend on both the modulus and the density of the system. However, a shear mode propagating through a porous material filled with a liquid is sensitive only to changes in effective density since the liquid does not contribute to the shear modulus. In this respect, ultrasonic velocity measurements are analogous to torsional oscillator measurements. However, ultrasonic techniques have the advantages of high (and variable) frequency and so are sensitive to dissipation; the velocity is sensitive to overall density; and longitudinal and shear modes can be used to probe modulus effects in fluids. Due to the sensitivity of the ultrasonic velocity to isotopic concentration, it has also been used to probe phase separation in bulk helium mixtures [2]. The attenuation of ultrasound provides additional information. A critical attenuation peak accompanies the lambda transition [27, 28] in bulk mixtures. The damping of torsional oscillators also provides information, but low frequencies are used and interference from superfluid acoustic modes complicates measurements of dissipation. On the negative side, high frequency effects may cause rounding of the superfluid transition in ultrasonic measurements.

The initial aim of this work was to investigate helium mixtures for a number of aerogel porosities. However, propagation of ultrasound through higher porosity aerogel proved difficult. The research focused on the 87% porosity aerogel with the interesting conclusion that the effects of 98% aerogel were not amplified in lower porosity aerogels, but instead seemed to disappear producing a more bulk-like phase diagram. The phrase "less is more" was used to describe this trend [29].

The thesis is organized as follows. Chapter 2 presents background material covering phase separation, an introduction to superfluidity, a description of previous measurements on 98% aerogel and an overview of the theory of ultrasonic propa-gation in saturated porous media. Chapter 3 is a description of the experimental techniques employed. Chapters 4 and 5 report and discuss the experimental results on pure ^{4}He films and on helium mixtures, respectively. The essential results are summarized in Chapter 6.

Chapter 2

Phase Separation, Superfluidity and Ultrasonic Measurements in Porous Materials

Introduction of a solid matrix (porous material) to a pure system adds to its complexity. While this seems counter to the physics adage "assume a spherical cow," complexity is a logical progression; however, the pure system needs to be fully understood before the effects of impurities are pursued. Since helium is perhaps the most thoroughly studied pure system, it is an obvious choice to investigate the effects of disorder and impurities. This chapter reviews the properties of bulk helium, both pure ^{4}He and ^{3}He-^{4}He mixtures, including an introduction to the critical phenomena associated with the lambda transition, as well as the behavior of helium imbibed by porous aerogel. The relevant properties of the porous medium used in this work, aerogel, are also presented. Finally a discussion of ultrasonic propagation through fluid filled isotropic porous media is presented.

2.1. Superfluid Helium

Phenomenological descriptions of superfluid ^{4}He are well tested [2] and provide an excellent framework to describe the measurements in this thesis.

2.1.1 The two-fluid model

Early experiments revealed an apparent paradox in the behavior of ^{4}He; the viscosities measured in different types of experiments did not agree. In experiments designed to measure viscous flow resistance, a narrow channel is packed with a porous material and the viscosity is proportional to the pressure required to force the fluid through at some velocity. These experiments found that below a certain temperature, T_λ (the lambda point), the flow velocity was almost independent of the pressure gradient along the channel; such a result suggested superfluid helium has vanishing viscosity.

In a second type of experiment, designed to measure the viscous drag on a moving body, torsional oscillators were used to measure the inertial coupling of the liquid to the oscillator. The method was based on the dependence of the oscillator period (P) on the torsion constant (k) and the moment of inertia (I_b) via

$$P = 2\pi\sqrt{I_b/k} \qquad (2.1.1.1)$$

Since liquid within a "viscous penetration depth," δ, is dragged along with an oscillating surface, the moment of inertia and hence the period of the torsional oscillator was very sensitive to amount of mass viscously coupled to the torsion bob. In experiments with helium, cooling below T_λ caused the period of oscillation to decrease sharply but continuously, indicating that some fluid remained viscously coupled below T_λ. A fluid with zero viscosity should contribute *no* loading to the oscillator, however, the viscosity of the fluid as determined from the oscillator damping was similar to that of helium gas. Apparently superfluid ^{4}He is both viscous and non-viscous, hence the paradox.

The viscosity contradiction was resolved by the introduction of a two-fluid model for superfluid helium by Tisza [30] which describes helium below the superfluid transition (known as He II) in terms of a mixture of two liquids, a normal fluid component possessing a viscosity, and a superfluid component capable of frictionless flow. The normal and the superfluid components cannot be physically separated; in fact since the helium atoms are indistinguishable, one cannot even consider some atoms as belonging to the normal fluid and the rest to the superfluid. Despite their indistinguishability, each fluid is associated with an effective mass density so the total density of the helium is

$$\rho_4 = \rho_n + \rho_s \tag{2.1.1.2}$$

where the subscripts refer to the normal and superfluid components.

Given the two-fluid model, the torsional oscillator results are easily interpreted. Below T_λ, the zero viscosity superfluid fraction, $\rho_s(T)/\rho$, of the fluid was no longer entrained by the oscillating discs. The change in period represents the temperature dependence of the remaining normal fraction, $\rho_n(T)/\rho$, of the helium. Given the total density of ^{4}He, the superfluid fraction can be determined. Figure 2.1.1.1 shows the variation of the superfluid and normal fractions with temperature; below about 1 K the fluid is almost entirely superfluid. Because they depend only on the coupled mass, torsional oscillator measurements are the quintessential measurement technique of the superfluid fraction, as was first demonstrated by Andronikashvili [31].

The two-fluid model has been used to describe other properties of superfluid helium. A flow velocity can also be assigned to each of the fluids. The apparent zero viscosity measured in flow resistance experiments can now be understood since only the superfluid fraction flows through very small pores. The normal fluid carries all the heat and entropy; the superfluid fraction flows toward regions of higher temperatures in order to reduce the temperature gradient. Since the superfluid flows without resistance the thermal conductivity is large.

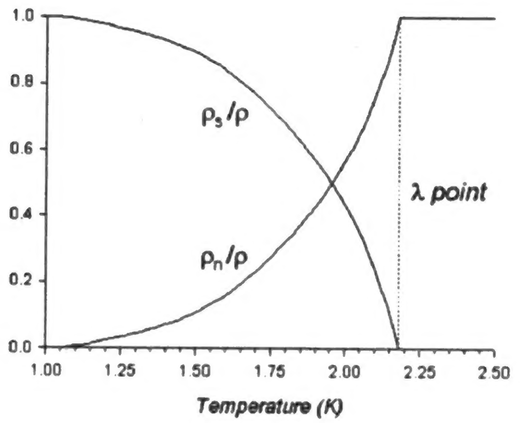

Figure 2.1.1.1. Superfluid and normal fractions in bulk He II below T_λ.

2.1.2 Criticality and Superfluid Helium

Because the lambda point corresponds to a continuous phase transition, investigation of critical behavior has been one of the driving forces behind interest in liquid helium research. Since the experimental work in this thesis involves both the superfluid and phase separation transitions, basic ideas of critical behavior are presented.

The simplest example of a critical point is found in liquid-vapor coexistence systems; when the pressure and temperature of a closed system containing a liquid and vapor in coexistence are increased, coexistence ceases at the critical point (P_c, T_c). As the critical point is approached, the densities and the entropies of the liquid and vapor phases converge. The transition at the critical point is classified as continuous or second order and is accompanied by a critical peak in the heat capacity. An underlying concept in critical behavior is that of the *order parameter*, which describes the ordering (as opposed to disorder) of a system and whose value defines the state of the system. For example, the order parameter in a liquid-vapor system is the density difference between the two phases. Typically, the order parameter is zero above the transition where the system is disordered; in the liquid-vapor system, there is no density difference above T_c, but ordering occurs below T_c as the liquid and vapor phases separate.

As superfluid ^{4}He is considered to be a macroscopic occupation of the quantum mechanical ground state [3], the order parameter is a two-component complex function,

$$\psi = |\psi(r)| e^{i\theta} \tag{2.1.2.1}$$

representing the wave function of the ground state. The two degrees of freedom are the magnitude $|\psi|$ and the phase θ. Through the appropriate normalization of the wave function, the superfluid density is related to the order parameter by

$$\rho_s = m_4 |\psi(r)|^2 \tag{2.1.2.2}$$

where m_4 is the atomic mass of ^{4}He and ρ_s increases continuously from zero at the transition to ρ_4 at T=0 K.

A property common to critical behavior is the power law dependence of quantities like the order parameter and the coherence length. For example, the superfluid density near T_λ, can be written in terms of the reduced temperature, $t=1-T/T_\lambda$, raised to some power, ζ,

$$\rho_s \approx \rho_{so}(t)^\zeta \tag{2.1.2.3}$$

where for bulk measurements at saturated vapor pressur $\zeta=0.6717(4)$ and $\rho_{so} = 0.351$ g/cc, and the power law behavior has been shown to hold true over several orders of magnitude in reduced temperature. This power law characterization is at the heart of the concept of universality, where, with proper scaling, physically different systems undergoing transitions will display similar power law behavior. Further, only two parameters are required to classify a transition: the dimensionality and the number of degrees of freedom in the order parameter. For bulk helium these numbers are 3 and 2, respectively.

The coherence length, ξ, is defined as the spatial extent of fluctuations in the order parameter. In the liquid-vapor system (and other binary systems), ξ is related to the thickness of the interface between the two phases; at T_c the coherence length and the interfacial width diverge. In superfluidity, the coherence length is related to the spatial changes in the phase of the wave function, and can be written in three dimensions as [18]

$$\xi(t) = \left(\frac{k_B T m_4^2}{\hbar^2}\right)\frac{1}{\rho_s(t)} \qquad (2.1.2.4)$$

where k_B is Boltzmann's constant, and $\hbar$ is Planck's constant.

2.1.3. Ultrasonic Attenuation in Helium

Of some interest in this thesis is the attenuation of sound near the lambda transition. Previous ultrasonic measurements on bulk helium have found a critical attenuation peak at the lambda transition [2]. Early measurements suggested some type of relaxation process [32] and a comprehensive theoretical description of critical attenuation was developed by Ferrell and Bhattacharjee [30] in the early 1980's. In their theory, the critical attenuation results from temperature undulations associated with the adiabatic compression and rarefaction induced by propagating sound waves. This idea is not new, but is an extension of an idea first put forward by Hertzfeld and Rice [33] to describe ultrasonic attenuation in systems with multiple energy modes. Hertzfeld and Rice argued that ultrasonic attenuation is due to relaxation processes whereby a finite time is required for energy modes to thermally equilibrate with the pressure wave. If the temperature varies on the time scale of the ultrasound period, the pressure and temperature oscillations will be out of phase resulting in energy dissipation.

In bulk helium the critical attenuation peak associated with the lambda transition is very sharp. At T_λ the attenuation remains finite and scales as $\omega^{1.1}$; at 12 MHz it is approximately 20 dB/cm with a full width at half maximum of $\sim 10^{-3}$ K [2, 28]. The addition of ^{3}He further complicates the sound attenuation process near T_λ. Roe et al. studied the sound attenuation in mixtures and found it became broader in temperature as T_λ was lowered by the addition of ^{3}He [28]. Further, for concentrations $X>0.55$ their attenuation data near T_λ was reasonably described by a diffusive relaxation mechanism, as opposed to fluctuations in the order parameter. The properties of helium mixtures are discussed in the next section.

2.1.4 Mixtures of ^{3}He and ^{4}He

Since mixtures are of interest here, one further consideration remains: what is the effect of ^{3}He on the superfluid properties? We first note that as ^{3}He are fermions they should not contribute to the superfluid component. For dilute mixtures of ^{3}He in ^{4}He, Heer and Daunt [34] considered the ^{3}He atoms to simply lower the number density of bosons present in the system. The Bose-Einstein transition temperature is dependent on the number density of bosons in the following way

$$T_\lambda(X=0) = \frac{h^2}{2\pi m_4 k_B}\left(\frac{n_4}{2.612 V_L}\right)^{2/3} \qquad (2.1.4.1)$$

where n_4 is the number of ^{4}He atoms and V_L is the volume of the liquid. The density of the mixture can be expressed as

$$\frac{n_4}{V_L} = \frac{n_4}{(n_3 v_3 + n_4 v_4)} \qquad (2.1.4.2)$$

where v_i is the molar volume of the i^{th} isotope. Equations (2.1.4.1) and (2.1.4.2) result in the following equation for the change in transition temperature with concentration of ^{3}He, $X=n_3/(n_3+n_4)$

$$\frac{T_\lambda(X)}{T_\lambda(0)} = \left(\frac{n_4}{n_3 v_3 + n_4 v_4}\right)^{2/3} = \left(\frac{1-X}{1+X\omega}\right)^{2/3} \approx (1-X)^{2/3} \qquad (2.1.4.3)$$

where $\omega=v_3/v_4-1$ (~0.34 for T<1 K) and X is the ^{3}He concentration. The exponent 2/3 is in good agreement with experiment in the limit $X\rightarrow 0$.

Equation (2.1.4.3) implies that the lambda temperature decreases with increasing X, thus resulting in a line of critical points in the T-X plane. Uehara [35] has measured the power law behavior of the superfluid density in helium mixtures using second sound techniques and found an exponent similar to the bulk exponent, with the concentration dependence of ρ_{s0} (see eqn. (2.1.2.3)) adequately described by

$$\rho_s(X,t) \approx \left(\frac{1-X}{1+X\omega}\right)^2 \rho_s(0,t) \qquad (2.1.4.4)$$

The addition of ^{3}He does not qualitatively change the nature of the critical behavior at the lambda point.

As the ^{3}He atoms do not contribute to the superfluid component, they must contribute only to ρ_n. This has been confirmed by flow experiments where the ^{3}He atoms did not take part in the superfluid flow [2]. Feynman [36] treated the ^{3}He atom as a solid sphere moving through an ideal fluid and used classical hydrodynamics to show the effective mass m_3^* is the sum of the bare mass of ^{3}He and one half the mass of the displaced fluid. For ^{3}He atoms in a ^{4}He superfluid

$$m_3^* = m_3 + \frac{1}{2}\left(\frac{v_3}{v_4}\right)m_4 \qquad (2.1.4.5)$$

where v_3, v_4 are the atomic volumes. Classically, the extra inertial term is due to the back flow generated by a solid sphere as it moves through the fluid. Dividing through by the ^{3}He molar volume gives

$$\rho_3^* = \rho_3 + \frac{1}{2}\rho_4 \qquad (2.1.4.6)$$

Dash and Taylor further suggest that, since the effective mass is due only to the relative motion of ^{3}He through the superfluid, the density of ^{4}He should be replaced by the superfluid density

$$\rho_3^* = \rho_3 + \frac{1}{2}\rho_s(T) \qquad (2.1.4.7)$$

m_3* is now a function of temperature varying from m_3 at $T=T_\lambda$ to the value of eqn. (2.1.4.5) at T=0. One further modification was required. Dash et al. found that eqn. (2.1.4.7) represented the data well if the back flow contribution was somewhat higher; the ½ being replaced by 0.796 [68].

Dilute amounts of ^{3}He ($X<0.064$) are soluble in ^{4}He down to 0 K. However, concentrations greater than this result in a solubility gap: the mixture phase separates into ^{4}He rich and ^{3}He rich components. Phase separation of helium mixtures is discussed in the following section.

2.2. Phase Separation in Helium Mixtures

For a simple thermodynamic treatment of phase separation we consider a regular binary solution of 'a' and 'b' particles in which the change in entropy on mixing can be written [37]

$$\Delta S = -N_A k_B (X\ln X + (1-X)\ln(1-X)) \qquad (2.2.1)$$

where X and (1-X) are both less than one so, as expected, the entropy increases as the system moves from an ordered state (completely separated) to a disordered state (completely mixed). The change in energy associated with mixing can be estimated by considering z nearest neighbor interactions on a lattice with interaction energies V_{ab}, V_{aa}, and V_{bb} between particles, and is given by

$$\Delta U = \tfrac{1}{2} z N_A X(1-X)(2V_{ab} - V_{aa} - V_{bb}) = X(1-X)w \qquad (2.2.2)$$

where N_A is Avogadro's number and the excess energy w is a measure of the non-idealness of the solution; for an ideal mixture $w \equiv 0$. Assuming changes in volume are small on separation, the free energy can be constructed using (2.2.1) and (2.2.2)

$$\Delta G = G_m - G_s = X(1-X)w + N_A k_B T(X\ln X + (1-X)\ln(1-X)) \qquad (2.2.3)$$

The maximization of entropy always favors the mixed state as the temperature is increased, whereas the energy of mixing (ΔU) may be positive or negative. If $\Delta U > 0$ then phase separation is energetically unfavorable at low temperatures ($\Delta G > 0$); for phase separation to be favorable $\Delta G < 0$. Phase separation is driven by a classic competition between energy and entropy. Using the expressions for ΔU and ΔS we can determine the phase separation temperature where $\Delta G = 0$,

$$T_s = X(1-X)w/(R\ln 2) \tag{2.2.4}$$

Equation (2.2.4) describes the (ideal) phase diagram of a regular binary mixture in the X-T plane (Fig. 2.2.1). The dashed line defines the coexistence region. In a mixture of concentration X, when the temperature is below $T_s(X)$ a solubility gap is found and the concentrations of the two phases are fixed by the temperature; there are no stable states inside the coexistence region. The dark solid line indicates the path the system follows as the temperature of a mixture is lowered. When $T=T_s(X)$ the mixture phase separates into concentrations x_1, x_2. Further cooling causes changes in the concentrations of the two phases: $x_1 \rightarrow x_1'$ and $x_2 \rightarrow x_2'$. Also, as the temperature is reduced below T_s, the volume fraction of each phase changes according to the lever rule. Given the concentrations (x_1,

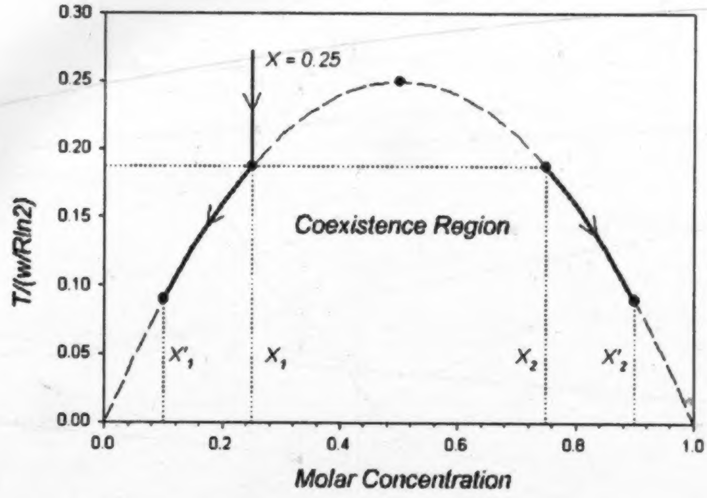

Figure 2.2.1. A theoretical temperature-concentration coexistence curve for an regular binary solution that phase separates. The dashed line is the coexistence curve and the dark solid lines show the path a system of concentration $X=x_1$ follows as the temperature is lowered below T_s. The critical point is shown as the filled symbol.

x_2) of two phases in equilibrium and an overall concentration of X, the relative fractions of the two phases c_1 and c_2 are

$$c_1 = (x_2-X)/(x_2-x_1); \quad c_2 = (X-x_1)/(x_2-x_1) \qquad (2.2.5)$$

Since $c_1+c_2=1$, as the temperature is cooled one phase grows at the expense of the other. In this respect, binary fluid phase separation is analogous to the liquid vapor transition where the fluid (vapor) condenses (evaporates) out of the vapor (fluid) as the temperature is decreased (increased). Due to symmetry, eqn. (2.2.4) predicts a simple relationship between the phases: $x_2=1-x_1$ for this model. At T=0 K, the phase diagram of Fig. 2.2.1 indicates the phases have separated into the pure components.

Figure 2.2.1 also displays a critical point at the apex of the parabola. As in a liquid vapor system, the distinction between the two phases disappears at the critical point; the densities of the two phases become equal, the interfacial tension goes to zero while the interfacial width diverges. In the derivation of eqn. (2.2.4) equal atomic volumes were assumed for the two components, so the critical concentration is $X_c=½$. The critical temperature T_c, follows from $T_c = T_s(X_c) = w/(4R\ln 2)$.

In comparison to the model discussed above, the phase diagram of helium mixtures is more complicated, and is shown Fig. 2.2.2. In helium mixtures X is defined as the ^{3}He concentration, $n_3/(n_3+n_4)$, where n_i is the number of moles of the i^th^ isotope. The solid line in the T-X diagram represents the lambda transition. Note at temperatures below the solid line the mixture is a superfluid, whereas at concentrations to the right of the solid line the mixture is a normal fluid.

The grey area defines the coexistence region and has several prominent features in comparison with the region in Fig. 2.2.1. First, mixtures with $X< 0.064$ are miscible at all temperatures and do not phase separate, even at T=0 K. This is a result of a disparity

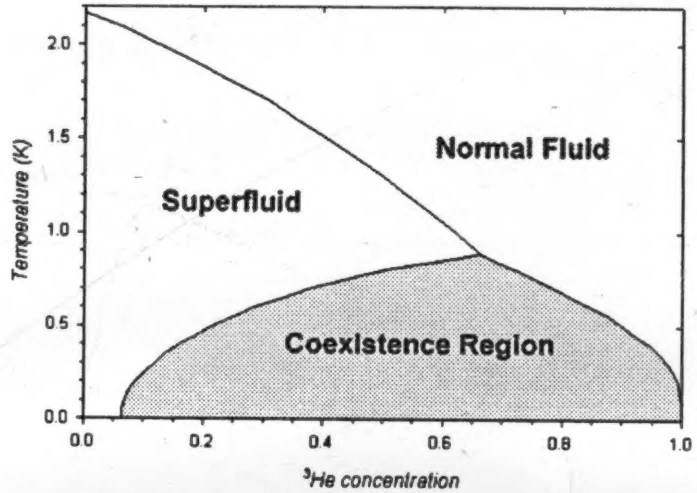

Figure 2.2.2. Phase diagram of bulk ^{3}He-^{4}He mixtures. The solid line is the superfluid transition. The grey area is the coexistence region: mixtures in this region phase separate into concentrations defined by the borders.

between the ^{3}He latent heat and the binding energy of ^{3}He in ^{4}He [38] at T=0 K. At T=0 there is no contribution from the entropy, and ΔU for mixtures with $X<0.064$ must be negative, resulting in a stable mixed phase. In helium mixtures the coexistence is also between phases of very different properties. Equilibrium is between a normal ^{3}He rich and a superfluid ^{4}He rich phase as well as between phases with different concentrations. In bulk helium mixtures the ^{3}He rich phase is less dense and floats atop the superfluid ^{4}He rich phase.

In addition to the miscibility at T=0 K of dilute solutions, the critical concentration is shifted to a higher value, $X_c = 0.67$. The approach to the apex of the phase separation curve from either side is linear resulting in a cusp at X_c [19]. Furthermore, the lambda line intersects the phase separation curve at a tricritical point, named for the intersection (in a suitable phase space) of three lines of critical points [39, 40]. Graf et al. determined the location of the tricritical point to be (X_{tr}, T_{tr})= (0.67, 0.87 K) and found the coexistence line on both sides to linearly approach the tricritical point [19].

Blume, Emery and Griffiths (BEG) applied an Ising model to bulk helium mixtures [41]. BEG considered a spin 1 Ising model where ^{3}He atoms are represented by $S_i=0$, and ^{4}He atoms as $S_i = \pm1$ with the sign indicating the superfluid ordering for liquid ^{4}He. The BEG Hamiltonian consists of three terms

$$H_m = -J\sum_{<i,j>} S_i^z S_j^z + -K\sum_{<i,j>} S_i^{z2} S_j^{z2} + \Delta\sum_{<i>} S_i^{z2} \qquad (2.2.6)$$

The first term models the superfluid ordering as it leads to a second order transition with a nonzero value of the "magnetization" M ($=N^{-1}\sum S^z_i$) below a temperature that depends on J and the ^{3}He concentration. The second term introduces interactions between the different types of atoms and is reminiscent of arguments presented in regular solution theory, $V= V_{33}+V_{44}-2V_{34}$. The final term, $\Delta= \mu_3 - \mu_4 +2z(V_{33}-V_{44})$, with μ representing the chemical potential of a given isotope and z the number of nearest neighbors, arises from the introduction of the chemical potentials to insure the conservation of particles.

With the proper parameters (V<<J), this model reproduces the helium mixture phase diagram uncannily. In fact, when V=0 the BEG model predicts a tricritical point at a temperatue $T_{tr}=⅓T_\lambda(0)$ and a concentration X_{tr} = ⅔, close to the observed values of $T_{tr}=0.4T_\lambda(0)$ and X_{tr} = 0.67. The BEG model does not, however, reproduce the finite solubility of ^{3}He in ^{4}He at T=0 K; this would require inclusion of Fermi statistics to model the ^{3}He-^{4}He interactions.

It is noteworthy that the model reproduces experimental measurements when V=0. In the regular solution model setting V=0 is equivalent to treating helium mixtures as ideal solutions which should not phase separate. This introduces some doubt as to what drives phase separation in helium mixtures; BEG attribute phase separation for V=0 to the superfluid ordering in the system. Consider only the J term in the Hamiltonian above. Adding ^{3}He means some of the S_i are zero, so when X is sufficiently large the Hamiltonian is minimized by phase separation of the superfluid and the ^{3}He atoms; maximizing ^{4}He-^{4}He (superfluid) pairs (maximizing ^{3}He-^{3}He pairs minimizes zero terms) maximizes negative terms and minimizes H. That is, the BEG model suggests superfluid ordering drives the phase separation of the two isotopes.

Up to this point, the final term in the Hamiltonian has been neglected. The term proportional to Δ is a crystal field interaction which is independent of the superfluid ordering and so represents a bond type interaction. This bond-like interaction determines the nature of the phase separation transition. In particular, above a critical value of Δ phase separation at large X becomes a first order transition [41]. As we shall see, the bond-like interaction plays an important role in the modeling of helium mixtures contained in aerogel.

2.3. Aerogel

Aerogels are a singular class of materials produced by drying an alcogel. While aerogels can be made using many different precursors, notably alumina and silica, we are only concerned with silica aerogels (aerogel). Aerogel is not a new material; the sol-gel chemistry required to produce siloxane polymers was known as early as 1860 [42]. Hypercritical drying of a gel was first employed by Kistler [43] to demonstrate the existence of a solid gel matrix. Aerogel is remarkable by reason of its high porosity; samples can be made with porosities ϕ ranging from 85% to 99.8%. Only 0.2% of the volume of a sample of this latter porosity is occupied by silica and its average density is only 4 times larger than the density of air.

Aerogel is formed from a sol-gel process which involves the poly-condensation of tetramethoxysilane (TMOS) resulting in a gel comprised of a solid silica network contained in a methanol solvent. The methanol is removed hypercritically to prevent destruction of the delicate silica network by capillarity forces arising from the liquid-vapor interface. The process of gel formation is thought to occur in three steps [42]. First, formation of particles by the polymerization of monomers occurs. The particles have a characteristic dimension of 1-2nm. Second, the continued growth of these particles results in reduced numbers locally with a characteristic cluster size of 5-10nm. Third, the particles link into chains which generate a network spanning the entire volume and form the gel. The gelation process is often described as "diffusion limited aggregation" and leads to an open structure of silica strands connected at random sites.

2.3.1. Structure of Aerogel

There are several methods available to probe the structure of aerogel. These include small angle scattering (X-ray, neutron, light) and transmission electron microscopy (TEM). The latter is the most striking as it produces visual images of the aerogel structure, although the interpretation of such pictures is perhaps more difficult and subjective. Scattering techniques generally provide information on correlations of the structure.

TEM microscopy probes the nanometer scale structure of silica aerogel. Figure 2.3.1.1 shows a TEM micrograph of an 87% aerogel specimen from the same batch as the aerogel used in the experiments. The photo suffers from drifting due to heating and/or charging of the aerogel in the electron beam. The magnification is 5×10^5 and the bar denotes 20 nm. There are clusters (dark) of approximately 10 nm in diameter forming the aerogel with no visible evidence of pores (light) larger than ~20 nm.

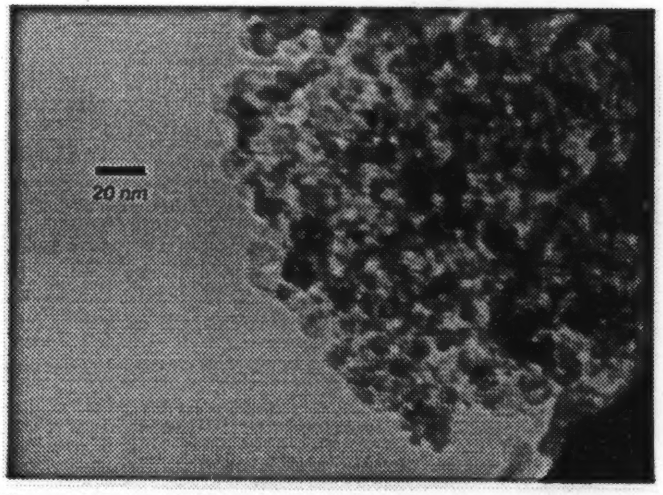

Figure 2.3.1.1. TEM micrograph of 87% aerogel sample cut from the same batch as that used in experiments. The magnification is 500k.

Small angle neutron and x-ray scattering have also been used to investigate the structure of aerogels. In these types of scattering experiments aerogel is exposed to a beam (x-rays, light, neutrons) of known wavelength and the scattered intensity is measured as a function of scattering angle. Introducing the wave vector q, the Bragg equation relates the scattering angle to a characteristic length scale, $d = 2\pi/q$.

$$q = (4\pi/\lambda)\sin(\tfrac{1}{2}\theta) \tag{2.3.1}$$

By using a combination of light, X-ray, and neutron scattering, length scales rom 0.1 nm to 1 μm can be probed. Data is plotted as the scattered intensity against the wave vector (q) on a log-log scale and shows a region of q where the intensity is proportional to q^{π}, i.e. roughly linear on a log-log scale. For example, $\pi \sim 2.3$ is typical of an 84% aerogel sample over a region $0.023 < q/\text{Å} < 0.135$ [44]; these values of the wave vector correspond to $46 < d < 250$ Å. Similar trends are obtained for higher porosity aerogel which indicates fractal-like correlations in the mass distribution. However, the scattering properties are dependent on the details of the preparation and to confuse the issue further, power law scattered intensity can also arise from a non-fractal system [42]. What is clear from the scattering data is that aerogel have no single characteristic length scale.

2.3.2. Surface Area and Capillary Condensation

Surface area is typically determined by adsorption isotherm measurements. Gas is admitted to the system at a fixed temperature and the amount adsorbed is determined as a function of the pressure. Employing a model like that of Brunauer-Emmett-Teller (BET) [45] allows an estimation of the surface area. The BET equation relates the reduced pressure, P/P_o (where $P_o(T)$ is the saturated vapor pressure of the gas, here N_2, at T) and the number of adsorbed moles, n.

$$\frac{P/P_o}{n(1-P/P_o)} = \frac{(c-1)}{n_m c}\frac{P}{P_o} + \frac{1}{n_m c} \qquad (2.3.2.1)$$

n_m is the number of moles required for an average coverage of one monolayer, and c is a constant which depends on the difference between the adsorbate-substrate and adsorbate-adsorbate interactions. Plotting the left hand side of eqn. (2.3.2.1) versus P/P_o gives a linear equation determining c and n_m. Once n_m is known, the surface area is

$$S = n_m N_A \sigma \qquad (2.3.2.2)$$

where N_A is Avogadro's number (1.6023×10^{23}) and σ is the areal coverage of a nitrogen molecule (16.2 Å^2). It should be noted that eqn. (2.3.2.2) is derived for a flat substrate and infinite half-space and in porous materials deviations from eqn. (2.3.2.2) are expected for $P/P_o \geq 0.5$ [34].

Certain simplifying assumptions are incorporated into the description of all porous materials. For the most part, the pore walls are considered to be relatively smooth on an atomic scale, and some basic geometry is chosen for the pores. A common description is that of intersecting cylindrical pores of some characteristic length and radius. Isotherms are used to measure the surface area, but can also provide information about the pore size distribution if both adsorption and desorption isotherms are measured. A complete ^{4}He isotherm on 87% aerogel is shown in Fig. 2.3.2.1. This T=2.42 K isotherm was measured by Jongsoo Yoon et al. at Penn State University. Adsorption is represented by the filled symbols, desorption by the open symbols; the inset is the entire range of pressures, $0<P/P_o<1$. Initially, ^{4}He is admitted to an empty aerogel and there is a region where the reduced pressure increases slowly with amount adsorbed. A knee is found at a coverage of ~1.5 mmol and pressure $P/P_o \sim 0.06$. In the pressure range $0.06<P/P_o<0.75$ the reduced pressure increases linearly with added ^{4}He. Note at $P/P_o = 0.75$ the aerogel is about ¼ full. In the range $P/P_o>0.75$ there is a dramatic increase in the amount of ^{4}He adsorbed as the pressure approaches the saturated vapor pressure.

Starting from the filled aerogel, ^{4}He is then desorbed, resulting in the open symbol curve. Desorption follows a different path for $P/P_o< 0.97$ and Fig. 2.3.2.1 displays a hysteresis loop which closes at $P/P_o \sim 0.82$. While this isotherm should satisfy the linearity of the BET equation (eqn. (2.3.2)), due to the compressibility of helium the areal coverage of ^{4}He atoms depends on the substrate-helium interaction and is thus not accurately known. Therefore, while the monolayer coverage can be determined from a BET plot of a helium isotherm, the total surface area of the sample cannot. The surface area is usually determined via nitrogen isotherms.

The hysteresis loop is a result of capillary condensation which is the relaxation of a developing Kelvin instability [46]. If we assume cylindrical pore geometry (length l, radius r), then as the thickness of the adsorbed film approaches the radius of the cylinder, at some well defined length dependent thickness the energy contained in the surface overcomes the desire of the adsorbent to wet the surface and the pore fills, effectively

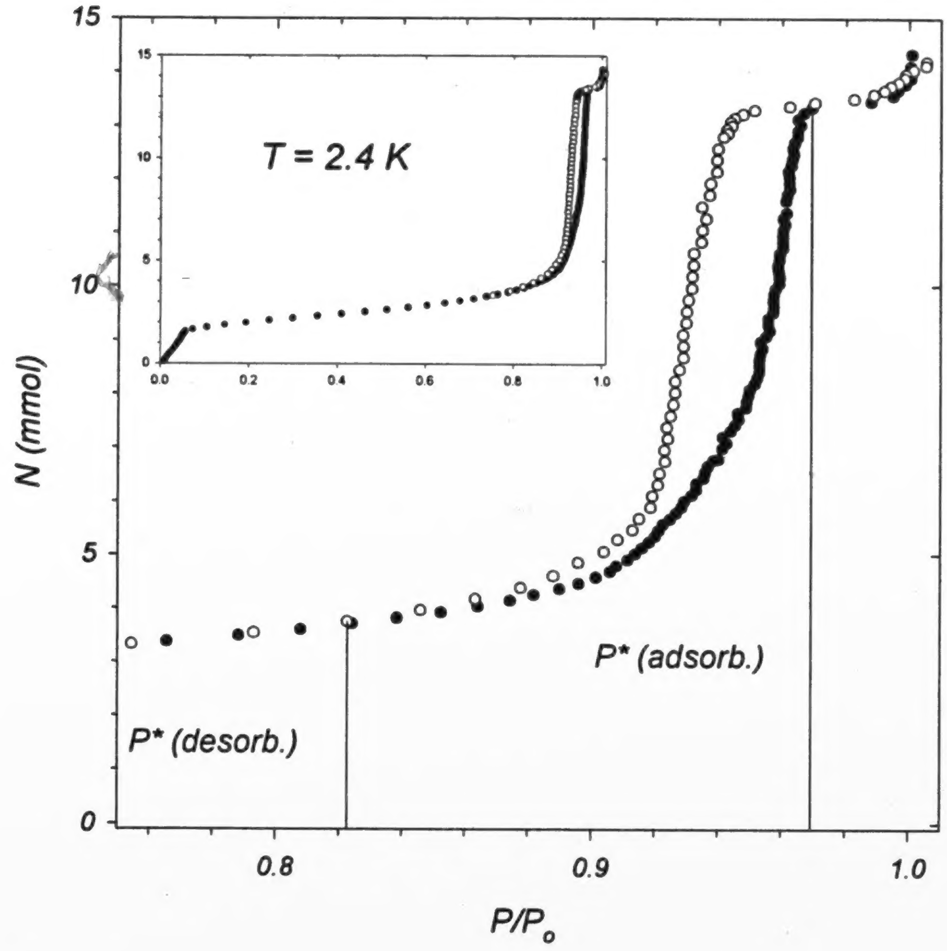

Figure 2.3.2.1. ^{4}He liquid-vapor isotherm in 87% aerogel at 2.4 K. Filled symbols are adsorption, open symbols desorbtion.

reducing the surface energy.

On desorption the opposite occurs. Initially, a cylindrical pore is completely filled and as the pressure decreases a concave spherical cap interface is formed at the ends of the pores. The instability occurs as the pressure decreases and the radius of curvature of the interface between liquid and vapor phases becomes smaller than the pore radius.

A simple relation between the pore size and the hysteresis loop can be derived by imposing both thermodynamic equilibrium between the phases and mechanical stability of the interface. The thermodynamic equilibrium condition is that the chemical potentials of the liquid and gas phases must be equal ($\mu^l = \mu^g$). Mechanical stability of the interface requires a pressure gradient across a liquid-vapor interface characterized by surface tension σ^{lv} as

$$P^l - P^v = C^{lv}\sigma^{lv} \qquad (2.3.2.3)$$

where C^{lv} is the mean curvature of the surface and can be positive or negative; the convention here is C^{lv} is negative if the center of radius is in the vapor which implies the pressure in the liquid is less than that of the surrounding vapor. Equating the chemical potentials and making use of eqn. (2.3.2.3), the Kelvin equation is written

$$\ln(P/P_o) = \frac{\sigma^{lv} v^l C^{lv}}{RT} \qquad (2.3.2.4)$$

The mean curvature C^{lv} is now considered with respect to adsorption and desorption. As gas is admitted to an empty porous medium it is adsorbed onto the walls and forms a liquid like layer. For a cylindrical pore the radius of curvature is infinite along the axis, so an adsorbed film has a mean curvature given by the pore radius, $C^{lv} = -1/r_p$. On the other hand, when the pores are saturated and liquid is being removed, the curvature is that of the (concave) spherical cap of liquid formed at the ends of the cylinder whose mean curvature is $C^{lv} = -2/r_p$. Using these values of the radius of curvature the Kelvin equation gives the pressure, P* , for equilibrium

$$\ln(P^*/P_o) = \begin{cases} -\dfrac{\sigma^{lv}v^l}{RTr_p} & \textit{adsorption} \\ -\dfrac{2\sigma^{lv}v^l}{RTr_p} & \textit{desorption} \end{cases} \qquad (2.3.2.5)$$

Applying these equations to the helium isotherm above gives a measure of the pore size distribution. For aerogel similar in porosity to that used in this work, r_p ranges from ~ 50 to 150 Å. It should be noted that the concept of pores in aerogel is a bit incongruous; instead one might interpret r_p as a characteristic separation of the strands.

2.4. Helium in Porous Media

As well as ultrasonic techniques to be described later, several other techniques have been used to investigate helium mixtures in aerogel. Torsional oscillator and heat capacity measurements will now be discussed in the context of the 98% aerogel.

The torsional oscillator technique described above has also been applied to helium in porous media [47]. By designing very high Q oscillators, Reppy and co-workers were able to achieve high sensitivity making it possible to study the critical behavior of ^{4}He (both films and full pores) confined in a number of porous media [17, 18, 44, 48, 49]. Later, heat capacity and torsional oscillator measurements were combined so simultaneous measurements could be made on the same sample.

Of fundamental interest in the study of the critical behavior of helium in porous materials has been studying the effects of randomness and confinement on the universality of the transition. Introduction of a solid matrix should change the topology and perhaps the dimensionality of the phase transition; universality predicts changes in the critical exponents with the dimensionality of the transition. In helium there are two experimentally obtainable exponents, ζ and α, which describe the behavior of the order parameter and heat capacity, respectively, near the transition in terms of the reduced temperature; for bulk helium they are ζ=0.6717(4) and α=−0.013(3), respectively. When helium is contained in aerogel the superfluid exponent changes to ζ~0.813(4) quite different from the bulk value; this is in contrast to other well characterized materials such as Vycor where the exponent is essentially the same as bulk. Investigations of ^{4}He films have also been of interest. Recently, Crowell et al. measured the superfluid exponent of films adsorbed onto aerogel and found very similar behavior to films on Vycor and a return to essentially bulk values [48]; averaged over a range of film thicknesses, the exponent was ζ=0.63(3).

A singularity is found in the heat capacity measurements of full pore aerogel, but is distinctly different than that of bulk [17]; the aerogel singularity is more cusp-like than the logarithmic divergence seen in bulk. By comparison, a small heat capacity anomaly has been found in full pore Vycor [78] and for helium films on Vycor [50]. Both heat capacity and superfluid measurements of helium in aerogel display very sharp transitions, comparable to the transition in bulk [17, 18]. The difference in the behavior of bulk and saturated aerogel helium has been ascribed to long range correlated disorder in aerogel [17, 18, 48].

Torsional oscillator and heat capacity techniques have also been applied to helium mixtures in aerogel [16]. Figure 1.1 is the phase diagram as determined from torsional oscillator measurements. The solid line is the bulk helium mixture diagram as described above, while the symbols represent the phase diagram as inferred from torsional oscillator measurements. The open symbols indicate a superfluid transition that continues to low temperature even at high ^{3}He concentrations. In contrast to bulk mixtures the coexistence region (filled symbols) is seen to be *detached from the lambda line*. A description of the experimental results leading to this intriguing diagram is presented below.

First and foremost torsional oscillators are sensitive to the moment of inertia of the fluid-aerogel torsion bob. This is ideal for detection of the superfluid transition since below T_λ the superfluid component decouples from the aerogel and the period of oscillation decreases in proportion to the superfluid density. That is, only the normal component of the fluid contributes to the moment of inertia and eqn. (2.1.1.1) predicts the period varies as the root of the moment of inertia. This decrease in period was used to map out the open circles in Fig. 1.1. As the phase diagram suggests, a decrease in the period was found for virtually the entire range of ^{3}He concentrations, the lowest transition temperature occurring at T_λ~200 mK and X~0.96. Further, when the ^{3}He concentration was below 0.8, a second, more subtle, feature was detected in the torsional oscillator data. At some temperature below T_λ, 'jumps' were detected in the period, as were 'dips' in the amplitude of the oscillator (the amplitude is inversely proportional to the dissipation experienced by the oscillator). As more ^{4}He was added the period became hysteretic on thermal cycling cooling below a characteristic temperature. The jumps and dips and the onset of hysteresis were attributed to crossing of the coexistence boundary and represent the filled circles in Fig. 1.1.

Heat capacity measurements have also been made on helium mixtures contained in 98% aerogel [51]. In bulk helium, the lambda transition is continuous and has a logarithmic divergence in the heat capacity at T_λ. Phase separation in helium mixtures is a first order transition with a latent heat of mixing, and there is a jump discontinuity in the heat capacity at T_s. All of these features become smaller and eventually disappear as the tricritical point is approached.

N. Mulders et al. used an AC calorimetry technique to corroborate the mixture phase diagram inferred from the torsional oscillator measurements on 98% aerogel [51].

A synopsis of their heat capacity results is shown in Fig. 2.4.1. The X=0.44 curve is indicated by the line and shows a prominent peak in the heat capacity, C, at the lambda transition T_λ~1.25 K. As the temperature is decreased through T_s~0.8 K a jump is seen in the heat capacity at phase separation. Increasing X moves the heat capacity peak to lower T_λ and the jump in C at phase separation evolves into a region of negative dC/dT. At concentrations above X>0.8 no phase separation is detected, in agreement with torsional oscillator measurements.

Several notable features were pointed out by Mulders et al. First, in the concentration region 0.64<X<0.88, the amplitude of the heat capacity peak does not decrease with increasing X, in contrast to the X<0.64 region where the decrease in amplitude with increasing X is quite dramatic. In this same region the superfluid density measurements showed a broadening of the lambda transition. Comparing the heat capacity data for mixtures in aerogel to that of bulk mixtures quite convincingly displays the continuation of the heat capacity peak to low temperatures for X>0.8. This agrees with the torsional oscillator measurements and implies that the coexistence region is completely contained within the superfluid phase.

The intriguing detachment of the coexistence region has prompted several theoretical investigations [22-25]. Two of these modeled aerogel by introducing randomness into the crystal field term in the BEG model. Since this term is invariant under the symmetry breaking of $S^z_i=\pm1$, it constitutes a bond interaction for the superfluid transition. This "random bond" is a somewhat new approach as porous media have usually been associated with random field systems [13, 52]. Maritan et al. used a mean field theory approach to show that introduction of quenched (spatially fixed) randomness in the BEG Hamiltonian caused the tricritical point to become unstable resulting in the lambda being detached from the coexistence curve [25]. Falicov et al. "grew" a structure that mimicked aerogel on an LxLxL lattice both in its connectivity and its density [23]. The effect of the aerogel was to preferentially attract the ^{4}He isotope due to its lower

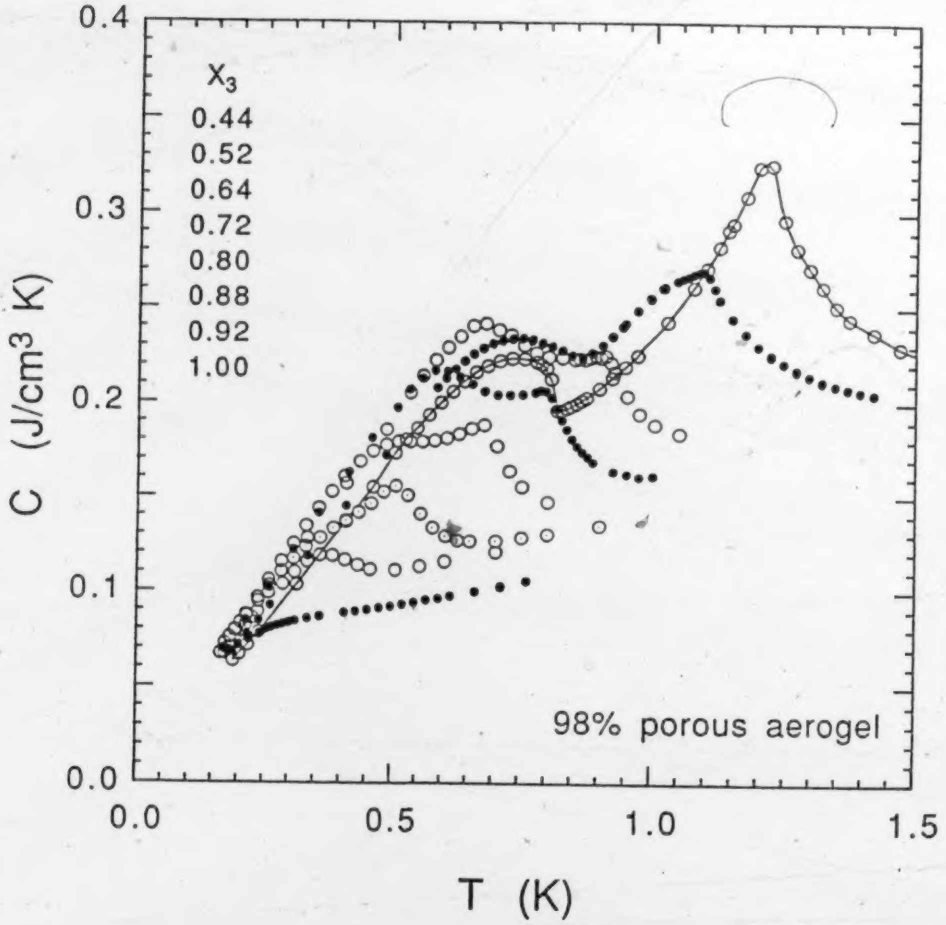

Figure 2.4.1. Heat Capacity of Helium Mixtures in 98% Aerogel. Data courtesy of M. Chan.

zero point motion. Randomness was introduced as a site dependent crystal field term. Monte-Carlo simulations where used to determine the phase diagram based on the BEG Hamiltonian and resulted in a phase diagram very similar to that determined in the 98% aerogel, with the lambda line detached from the coexistence region.

While the above studies have focused on the randomness and connectedness of the aerogel structure, Pricaupenko et al. studied the effects of confinement on the phase separation of helium mixtures [22]. They used a non-local density functional formalism to describe helium mixtures confined between two narrowly separated plates. Contrary to previous investigations which considered ^{4}He to be localized at the substrate, the calculations of Pricaupenko et al. indicated that, except for a strongly bound layer of ^{4}He occupying the first few layers, mixing was enhanced at the substrate.

From these results in the 98% aerogel the work in this thesis extends the study of helium mixtures to higher density aerogels where one might think that increasing the amount of impurity would amplify the experimental effects seen in the 98% aerogel. As will be shown in Chapter 5, this is not the case and mixtures in aerogel are governed by a "less is more" philosophy.

2.5. Propagation of Ultrasound in Porous Media

Ultrasonic velocity depends on the ratio of modulus to density. The number of ultrasonic modes which propagate depends on the nature of the supporting medium. This section introduces the fundamentals of ultrasonic propagation in fluid filled porous media.

2.5.1 Ultrasonic Modes

Aerogels are isotropic and so have only two independent elastic moduli, which can be taken to be the shear modulus μ_a and the bulk modulus K_a. Ignoring degeneracies in polarization, aerogels support two ultrasonic modes, compressional and transverse. Compressional, or longitudinal, modes are oscillations with particle motion parallel to the wavevector, i.e. along the direction of propagation. Transverse, or shear, waves displace the particles in a direction perpendicular (transverse) to the direction of propagation. Transverse modes require a shear restoring force, and so do not normally propagate in fluids.

The velocities of the two modes are usually expressed in terms of the bulk and shear modulus. If we consider solid silica with bulk density ρ_{Si} and moduli μ_{Si} and K_{Si}, and imagine removing some volume fraction ϕ to make an aerogel with porosity ϕ, then the porous material will have a density $\rho_a = (1-\phi)\rho_{Si}$ and moduli μ_a and K_a. The shear and longitudinal velocities are

$$v_s = \sqrt{\frac{\mu_a}{(1-\phi)\rho_{Si}}} = \sqrt{\frac{\mu_a}{\rho_a}} \qquad (2.5.1.1)$$

$$v_l = \sqrt{\frac{K_a + \frac{4}{3}\mu_a}{\rho_a}} \qquad (2.5.1.2)$$

Typical sound speeds for 87% porous aerogel (ϕ=0.87) are 600 and 300 m/s for the longitudinal and shear modes, respectively. At frequencies of 10 MHz the wavelength, λ is several 10's of microns, much larger than any characteristic length scale (i.e. pore radius, r_p ~ 100 Å, or strand size r_s~50 Å) in the aerogel so there should not be any significant scattering and the aerogel can be treated as a homogeneous continuous medium. Such long wavelengths also imply that acoustic strain gradients over a pore are small and the entire pore moves and is compressed almost uniformly in a passing acoustic wave.

Consider next what happens when the pores contain a fluid with density ρ_f and viscosity η. To illustrate the coupling between the pore wall and fluid, consider the oscillating solid box immersed in the fluid in Fig. 2.5.1.1. A transverse wave is shown here, but in an isotropic medium a longitudinal wave would produce similar couplings. Figure 2.5.1.1 shows two types of coupling associated with a passing sound wave. The "pushing" of the fluid by the top and bottom of the box is an inertial effect and will be discussed later in terms of the tortuosity. Of more immediate concern is the up-down motion of the sides of the box which exert a shearing force on the liquid. If the shear viscosity of the fluid is non-zero, the motion of the walls generates a viscous wave which penetrates a distance δ into the fluid. This "viscous penetration depth" is given by

$$\delta = \sqrt{\frac{2\eta}{\rho_f \omega}} \qquad (2.5.1.1)$$

and represents the distance over which the amplitude of the viscous wave decays to 1/e of its value at the wall. δ presents a convenient metric with which to characterize different regimes for ultrasonic propagation. We have tacitly assumed that we are in the 'hydrodynamic limit' where the mean free path of excitations in the liquid the pores is

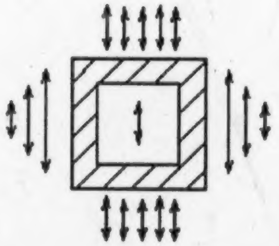

Figure 2.5.1.1. Sound Coupling. Coupling of solid strand to surrounding fluid.

smaller than the viscous penetration depth.

2.5.2 Low and High Frequency Regimes

If δ is much larger than the typical pore size ($\delta \gg \bar{r}_p$) the fluid is viscously locked to the porous material; this is the low frequency (or high viscosity) regime. In this regime the viscously clamped fluid contributes to the effective density which is written

$$\rho_{eff} = \rho_a + \phi\rho_f \qquad (2.5.2.1)$$

Since the fluid does not change the porous medium's shear modulus, the shear sound velocity for the low frequency regime is

$$v_s\big|_{\omega\to 0} = \sqrt{\frac{\mu_a}{\rho_a + \phi\rho_f}} \qquad (2.5.2.2)$$

so the sound velocity decreases when fluid is added. If the porous material is only partially saturated, i.e. an adsorbed film, $\phi\rho_f$ is replaced by the fluid per unit volume (the average fluid density).

Consider next the high frequency (or low viscosity) regime. When ω is large enough the viscous penetration depth is much smaller than the pore size, $\delta \ll r_p$ and most of the fluid is not viscously coupled to the pore wall. Since the fluid is decoupled from the solid matrix it should not contribute to the density, resulting in higher sound speeds. For complete decoupling, the effective density would be equal to the density of the empty porous material, $\rho_{eff} = \rho_a$. But recall Fig. 2.5.1.1, which illustrates the inertial coupling to the fluid which has so far been neglected; fluid above and below is "pushed" by the solid material. In the low frequency regime the fluid is viscously locked so inertial coupling is unimportant; in the high frequency regime it keeps part of the fluid coupled to the matrix.

There is also a third mode of propagation in the high frequency limit, the Biot 'slow wave', which is essentially a compression wave in the decoupled fluid.

2.5.3. Propagation in Helium filled Pores

Since He II has both a normal and a superfluid component, when porous media are saturated with superfluid helium the acoustic propagation involves both the low and high frequency regimes. At temperatures $T>T_\lambda$, the fluid is viscous and the acoustic propagation may be in the low frequency regime where $\delta>>r_p$. When T=0 K, there is no normal fluid ($\eta=0$) so sound propagates in the high frequency (low viscosity) regime. Between these two limits, the fluid has both a normal component and a superfluid component whose densities vary continuously with temperature. Further, these fluids can move relative to each other, so a porous material saturated with a superfluid is really a three-component system. This unique situation is examined in more detail below.

Above T_λ the viscosity of helium is ~25 μPoise which corresponds to a viscous penetration depth of δ~230 Å (for a 10 MHz sound frequency). This is only about twice the pore radius r_p~100 Å, as determined from the isotherm measurements, and hardly satisfies $\delta>>r_p$. However, low frequency propagation is still expected since in a porous medium with a range of pore sizes the high frequency crossover is determined by the smallest pores [53, 54]. This conclusion is supported by the lack of frequency dependence in superfluid decoupling for transverse waves in helium filled aerogel [55]. Below T_λ, the normal fluid density decreases, as does the viscosity. Torsional oscillator measurements [56] have found that below T_λ the viscosity of the normal component reaches a minimum at ~1.6 K of 11 μPoise. However, the normal fluid density decreases faster than η and δ increases monotonically below T_λ. Below 1.6 K the viscosity rises rapidly because the mean free paths of phonons and rotons increase (~200 Å) at low temperatures. When the mean free path is on the order of the r_p and δ the hydrodynamic description breaks down and the effect of the fluid should be described in terms of scattering excitations from the pore walls [53]. Adding ^{3}He to the superfluid decreases the mean free path of these excitations and limits the rise in the viscosity at low temperatures. At a concentration of X=0.5 the penetration depth of the normal fluid component (to which ^{3}He contributes) is δ~250 Å at 1.2 K, so the normal fluid component is still in the low frequency regime. The situation is much simpler for ^{4}He films where the viscous penetration depth is always greater than the film thickness, so the normal fluid component is always in the low frequency regime.

While the viscosity of the superfluid fraction is zero, some fluid may still be dragged by the walls. This coupling occurs because the superfluid density increases from zero at the pore wall to ρ_s in the pores over a distance roughly equal to the coherence length (ξ) and so fluid within a distance ξ will still be coupled to the walls. Since the coherence length scales with the inverse of the superfluid density (eqn. (2.1.2.4)), this effect will only be significant very near T_λ, $\delta \sim \xi << r_p$, otherwise, the superfluid fraction is always in the high frequency limit.

To reiterate, at and above the transition temperature, helium has a non-zero viscosity and is coupled to the pore motion reducing the sound speed. Below T_λ the normal fluid component is clamped to the pores but the superfluid component decouples from the matrix giving rise to an increase in the sound velocity. In this way ultrasonic shear velocity measurements are analogous to torsional oscillator measurements.

2.5.4. Tortuosity

The tortuosity, α, of a porous medium is a geometric quantity that determines the inertial coupling of the fluid to the matrix. In the high frequency limit only a fraction $1/\alpha$ of the fluid decouples, so the effective density is

$$\rho_{eff} = \rho_a + (1-1/\alpha)\phi\rho_{He} \tag{2.5.4.1}$$

The tortuosity is a measure of twistedness of the pores. If all pores are parallel to the displacement, all the fluid should decouple in the high frequency regime so $\alpha=1$. Pores perpendicular to the displacement would not allow any decoupling so $\alpha=\infty$. In isotropic solids like aerogels, the pores are randomly shaped and oriented giving an intermediate tortuosity. The shear sound velocity for the high frequency regime (corresponding to the T=0 limit for superfluid helium) is written

$$v_s|_{\omega\to\infty} = \sqrt{\frac{\mu_a}{\rho_a+(1-1/\alpha)\phi\rho_{He}}} \tag{2.5.4.2}$$

In the intermediate regime where both the normal and superfluid components are non-zero the shear velocity is

$$v_s|_{(0<T<T_\lambda)} = \sqrt{\frac{\mu_a}{\rho_a+\phi(\rho_n+(1-1/\alpha)\rho_s)}} = \sqrt{\frac{\mu_a}{\rho_a+\phi(\rho_{He}-\rho_s/\alpha)}} \tag{2.5.4.3}$$

where $\rho_{He}=\rho_n+\rho_s$.

2.5.5. Longitudinal Modes

Only shear waves have been discussed up to this point to emphasize the sensitivity of velocity measurements to the effective density. For longitudinal modes, the bulk modulus of the fluid also contributes to the sound speed. This contribution can be calculated using the Biot theory [57] making longitudinal velocity measurements also useful. For example, our measurements are in "the rigid frame limit" where the fluid is much more compressible than the matrix (K_{Si} , $K_a >> K_{He}$), and in the low frequency regime the bulk modulus is $K_{eff} = K_a + \Delta K_{He}$ [58], where

$$\Delta K_{He} = (1/\phi)\left(1-\frac{K_a}{K_{Si}}\right)^2 K_{He} \qquad (2.5.5.1)$$

resulting in a low frequency ($T \geq T_\lambda$) longitudinal velocity

$$v_l\big|_{\omega\to 0} = \sqrt{\frac{K_a+\frac{4}{3}\mu_a+(1/\phi)(1-K_a/K_{Si})^2 K_{He}}{\rho_a+\phi\rho_{He}}} \qquad (2.5.5.2)$$

In the high frequency limit the Biot theory predicts a further contribution to bulk modulus, so the longitudinal velocity in the rigid frame limit for T=0, is

$$v_l\big|_{\omega\to\infty} = \sqrt{\frac{K_a+\frac{4}{3}\mu_a+(1/\phi)(1-K_a/K_{Si})^2 K_{He}-(1/\alpha)(2-\phi-K_a/K_{Si})K_{He}}{\rho_a+(1-1/\alpha)\phi\rho_{He}}} \qquad (2.5.5.3)$$

Finally the ratio of the low to high frequency ($T>T_\lambda$ to T=0) velocity changes for longitudinal and shear waves is

$$\frac{\Delta v_l/v_{lo}}{\Delta v_s/v_{so}} \approx 1 - \frac{(\rho_a+\phi\rho_{He})}{\phi\rho_{He}}\frac{(2-\phi)K_{He}}{K_a+4\mu_a/3} \qquad (2.5.5.4)$$

This equation can be checked using experimentally determined sound velocity data shown in Figure 2.5.5.1. The three velocity curves correspond to 11 and 12.5 MHz longitudinal data and 6.5 MHz shear data with the aerogel pores saturated with a helium mixture containing roughly 10% ^{3}He. The background has been subtracted for all three curves. Figure 2.5.5.1 shows the longitudinal modes experience a 5.9% change in the velocity, whereas the shear mode velocity increases by 7.25%, giving a ratio of 0.81 between the two modes. Using the values ϕ=0.87, ρ_{He} corresponding to a 10% ^{3}He concentration ~ 0.12 g/cc, ρ_a = 0.36 g/cc and the ratio of the moduli as determined by

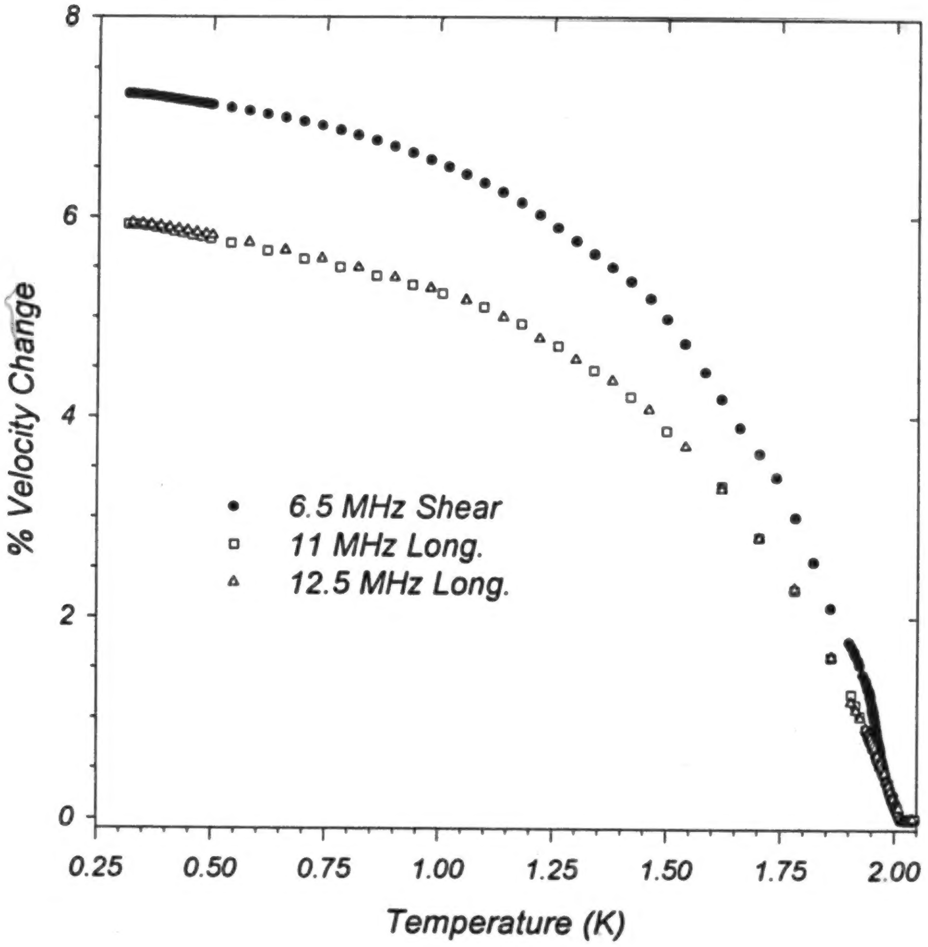

Figure 2.5.4.1. Velocity curves of 6.5 MHz shear and 11, 12.5 MHz longitudinal modes for a 10% mixture. The longitudinal modes have a lower bulk modulus contribution in the high frequency (low temperature) regime so the increase in velocity is smaller than that of the shear mode.

absolute velocities of the empty aerogel and the helium mixture, eqn. (2.5.5.4) gives a ratio of 0.75. This agrees well with the experimental data in Fig. 2.5.5.1. So while we understand the discrepancy between the two sound modes, all quantitative measurements are made from shear modes where possible.

2.5.6. Ultrasonic Attenuation

The Biot theory also predicts attenuation due to viscosity in the two regimes. The low frequency attenuation is expected to scale as $\alpha \sim \rho_n^2/\eta$, while in the high frequency regime $\alpha \sim (\rho_n \eta)^{1/2}$. Any critical attenuation peak due to criticality in the fluid [54] would be superimposed on this background.

Ultrasonic measurements on ^{4}He (both films and full pores) in Vycor and aerogel show a sharp peak at the superfluid transition. For helium films in Vycor this peak broadens above about 10 MHz and appears to be associated with vortex motion [44]. A similar mechanism may be responsible for the critical peak in full pores, or it may indicate coupling of the sound wave in the solid to fluctuations in the helium.

In contrast to continuous (second order) transitions, a first order transition should not have a critical attenuation peak since critical fluctuations are not present. However, the attenuation may still be sensitive to phase separation in a number of ways. Scattering of acoustic waves will occur if the dimensions of structures in the medium are of size comparable to the sound wavelength, λ, and is analogous to Rayleigh scattering of light. Phase separation in aerogel could result in domains of each phase with the interface effectively pinned by the aerogel matrix. If the domains are large, $\lambda \sim 10$ μm, then the acoustic wave will be strongly scattered according to [67]

$$\alpha \approx 8.7 \frac{2\pi^3 f^4}{3v^3} \frac{kT}{K_b} \, dB/cm \qquad (2.5.6.1)$$

where K_b is the bulk modulus, and f and v are the sound frequency and velocity. Motion of interfaces in response to a sound wave may also cause dissipation and be seen as an increased attenuation once phase separation occurs. If the pinning of the interfaces by the aerogel matrix is history dependent, the resulting hysteresis should appear in the attenuation.

Chapter 3
Experimental Methods

Low temperature experiments depend on successful integration and application of many subsystems. This work is no exception, with a dilution refrigerator to provide temperature stability from 2 K down to 100 mK, a pulse-echo ultrasonic spectrometer used to probe the sample, an accurate gas handling system to admit and remove the helium mixtures and a mass spectrometer to provide accurate concentration corrections. Measurements cannot be made of course, if the sample, or any of the cryogenic systems, does not survive the deep freeze; these breakdowns are euphemistically referred to as "the joys of low temperature physics."

The following chapter describes the experimental and sample preparation techniques. Each subsystem is described in some detail with the chapter culminating in the description of a typical experimental run.

3.1. Ultrasonic System

Ultrasonic velocity and attenuation were measured using a pulse-echo technique.

The primary objective is the detection of small changes in the velocity and attenuation due to changes in sample properties; this is in contrast to measurements of the absolute ultrasonic velocity or attenuation. Typically, two transducers are mounted at opposite ends of the sample; one transducer generates an ultrasonic pulse and the other receives the transmitted pulse. To obtain absolute measurements of the velocity the transit time of the pulse (τ) through the sample must be measured. With current digital oscilloscopes, 1 percent accuracy is easily achievable. However, knowing τ to a high degree of accuracy is insufficient in some cases for the determination of the absolute ultrasonic velocity. For example, in experiments presented here the transducers are attached to the samples using a thin layer of epoxy. The thickness of this bond and the ultrasonic velocity in the epoxy are unknown and therefore add uncertainty to any absolute measurement of the ultrasonic velocity in the sample. Similarly, the absolute attenuation cannot be accurately measured because the boundary conditions are not known. All this aside, with the current ultrasonic system we can measure small changes in the ultrasonic attenuation (0.01 dB resolution) and velocity (few parts in 10^6).

Changes in velocity are detected by comparing the phase of the signal transmitted through the sample to the phase of a reference signal. Assuming the thickness of the sample (d), the initial transit time through the sample (τ) and the sound's angular frequency (ω) are known, the change in velocity is related to the change in the phase ($\Delta\phi$) by:

$$\frac{v-v_o}{v_o} = \frac{1}{1-\Delta\phi/\omega\tau} \tag{3.1.1}$$

where $v_o = d / \tau$ is the reference velocity.

To detect changes in the phase of the transmitted signal a heterodyne technique is used. The basic philosophy behind heterodyne systems is the conversion of the radio frequency (RF) ultrasonic signals to a single intermediate frequency (IF). Any required signal conditioning (filtering, amplification, etc.) occurs at the IF. A heterodyne system allows the use of a wide range of sound frequencies while reducing effects of frequency dependence of electrical components used in the signal processing.

A schematic of the ultrasonic system is shown in Fig. 3.1.1. A continuous RF signal is applied to the Matec gated amplifier and the ultrasonic spectrometer. The gated amplifier produces a pulse of specified duration (~2 μs) at the applied RF; the spectrometer uses the continuous RF as the reference signal to which the phase of the transmitted signal is compared. From the gated amplifier the RF pulse passes through programmable attenuators before being applied to a piezoelectric transducer at the sample. Piezoelectric transducers convert the electrical pulse to ultrasonic energy that is transmitted through the sample (hopefully!) and detected using a second transducer. The received signal is immediately amplified using low noise broadband amplification and passed through another programmable attenuator and finally another stage of broadband amplification before phase detection.

The RF signals presented to the spectrometer are converted to the IF via mixing with a local oscillator (LO) signal of frequency $f_{LO} = f_{IF} - f_{RF}$, which results in frequencies f_{IF} and $(f_{IF} - 2f_{RF})$. The latter frequency is removed using a bandpass filter with a center frequency of 155 MHz (the IF frequency). As mentioned, the phase difference between the reference and the sample signal is used to determine the ultrasonic velocity via eqn. (3.1.1). To do this, the received signal is split into in-phase (x) and 90° out-of-phase (y) components. Mixing with the reference signal, which has also been converted to the IF, results in a DC signal corresponding to the magnitude of each component of the transmitted signal and a $2f_{IF}$ signal which is filtered out. The phase difference between the reference waveform and the transmitted signal is given by $\phi = \tan^{-1}(V_x/V_y)$, where V_x and V_y are the DC voltages averaged via boxcar integration. Equation (3.1.1) is then used to determine changes in the ultrasonic velocity using the measured phase change.

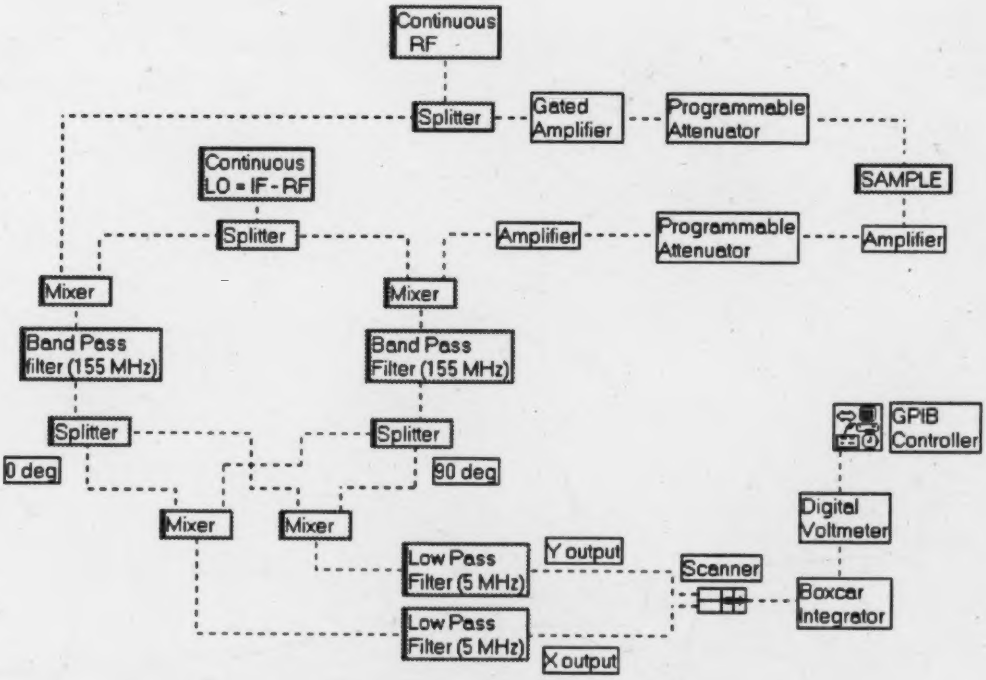
Continuous RF
Splitter
Gated Amplifier
Programmable Attenuator
SAMPLE
Continuous LO = IF - RF
Splitter
Amplifier
Programmable Attenuator
Amplifier
Mixer
Mixer
Band Pass filter (155 MHz)
Band Pass Filter (155 MHz)
Splitter
Splitter
0 deg
90 deg
GPIB Controller
Mixer
Mixer
Digital Voltmeter
Low Pass Filter (5 MHz)
Y output
Scanner
Boxcar Integrator
Low Pass Filter (5 MHz)
X output

Figure 3.1.1. Schematic of the ultrasonic pulse-echo heterodyne receiver system.

For more complete details of the ultrasonic heterodyne receiver the reader is directed to N. Mulders' Ph.D. thesis [44].

Ultrasonic attenuation is obtained in one of two ways. The first is simply via the magnitude of the x and y components of the phase measurement:

$$V_z = (V_x^2 + V_y^2)^{1/2} \qquad (3.1.2)$$

with the attenuation in dB given by

$$\alpha = 10\log (V_z^2) \qquad (3.1.3)$$

The second method is by direct measurement of the amplitude of transmitted signal. In this case, V_z is measured without phase detection and the attenuation is given by eqn. (3.1.3).

3.2. Thermometry and Temperature Control

Thermometry is not the problem it once was. For this work, a calibrated Ge resistance thermometer (Lakeshore Model GR-200) was used to measure the cell temperature. This same thermometer was used to provide feedback to the temperature controller and was attached directly to the oxygen free high conductivity (OFHC) copper (Cu) cell in which the sample was located. The heater controlling the sample temperature was attached directly to the mixing chamber of the dilution fridge. A digital resistance bridge (Quantum Design 1802) was used to measure the Ge thermometer resistance and provide the heater output. The above arrangement provided temperature stability of 0.1%.

3.3. Sample Preparation

Early attempts to study helium mixtures contained in aerogel [26] were made by placing an aerogel sample prepared for ultrasonic measurements in a cell containing bulk helium mixture. While this work showed that the superfluid and phase separation transitions were detectable using ultrasonic techniques, the presence of bulk helium meant that the exact mixture concentration contained in the aerogel could not be determined. The detectable features were time dependent, presumably resulting from a change in concentration due to diffusion from the bulk mixture. To alleviate this problem in this work, epoxy (Tra-Con BA-2151) was used to coat the aerogel-transducer sample thereby minimizing the amount of bulk helium in contact with the aerogel.

Aerogel samples were obtained from various sources. The 87% porous samples were made by L. Hrubresh at Lawrence Livermore National Laboratories. Higher porosity samples were generously supplied by N. Mulders et al. at Penn State University and some test samples were grown by Ying Xie and myself; only the 87% aerogel is investigated in this thesis. Most of the aerogel samples were prepared in small glass vials, but for ultrasonic measurements these cylindrical samples had to be cut into thin disks with parallel faces. Disks were cut using a high speed drill equipped with a diamond cutter. The drill was held stationary by clamping it to the drive shaft of a milling machine while the aerogel sample was held in the vise. The milling machine table was moved in the same linear direction during cutting to ensure the faces were as parallel as possible. This arrangement allowed for precise control of the cutting process; typically, aerogel samples were 3 mm in thickness, but samples have been cut as thin as 0.75 mm.

After cutting the aerogel samples, they were weighed and their volumes were determined geometrically. These simple measurements allow an estimation of the porosity using the equation:

$$\phi = 1 - \rho_a/\rho_{Si} \tag{3.3.1}$$

where ρ_{Si} is the density of bulk silica (2.21 g/cc). Knowledge of the open volume within the aerogel (ϕV_a) is also important to prevent overfilling of the sample since a bulk mixture in contact with a saturated porous medium may have a different ^{3}He concentration.

After this straightforward sample characterization, 20 MHz longitudinal $LiNbO_3$ transducers were epoxied to the faces of the cut aerogel. A filled epoxy, Tra-Con BA-2151, was used due to its high viscosity and quick drying nature, which should combine to cause as little damage to the aerogel sample as possible. Once dry, further epoxy was applied to the sample until the entire aerogel-transducer assembly was encapsulated. A hole was drilled through the epoxy at a point away from the transducers, into which a 0.25 mm i.d. capillary was epoxied. This capillary allowed helium to be admitted to and

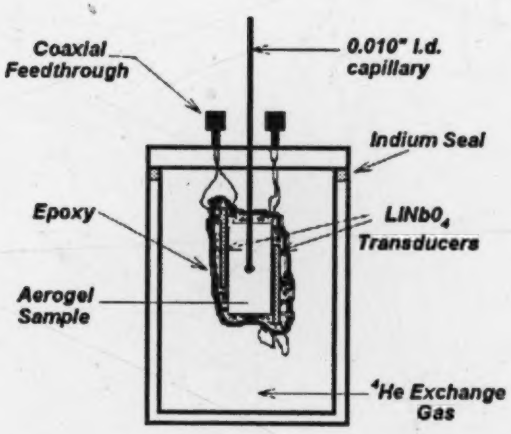

Figure 3.3.1. Schematic of epoxied aerogel sample contained in Cu cell.

removed from the aerogel sample. The completed sample was checked for leaks and sealed inside a OFHC Cu cell anchored to the mixing chamber of the dilution fridge. A feed-through in the lid of the Cu cell was necessary to facilitate the aerogel fill line capillary; a Cu-Ni capillary was fed through the Cu lid and epoxied in place. Both the aerogel sample capillary and the capillary leading to room temperature were soldered to this feed-through. Figure 3.3.1 displays the epoxied aerogel sample and Cu cell. ^{4}He exchange gas was admitted to the sealed Cu cell to insure thermal equilibrium of the aerogel and cell. It has been mentioned that below 250 mK ^{3}He would provide better thermal conductivity, however, ^{4}He was used in this thesis.

Early measurements indicated thermal anchoring of the capillary led to cold spots which made it difficult to fill the sample completely with no excess bulk mixture present. In subsequent measurements, a long capillary (~0.5 m) anchored only at 4 K was used to minimize the heat leak to the cell.

Sample characterization also included a nitrogen BET isotherm measurement to determine the surface area. Nitrogen was admitted from a room temperature gas handling system with a calibrated volume (Section 3.4). The aerogel was evacuated and flushed with helium several times and then cooled to 77 K. Nitrogen gas was admitted in controlled amounts and the resultant pressure was determined using a capacitance manometer (Setra Model 205-2). Since the aerogel strands are easily destroyed by capillary forces, the nitrogen reduced pressure was kept below $P/P_o<0.4$. The BET plot (Section 2.3.2) for this sample is shown in Fig. 3.3.2, and using 16 $Å^2$ as the surface area of a nitrogen atom, the specific surface area for the epoxy encapsulated 87% aerogel was found to be 410 ± 20 m^2/g, or 13.9 ± 0.7 m^2.

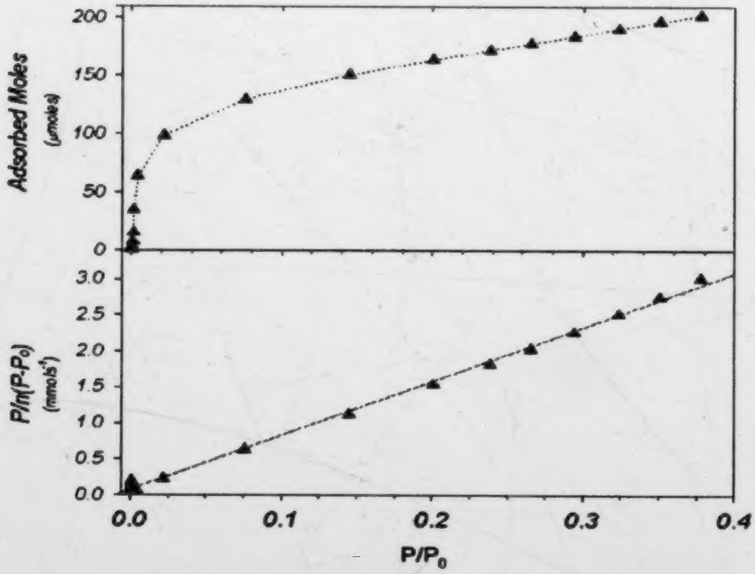

Figure 3.3.2. Nitrogen isotherm measurements on epoxy encapsulated 87% aerogel. Top graph displays the reduced pressure as nitrogen is adsorbed. Bottom plot is the BET equation plotted against the reduced pressure and the resulting least squares fit.

3.4. Mass Spectrometer and Gas Handling System

The addition and removal of ^{3}He and ^{4}He gases utilized a calibrated room temperature gas handling system (GHS). This GHS has been discussed previously [8, 9, 44] with only minor modifications for the present work. The basic layout of the GHS is (Figure 3.4.1) that of a calibrated volume (15.89 cc) and a capacitance manometer (Setra Model 205-2) connected to a series of valves to admit the helium gases from the storage tanks and to the cryogenic sample. Knowing the volume of the GHS, the ideal gas law can be used to determine the number of moles admitted to (removed from) the sample.

Throughout this work the ^{4}He (four 9's) was cleaned using a liquid nitrogen trap, but the ^{3}He was not. This unequal treatment was due to the incertitude of the treatment of the ^{4}He by my predecessors and the utilization of previously unused high purity ^{3}He. No blocking of the fill line occurred which, coupled with the inherent purity of liquid helium, justifies the above procedure.

Experimental work on the mixtures began with a determination of n_c, the ^{4}He inert layer coverage. n_c is the minimum ^{4}He coverage required for superfluidity at 0 K and was determined by admitting controlled amounts of ^{4}He into the aerogel sample until a superfluid transition was detected at the lowest base temperature (~250 mK). Once n_c was determined, ^{3}He was added to saturate the remaining pore space. To change the concentration of subsequent mixtures, the following procedure was used. The sample temperature was controlled at some convenient temperature above the superfluid transition temperature, the GHS was evacuated and the mixture vapor was allowed to expand into it. The amount of removed gas is then known from the GHS pressure, but its ^{3}He concentration (X) is not. However, the concentration of the vapor above bulk helium mixtures is tabulated as a function of temperature, giving a first order estimate of the concentration of the removed gas.

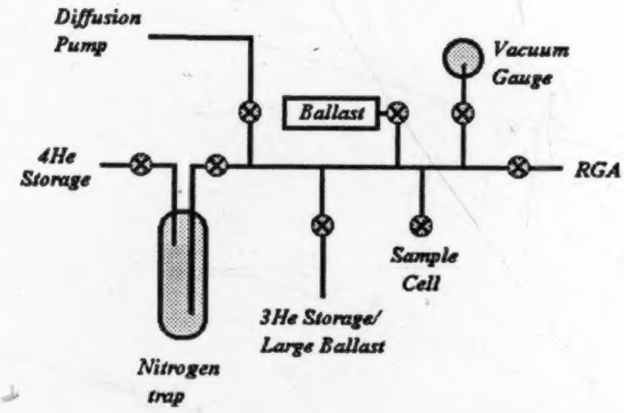

Figure 3.4.1. Gas handling system (GHS) used to admit and remove helium mixtures to the aerogel sample. RGA is residual gas analyzer.

However, as the concentration is varied from X=1 to X=0, the uncertainty in X will increase. To avoid having to periodically warm up and pump out the cell to produce known concentrations, a mass spectrometer was employed to accurately determine the concentration of the removed gas in the GHS.

A needle valve was used to admit the gas mixture to a mass spectrometer (Uthe Technology International (UTi), Model 100C) which was used to measure the relative partial pressures of the isotopes. These measurements of the relative concentrations of the helium isotopes were made at various time intervals to obtain average values. In this way improvements were made on tabulated measurements previously made on bulk mixtures. The procedure was checked by filling the sample with a known concentration in the middle of the range, on a separate run. The resulting transition temperatures in the nominally identical runs agreed to better than 1 percent.

Once the removed amount of each isotope was known, enough ^{4}He, and on occasion ^{3}He, was admitted to the sample at 1 K to achieve the desired concentration and to fill the aerogel sample. The different atomic volumes of ^{3}He and ^{4}He had to be considered in order to insure the sample was not over or under filled. Tabulated values of the molar volumes as a function of temperature are found in Wilks, as well as Progress in Low Temperature Physics, Vol. IV [2, 59].

3.5. Dilution Refrigerator

The concept of the dilution refrigerator is roughly thirty years old. My intention here is not to provide a detailed explanation of its operation or physical basis; I merely introduce the subject due to its importance in all aspects of this doctoral work. On the one hand, it is vital for the experimental measurements, and on the other, much of the theoretical framework of this dissertation was laid down during the early development of the dilution fridge. The physical basis behind the dilution fridge and this thesis is the phase separation of helium mixtures.

The underlying principle of the dilution refrigerator is that at 0 K the phase separation of the two isotopes is incomplete: pure ^{3}He and sits atop a denser ^{4}He rich phase containing a dilute amount (~6.4% molar concentration) of ^{3}He. In evaporative cooling, refrigeration is achievable through absorption of the latent heat of vaporization by the evaporating atoms. This process, however, is limited by the vapor pressure of the liquid; on cooling the vapor pressure falls rapidly and it becomes much more difficult to pump away the atoms. Dilution refrigeration is able to overcome the low pressure constraint and cooling occurs by absorption of the latent heat of mixing.

In order to take advantage of the latent heat of mixing and achieve these low temperatures it is necessary to continuously remove ^{3}He atoms from the lower ^{4}He rich phase. Figure 3.5.1 displays the clever idea employed to allow the continuous removal of ^{3}He from the ^{4}He rich phase: a tube directly connects a warm (700 mK!) region (the

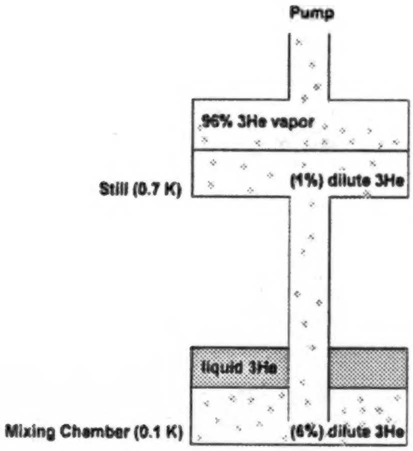

Figure 3.5.1. Schematic representation of a dilution fridge.

still), with the ^{4}He rich phase in the mixing chamber. Below ~1 K ^{4}He is entirely superfluid, has a very low vapor pressure and acts as a "massive vacuum" containing a dilute ^{3}He gas. In the still, the vapor pressure of ^{3}He is much higher than ^{4}He and is therefore pumped away. This depletion of ^{3}He in the still draws ^{3}He out of the ^{4}He rich phase in the mixing chamber, driven by an osmotic pressure gradient created by the temperature difference and the behavior of ^{3}He at different temperatures. Since the low temperature separated phases have concentrations of pure ^{3}He and 6.4% ^{3}He diluted in ^{4}He, removal of ^{3}He from the mixing chamber draws ^{3}He from the upper phase across the boundary to the ^{4}He rich phase and cooling occurs by absorption of the latent heat of mixing. This entire process is made continuous by circulation of ^{3}He; it is pumped from the still and is returned to the mixing chamber.

The above description, of course, greatly simplifies the system. On the theoretical side the fountain and osmotic pressures are very important, as are the exchange of heat between leaving and returning ^{3}He and the relative amounts of the isotopes in the fridge. However, the fundamental physical processes are apparent from the above description.

3.6. Computer Control

A typical data run involves all the above systems. Starting at some initial concentration, some of the mixture is removed. The amount of each isotope removed is calculated from the mass spectrometer measurements and an appropriate amount of each isotope is added to achieve the desired concentration. The sample is then cooled quickly to the base temperature (~250 mK) and left for a few hours.

Data collection is controlled by an IBM compatible personal computer and proceeds as follows. The desired set temperature is sent to the Quantum Design (QD) bridge which independently controls the temperature. A computer subroutine monitors the temperature, decides when it has stabilized, and then delays for a preprogrammed amount of time to ensure thermal equilibrium. After this settling time, digital voltmeters are used to read the voltages from the boxcar integrator corresponding to the x, y, and z components of the transmitted ultrasonic pulse. Having taken the required data, the computer instructs the QD bridge to stabilize at the next temperature set point. While stabilization occurs background data needed for drift compensation is acquired. This process is repeated until a full temperature scan is completed. A full scan typically is from 250 mK to above 1 K and then back again to 250 mK and takes about 24 hours.

Chapter 4

Helium Films in Aerogel

^{4}He films enjoyed an intense period of scrutiny when it was predicted they should undergo a Kosterlitz-Thouless (KT) transition [61]. As a result, there have been many previous studies of helium films on a variety of substrates [16, 44, 48, 49, 60,] and this chapter is primarily concerned with providing a background and comparison for the ^{3}He-^{4}He mixture measurements. In helium mixtures, ^{4}He is expected to be preferentially adsorbed to the surface of aerogel due to its lower zero point motion [16, 22, 23] and aerogel's large surface area suggests ^{4}He films may play an important role in the phase diagram of helium mixtures in aerogel. To this end, we present measurements on ^{4}He films adsorbed on the same 87% aerogel sample as used for mixture measurements discussed in Chapter 5. In particular, this chapter presents considerably more detail on tortuosity measurements. Because we are interested in the helium film behavior with respect to mixtures saturating the pores, the actual amount of ^{4}He adsorbed is reported as opposed to the coverage (moles/unit area) normally used when discussing films. This allows an easy conversion to equivalent ^{3}He concentration where it is assumed ^{3}He fills the pore space not occupied by the ^{4}He film. In this chapter our interest lies in the fact that helium films exhibit superfluidity with a thickness-dependent transition temperature, generically denoted by T_λ.

4.1. Previous Measurements

The KT transition is a 2-dimensional (2-D) vortex-antivortex binding [62] transition which results in superfluid behavior below a critical temperature, T_c. The KT transition on a flat substrate is characterized by a sudden disappearance of the superfluid density at T_c; however, measurements at finite frequencies and non-planar substrates broaden the jump into a continuous transition. Among other things, KT theory predicts the height of the superfluid density jump at the transition temperature and a linear relation between T_c and helium film coverage (μmol/m^2). In contrast to three-dimensional (3-D) bulk behavior, the KT transition has no associated ρ_s exponent and no heat capacity singularity.

Extensive measurements to determine the critical behavior of ^{4}He films on 91% and 95% aerogel have recently been made using torsional oscillator and heat capacity techniques [48, 49]. For films with transition temperatures less than 1 K, the critical behavior is similar to that of films on Vycor; the superfluid density exponent is $\zeta=0.63\pm0.03$, which is more bulk-like than the full pore aerogel where $\zeta=0.811\pm0.004$ [48]. Unlike Vycor however, no heat capacity anomaly was detected for ^{4}He films on aerogel, consistent with results reported by [51].

4.2. General Trends in Ultrasonic Velocity and Attenuation

This section introduces the ultrasonic measurements for pure ^{4}He films on the 87% porosity aerogel by showing how the sound velocity and attenuation evolve as thicker films are adsorbed and superfluidity appears. Figure 4.2.1 shows the velocities of 6.5 MHz shear waves for a series of adsorbed films. The top curve is for 373 μmol of ^{4}He, the bottom curve is for 480 μmol. As more helium is adsorbed the added mass

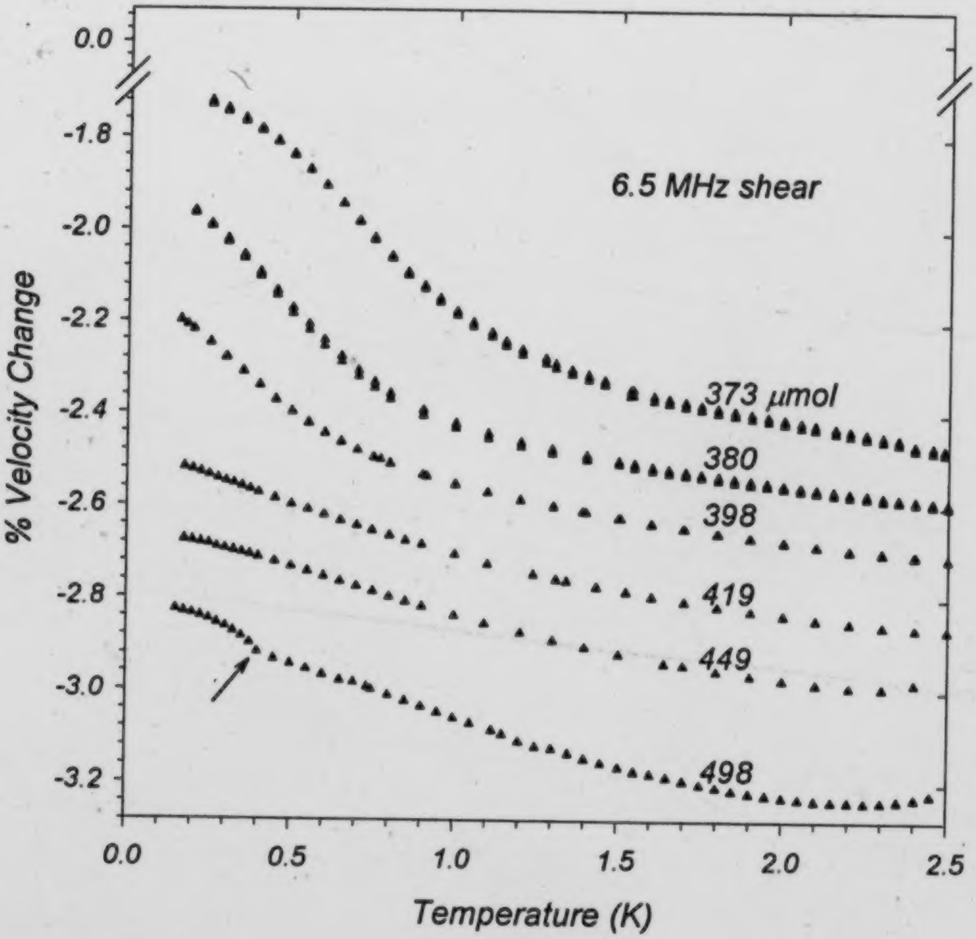

Figure 4.2.1. General trends in the ultrasonic velocity as ^{4}He is added for a 6.5 MHz shear mode. From top to bottom, the curves correspond to fillings n= 373, 380, 398, 419, 449, 498 μmol. The arrow indicates the onset of superfluidity.

results in a decrease in the sound speed. The spacing between these curves is due to the mass loading of the aerogel.

The broad increase in velocity below 1 K and the more gradual change at higher temperatures are due to interaction of the sound wave with the "two level systems" (TLS) that dominate the low temperature behavior of glasses. The suppression of the TLS velocity increase and its shift to lower temperatures as more ^{4}He is added have been studied in Vycor [44] and reflect the interaction between TLS of the aerogel and the adsorbed helium at its surface. Superfluidity first appears for the bottom (498 μmol) film and is seen as a kink in the velocity around 400 mK (indicated by the arrow) superimposed on the TLS background. The kink indicates the temperature where the helium film superfluid density becomes non-zero. Decoupling of the superfluid from the aerogel matrix lowers the effective density and causes the increase in the sound velocity. Not all the adsorbed helium decouples (the velocity at T=0 K is not identical with that in empty aerogel); only the amount of ^{4}He above a critical coverage n_c becomes superfluid.

Figure 4.2.2 displays the corresponding attenuation curves. Here the curves are offset vertically for clarity. Again, the top curve corresponds to the lowest filling and the bottom to ~498 μmol. The broad peak in the attenuation, also due to TLS, decreases and shifts to lower temperature as helium is adsorbed. The attenuation decreases at the lowest temperatures for all ^{4}He coverages. The bottom most curve, where superfluidity first occurs, shows a small critical attenuation peak, indicated by the arrow, at the same temperature as the sudden increase in velocity, T_λ~400 mK.

As expected, there are two markers for the onset of superfluidity in porous aerogel. The first is a sudden increase in the sound velocity as the superfluid decouples from the aerogel, the second is a critical attenuation peak as discussed in Section 2.5.6. An example of the superfluid transition in a helium film is shown in Fig. 4.2.3, which displays the velocity (filled symbols) and attenuation (open symbols) for a 6.5 MHz shear

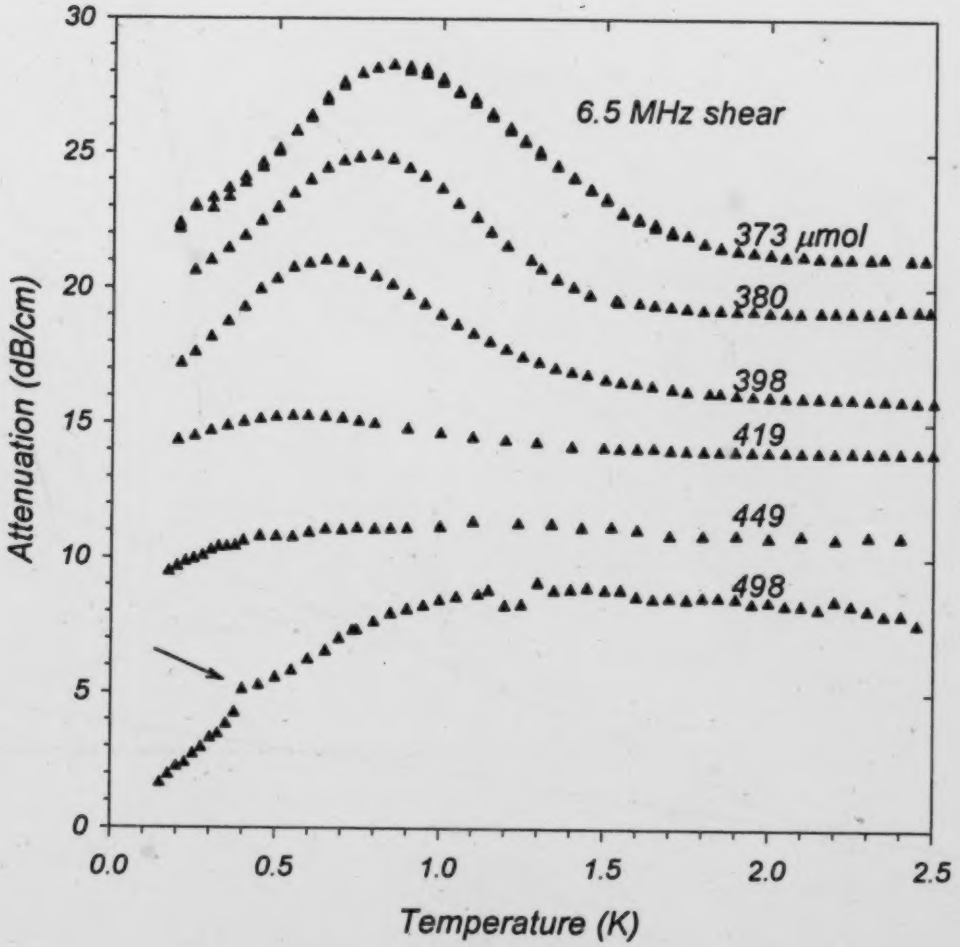

Figure 4.2.2 General trends in the ultrasonic attenuation as ^{4}He is added for a 6.5 MHz shear mode. From top to bottom, the curves correspond to fillings n=373, 380, 398, 419, 449, 498 μmol. The arrow shows the critical attenuation peak.

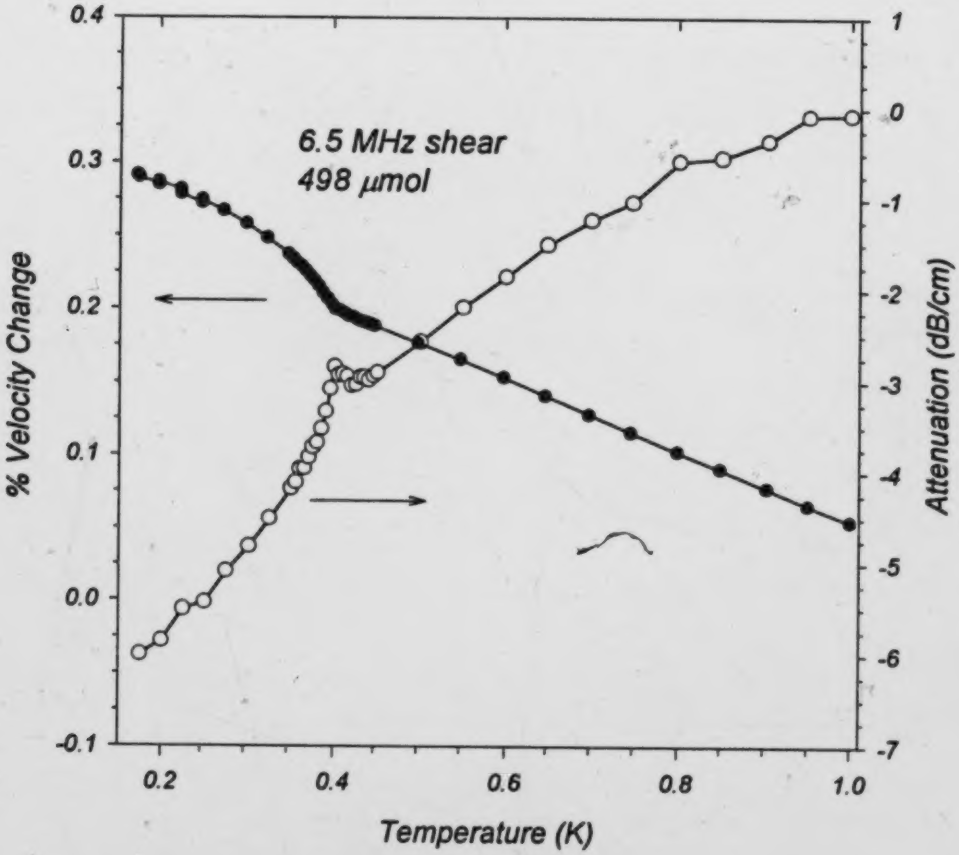

Figure 4.2.3. Velocity and attenuation data for a 6.5 MHz shear mode showing the transition region. The filling is 498 μmol. Note the increase in the velocity and corresponding attenuation peak. The lines are guides to the eyes.

mode. The film consists of 498 μmol of ^{4}He, or a coverage of 34.5 μmol/m^2. The velocity scale, shown here as a percent change, is on the left; the attenuation in dB/cm is on the right. At a temperature of 400 mK the film undergoes a superfluid transition resulting in a peak in the attenuation and a sharp increase in the velocity.

4.3. ^{4}He Inert Layer

Work on very thin films of ^{4}He on flat substrates has demonstrated the existence of a so-called "inert layer" of ^{4}He atoms which apparently do not contribute to the superfluidity [50, 62] (or at least to the decoupling). This inert layer is tightly bound to the substrate due to the large substrate-helium attraction potential. Usually the inert layer is defined as the minimum amount of ^{4}He needed for a superfluid transition at 0 K and is determined by an extrapolation of T_λ versus coverage (28 μmol/m^2 is a typical inert layer on flat Mylar) [63]. There are many factors which may contribute to the thickness of the inert layer such as the presence of ^{3}He [71], the curvature of the surface, and the interfacial thickness, none of which is well known. Recently, the inert layer has been reduced to 6 μmol/m^2 by pre-adsorption of H_2 onto a porous gold substrate [64]; presumably the hydrogen presents a lower attraction potential to helium.

Determining the inert layer for pure films adsorbed onto the 87% aerogel is straightforward. Temperature scans are completed for various amounts of adsorbed helium and transition temperatures are identified from the velocity increase due to decoupling. Figure 4.3.1 displays the transition temperature versus the amount of adsorbed ^{4}He. The lowest temperature at which a transition is detectable is 260 mK. Since heating of the sample had an appreciable effect on the transition temperature, data at very low fillings were acquired at low power input to the transducers. Unfortunately the low power decreased the resolution of the attenuation, so the critical attenuation peaks were unresolvable.

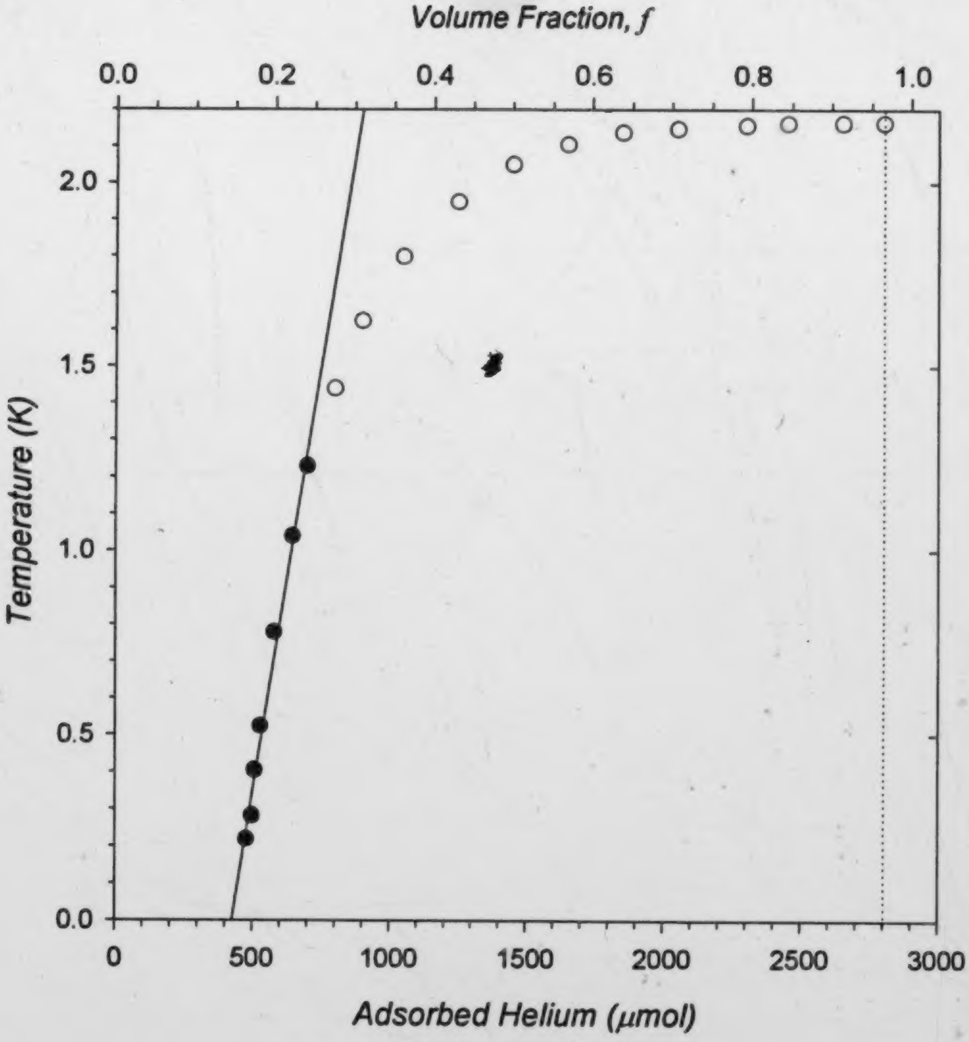

Figure 4.3.1. T_λ versus adsorbed helium for 87% aerogel. The linear regression is for the filled symbols. The T_λ=0 critical adsorption, n_c, is 427 μmol. The upper axis indicates the fraction of the pore volume occupied by the helium.

For transition temperatures below about 1.2 K the increase in T_λ is linear in adsorbed helium. At higher coverages the transition temperature begins to level off and approaches the temperature of the transition in saturated pores, ~2.16 K, indicated here by the dotted vertical line. The solid line shown in Fig. 4.3.1 is a linear regression fit to the transition temperatures shown as solid circles. Extrapolation to 0 K indicates that the inert layer, the amount of ^{4}He required for superfluidity at 0 K, is n_c=427 μmol. Dividing by the surface area (13.9 m^2) yields the critical coverage, $\sigma_c = 30.7$ μmol/m^2 , which is similar to (but between) previous measurements on 98% aerogel (Kim et al. found 36 μmol/m^2 [16]) and on flat Mylar substrates where $\sigma_c = 28.7$ μmol/m^2.

As we would like to compare the results of ultrasonic measurements on pure films to those on helium mixtures saturating the pores, the upper horizontal scale on Fig. 4.3.1 represents the volume fraction f occupied by the adsorbed helium. The bulk molar volume of ^{4}He at 1 K was used to calculate f.

4.4. Tortuosity Measurements

While it is true the superfluid fraction decouples from the matrix of a porous material, some of its mass may still contribute to the density as it is 'pushed' by the propagating sound wave. The tortuosity, α, which is a measure of this inertial coupling, can be determined from the fraction of superfluid which decouples

$$\rho_{decoupled} = \rho_s / \alpha \qquad (4.4.1)$$

Torsional oscillator measurements on superfluid helium often refer to the "χ factor," the fraction of ρ_s that remains inertially coupled to the oscillating substrate, which is related to the tortuosity by $\chi = 1 - 1/\alpha$.

One can also distinguish between a bulk tortuosity (α_{3D}) and a surface tortuosity

(α_{2D}). The bulk tortuosity is determined by the connectivity of the pores and is measured in experiments on fully saturated porous media using, for example, torsional oscillator or fourth sound techniques [65]. The surface tortuosity is measured in torsional oscillator or third sound experiments when thin films are adsorbed onto the substrate. For high porosity materials like aerogel, paths along the surface are generally more tortuous than those through the pores themselves, so $\alpha_{2D}>\alpha_{3D}$.

The tortuosity of the porous medium can also be determined from the shear sound velocity. If n_4 moles of helium is added to an aerogel, at $T>T_\lambda$ it is all coupled to the matrix and so will contribute to the density

$$\rho = (m_{aerogel} + m_4 n_4)/V_{aerogel} = \rho_a + \Delta\rho \qquad (4.4.2)$$

where $\Delta\rho = m_4 n_4/V_a$. The mass loading decreases the shear velocity ($v_s=(\mu_s/\rho)^{1/2}$) by an amount

$$\Delta_1 = \left.\frac{v-v_o}{v_o}\right|_{T>T_\lambda} = \sqrt{\frac{1}{(1+\Delta\rho/\rho_a)}} - 1 = -\frac{m_4 n_4}{2m_a} \qquad (4.4.3)$$

where $v_o=(\mu_a/\rho_a)^{1/2}$ is the velocity in the empty aerogel.

If the helium is cooled to 0 K where it is entirely superfluid, a fraction $1/\alpha$ decouples so the effective density is

$$\rho = \rho_a + \Delta\rho(1-1/\alpha) \qquad (4.4.4)$$

and the velocity change is

$$\Delta_2 = \left.\frac{v-v_o}{v_o}\right|_{T=0K} \approx -\frac{m_4 n_4}{2m_a}(1-1/\alpha) \qquad (4.4.5)$$

Two methods are used to obtain α from measurements of the sound velocity and the relevant quantities are shown in Fig. 4.4.1. The first method involves measuring $\Delta_1=\Delta v/v_o(T>T_\lambda)$ and $\Delta_2 = \Delta v/v_o(T=0\text{ K})$ with respect to a known background. Since the ^{4}He inert layer does not participate in superfluidity (n_c is the coverage required for a transition at T=0), measurements are made with respect to this coverage; Δ_1 and Δ_2 are now measured with respect to the inert layer, not the empty aerogel. However, as n_c is not known at the outset of the experiment, extrapolation is required to determine the velocities at T_λ and 0 K for the coverage corresponding to the inert layer, n_c. Once these inert layer velocities are known, Δ_1 and Δ_2 can be measured and the tortuosity for each film is found using

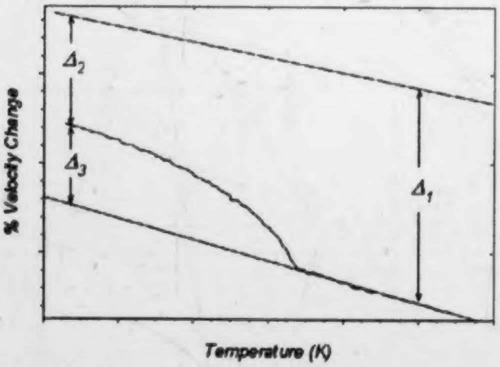

Figure 4.4.1. Definitions of quantities required for the calculation of the tortuosity. Note that Δ_3 is determined by subtracting the background and then taking $\Delta v/v_o$ at T=0.16 K.

$$\frac{\Delta_2}{\Delta_1} = (1-1/\alpha) \tag{4.4.6}$$

There are several details that should be mentioned. The first is that the velocities must be compared at the same temperature ($T>T_\lambda$) in order to account properly for background effects. Another consideration is that, regrettably, 0 K cannot be achieved in our lab, thus the assumption $\rho_n=0$ is probably not valid for the thinnest films. A fraction $\Delta\rho_s/\rho_{He}$ (<1) of the helium is in the superfluid component at T>0.2 K, so

$$\Delta_2 = \left.\frac{v-v_o}{v_o}\right|_{T=0.2K} = -\frac{m_4 n_4}{2m_a}\,(1-\frac{1}{\alpha}\frac{\rho_s(T)}{\rho_{He}}) \tag{4.4.7}$$

and Δ_1 is unchanged. Solving for the tortuosity gives

$$\alpha = \frac{\rho_s}{\rho_{He}}\left(1-\frac{\Delta_2}{\Delta_1}\right)^{-1} = \frac{\rho_s}{\rho_{He}}\,\alpha_{measured} \tag{4.4.8}$$

indicating the measured tortuosity is *larger* than the actual value for very thin films where $\rho_n \neq 0$.

An alternate method of determining the tortuosity is to extrapolate the background velocity contribution from above T_λ and subtract it. Usually the background above T_λ is fitted to a linear equation using points above the transition. This procedure is shown in Fig. 4.4.2. The top graph is the raw velocity data for a 6.5 MHz shear mode in aerogel with a ^{4}He coverage of 580 μmol (43 μmol/m^2). The line shows the extrapolated background using the velocity data above T_λ. The bottom graph is the velocity after this background has been subtracted. For films with high transition temperatures, this extrapolation may introduce systematic uncertainties into the calculation but, neglecting this, the tortuosity can be determined from the velocity change between T_λ and T=0

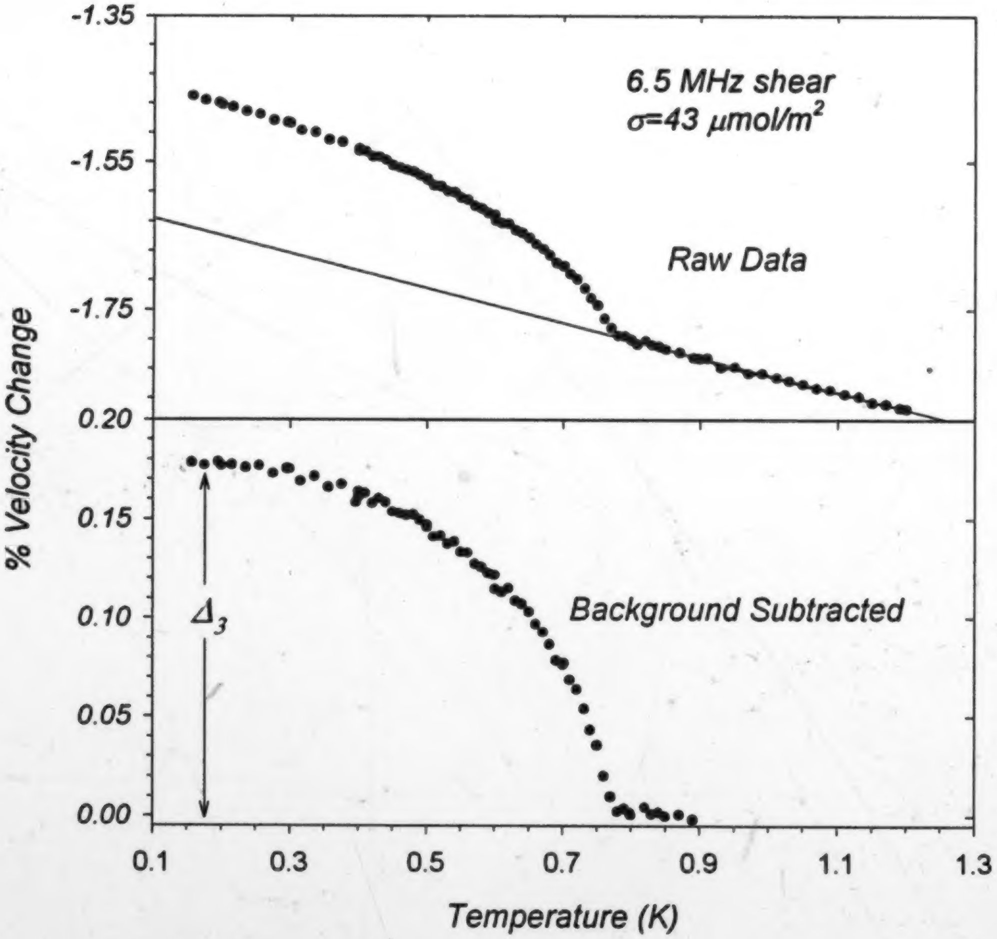

Figure 4.4.2. Example of background subtraction procedure for ^{4}He film velocity curve.

$$\Delta_3 = \frac{m_4(n_4-n_c)}{2m_a\ \alpha} \tag{4.4.9}$$

The parameter Δ_3 is defined in Fig. 4.4.1 and shown again in Fig. 4.4.2. Since only the extra helium above the inert layer will decouple, the number of ^{4}He atoms is n_4-n_c in eqn. (4.2.9); in the previous method this correction was accounted for by measuring all changes in velocity with respect to those at the inert layer coverage. Further uncertainty arises from imperfect knowledge of m_a as it may not be well defined in the epoxy coated aerogel. In this work, knowledge of the absolute tortuosity is not as important as its variation with ^{4}He coverage, so consistency is of primary importance. Within this framework there is an implicit assumption the changes in the sound velocity are not due to an interaction of the ^{4}He with the aerogel TLS and are solely density effects. The above procedures also assume that the mass sensitivity is the same at high and low temperatures.

Figure 4.4.3 shows velocity data for a series of films with the background subtracted, and illustrates the pitfalls of tortuosity measurements. All the data are for a 6.5 MHz shear mode; the coverages range from 480 μmol (35.6 μmol/m^2) to 646 μmol (47.9 μmol/m^2). The lowest coverage film (lowest T_λ) has a non-zero derivative at the base temperature; this indicates a substantial amount of the film is still normal fluid and therefore not decoupled. At somewhat higher coverages, the derivative is again non-zero at the base temperature, however, now it is positive. This change in derivative shows that the linear background extrapolation of the velocity from above T_λ is not adequate to correct for the "rounding" at low temperatures. The tortuosity would be calculated using the highest point of the plateau. Finally, the two curves with the highest T_λ show slight deviations in the shape of the velocity curve. This suggests inadequate correction for the background at intermediate temperatures, but should not seriously affect the tortuosity measurements which depend only on T~0 and $T>T_\lambda$ data.

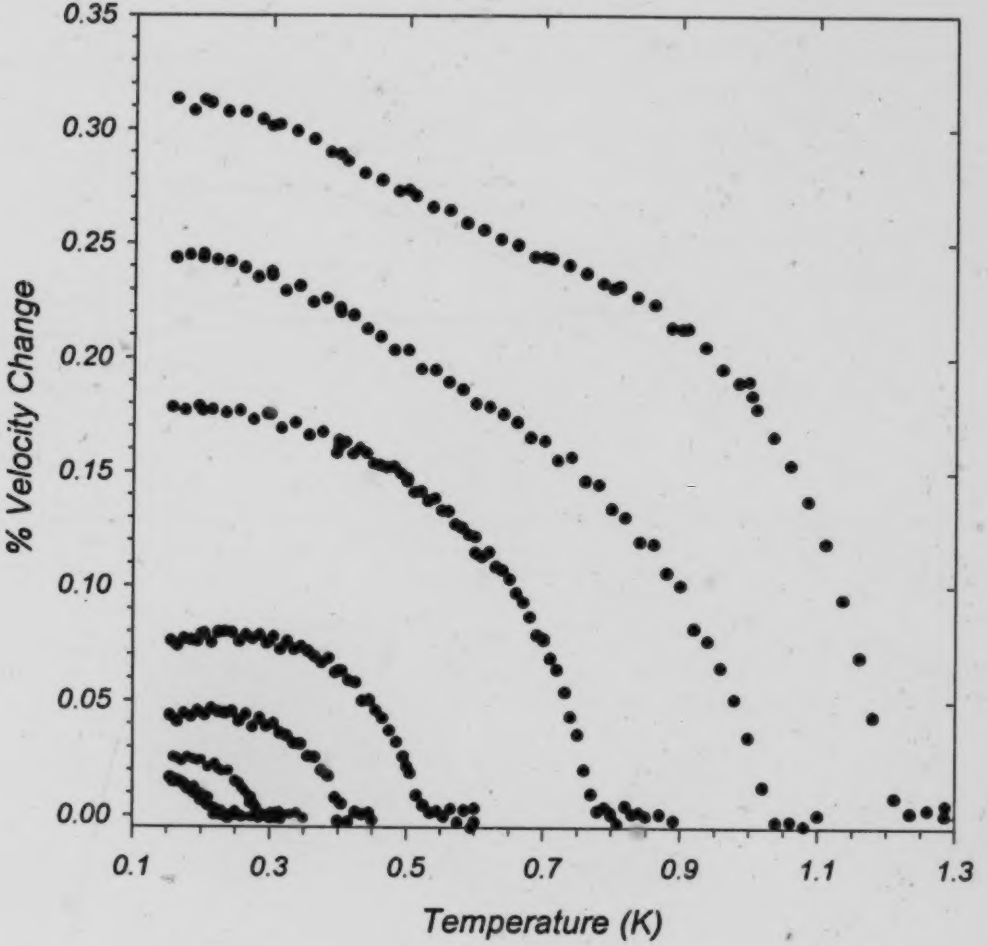

Figure 4.4.3. Series of films with backgrounds subtracted. n = 480, 490, 510, 530, 580, 646 and 700 μmol.

4.5. Tortuosity of Films

With the above methods of determining α, Fig. 4.5.1 shows 6.5 MHz data velocity curves for a series of ^{4}He adsorbed films with coverages ranging from empty (top) to 646 μmol (bottom). The first detectable transition is seen at $T_\lambda \sim 200$ mK for a filling of 480 μmol. Successive additions of ^{4}He decrease the velocity and increase T_λ. Figure 4.5.2 is a similar plot displaying the corresponding 11 MHz longitudinal velocity curves. Note the break in the vertical axis in both of these plots. For coverages near n_c the change in the velocity with respect to the empty aerogel is roughly -2.7% which necessitates the axis breaks.

The effect of the tortuosity is readily apparent from Figs. 4.5.1 and 4.5.2. If the superfluid decouples completely (α=1) then at T=0 any helium added beyond the inert layer coverage n_c will not change the velocity. Figures 4.5.1 and 4.5.2 clearly show that this is not the case. For example, compare the bottom two curves (filled circles and open triangles). The open triangles represent a filling of approximately 100 μmol more than the filled circles. Now consider three possibilities. First, if *all* the helium (inert layer included) were to decouple, the value of velocity at T=0 K should be that of the empty aerogel, or $\Delta v/v_o = 0$ as all velocities in Figs. 4.5.1 and 4.5.2 are compared to those of the empty aerogel (the upper most curve). Second, if all the helium which exceeded the inert layer ($n = n_4 - n_c$) were to decouple due to superfluidity, then the velocity at T=0 K should be that of the inert layer coverage (since the inert layer coverage is not known at the outset of the experiment the inert layer curve in Figs. 4.5.1 and 4.5.2 was re-constructed from the data afterwards). Since neither case describes the results shown in the above figures, only part of ρ_s must decouple implying a tortuosity α>1.

One more clarification on tortuosity measurements is required. As the thickness of the film increases, its morphology may change, hence the tortuosity may depend on the thickness of the adsorbed layer. Furthermore, as the inert layer is essentially a tightly

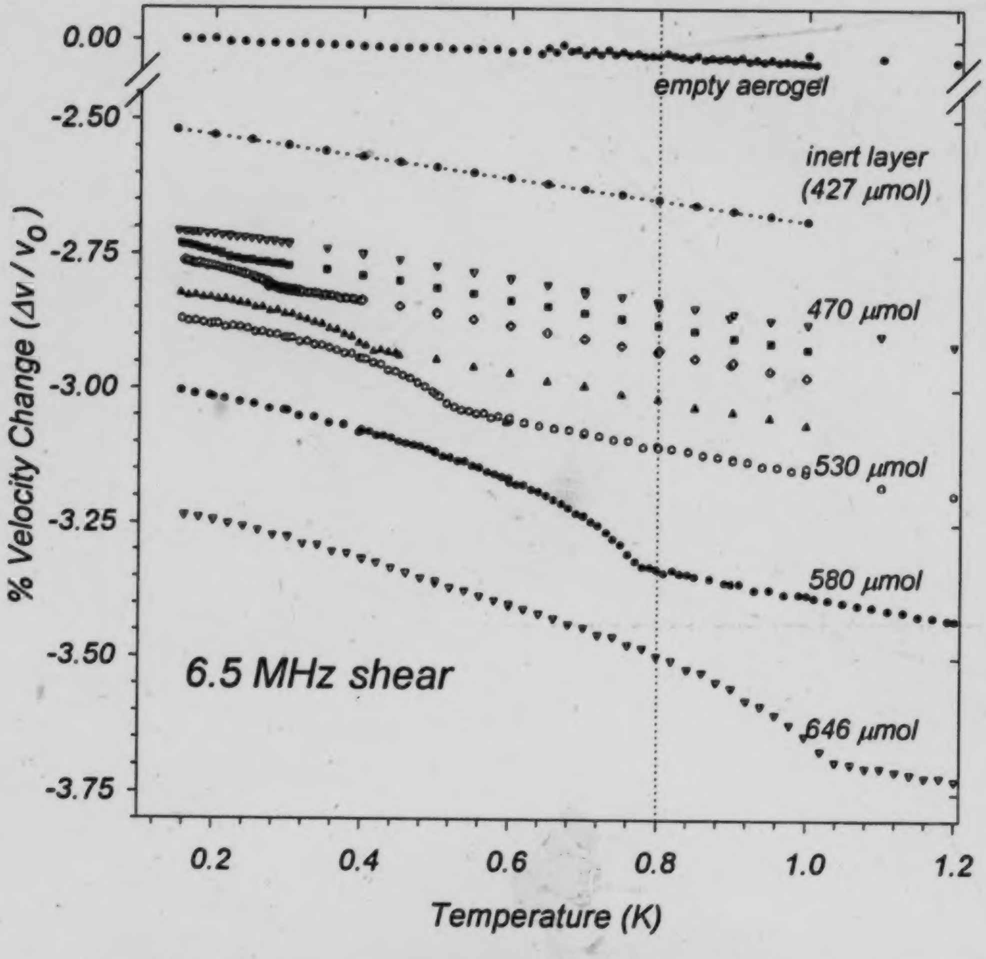

Figure 4.5.1. 6.5 MHz velocity data for helium films adsorbed on aerogel. Curves correspond to: empty aerogel, inert layer (see text), 470,480, 490, 510, 530, 580, 646 μmol. Note break in the velocity axis.

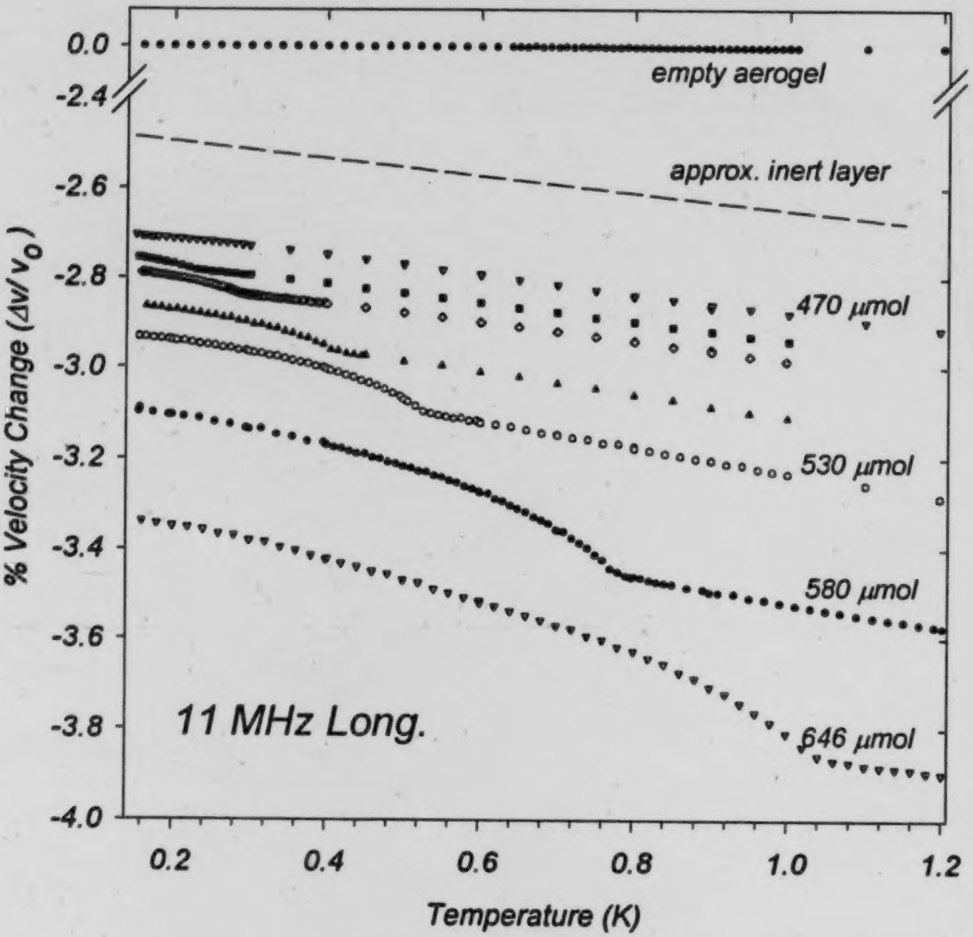

Figure 4.5.2. 11 MHz velocity for helium films adsorbed on aerogel. Empty aerogel, 470, 480, 490, 510, 530, 580, 646 μmol. The dashed line is the approximate location of the inert layer. Note the break in the vertical axis.

bound, non-superfluid layer, we treat it as part of the porous matrix and calculate the tortuosity with respect to the inert layer coverage. For thin film coverages only slightly greater than n_c, the film must conform closely to the aerogel strands and so it should be essentially the surface tortuosity, α_{2D}. Using eqn. (4.4.6), α_{2D} can be found by plotting the velocity change above the superfluid transition, $\Delta_1 = \Delta v/v_o$ $(T>T_\lambda)$, versus that at low temperature, $\Delta_2 = \Delta v/v_o$ $(T=0)$. If the tortuosity is constant, this should result in a linear equation with a slope equal to $(1-1/\alpha)$. Figure 4.5.3 shows such a plot for 11 MHz longitudinal (open symbols) and 6.5 MHz shear (filled symbols) modes for the thinnest films corresponding to transition temperatures below 1 K. The lowest transition temperature data is in the upper right corner; increasing the coverage moves the data points to the bottom left. The shear and the longitudinal data are in agreement with each other within the uncertainty of the measurements. From this low coverage data the surface tortuosity appears to be essentially constant. However, this procedure does not account for the temperature dependent TLS background and so the value calculated from Fig. 4.5.3 is an "apparent tortuosity", $\alpha_{app}=3.1\pm0.5$. The corrected value of the surface tortuosity will be discussed later in this section.

While the above method is valid for regions where the tortuosity is constant, we continue the above procedure to roughly half-filled pores which should result in an evolution in the tortuosity from α_{2D} towards α_{3D} and a deviation from linear behavior in a plot of Δ_2 versus Δ_1. Figure 4.5.4 is a plot of Δ_1, now measured at 2 K, versus $\Delta_2=\Delta v/v_o(T\sim0)$ and is limited to 6.5 MHz shear mode data. Data in the upper right corner correspond to the previous figure and a minimum transition temperature of ~250 mK; as helium is added the velocity decreases to the data point in the bottom left which corresponds to a transition temperature of approximately 2 K. The slope of the open circles is the (apparent) α_{2D} tortuosity. Since the square points deviate from the linear fit to the circles, thicker films evidently bring about a change in the tortuosity. The tortuosities for the entire range of fillings, n_c to fullpores, are now calculated.

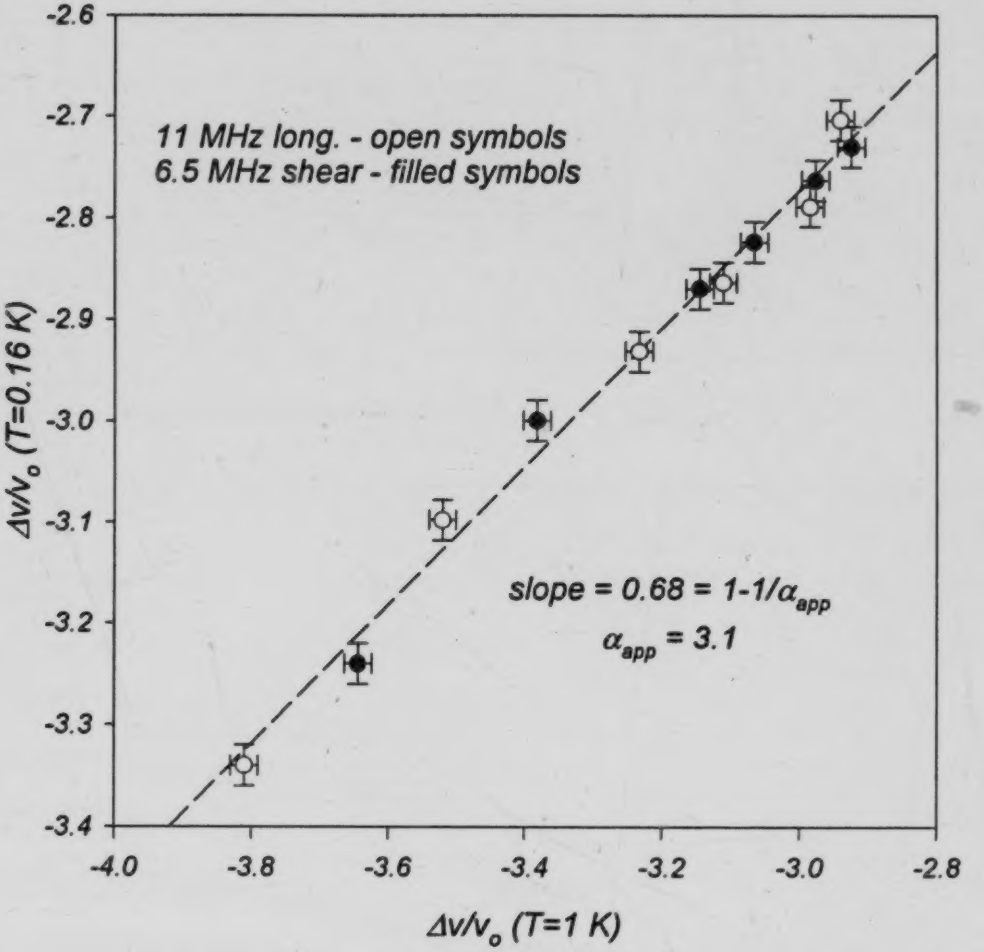

Figure 4.5.3. Plot of low temperature (T=0.16 K) velocity versus velocity above the lambda transition (T=1 K) for two frequencies: 11 MHz longitudinal and 6.5 MHz shear modes. The transition temperatures are below 1 K. The slope of the line is related to the tortuosity, which is found to be α_{app}=3.1.

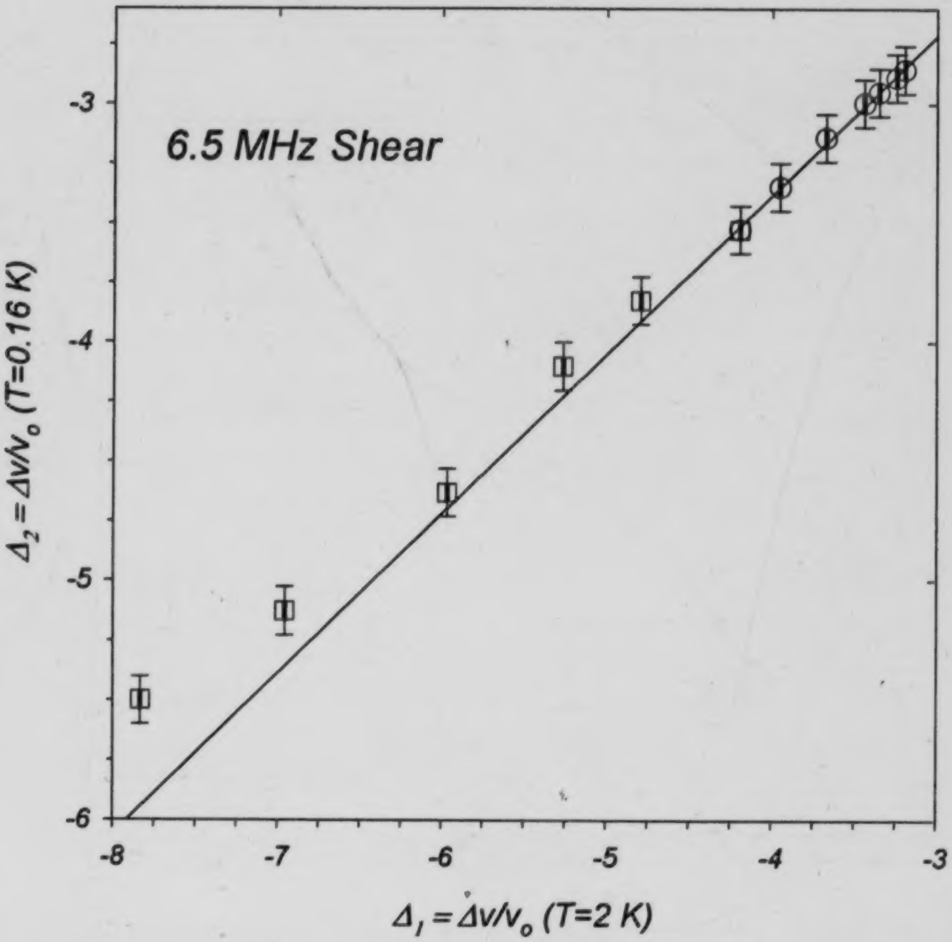

Figure 4.5.4. Veloctiy change at T=0.16 K versus velocity change at T=2 K displaying the decrease in slope with increasing helium adsorption. The amount of helium adsorbed ranges from 480-1100 μmol with the data points moving from the upper right to the lower left as helium is added. The transition temperatures range from 0.25 K to 1.8 K. As in Fig. 4.5.3, the slope is =(1-1/α_{app}).

Returning to the velocity data for the 6.5 MHz shear mode (Fig. 4.5.1), the tortuosity is calculated by measuring Δ_1 and Δ_2 as discussed. As shown in Fig. 4.4.1, Δ_1 is the change in $\Delta v/v_o$ with respect to the inert layer at T=1 K due to the adsorption of $n-n_c$ moles of helium; Δ_2 is the corresponding change in velocity at T=0.16 K due to the same adsorption. As n_c was not known in advance, the velocity for the inert layer was not directly measured and had to be determined by extrapolation of the $n>n_c$ data. While this extrapolation seems straightforward, the changing background can introduce large uncertainties in the final calculation of the tortuosity; data with $n\sim n_c$ are especially sensitive to small offsets in Δ_2. We now discuss the extrapolation of the inert layer.

The goal of the following procedure is to determine how (and if) the velocity above T_λ evolves with the addition of ^{4}He. We start by examining the slope of the velocity data in the temperature range $T_\lambda<T<1$ K, where the velocity variation is linear in temperature. In this temperature region, the velocity data corresponding to coverages from empty to 580 μmol are fit to linear equations, the slopes of which are then examined as a function of helium coverage (Fig. 4.5.5a). Figure 4.5.5a shows the slopes of the velocity background in the temperature range $T_\lambda<T<1$ K decrease linearly with helium coverage; as more helium is added the velocity above T_λ becomes more negative (steeper). Using the inert layer coverage n_c=427 μmol, the slope of the inert layer velocity is interpolated from Fig. 4.5.5a and found to be equal to -0.197 $(K)^{-1}$.

The next step is to determine the offset, or relative position, of the inert layer velocity by determining the change in the background ($T>T_\lambda$) at a constant temperature (T=0.8 K) as a function of adsorbed helium. This procedure is basically a mass sensitivity calibration, or a determination of the change in velocity at T=0.8 K due to mass loading of the aerogel. The velocity at 0.8 K is determined for a series of coverages (empty - 580 μmol) and is plotted again as a function of helium coverage (Fig. 4.5.5b). Figure 4.5.5b shows a linear relationship between the velocity change and the adsorption of helium from which, again using the inert layer coverage n_c, the relative offset of the inert layer

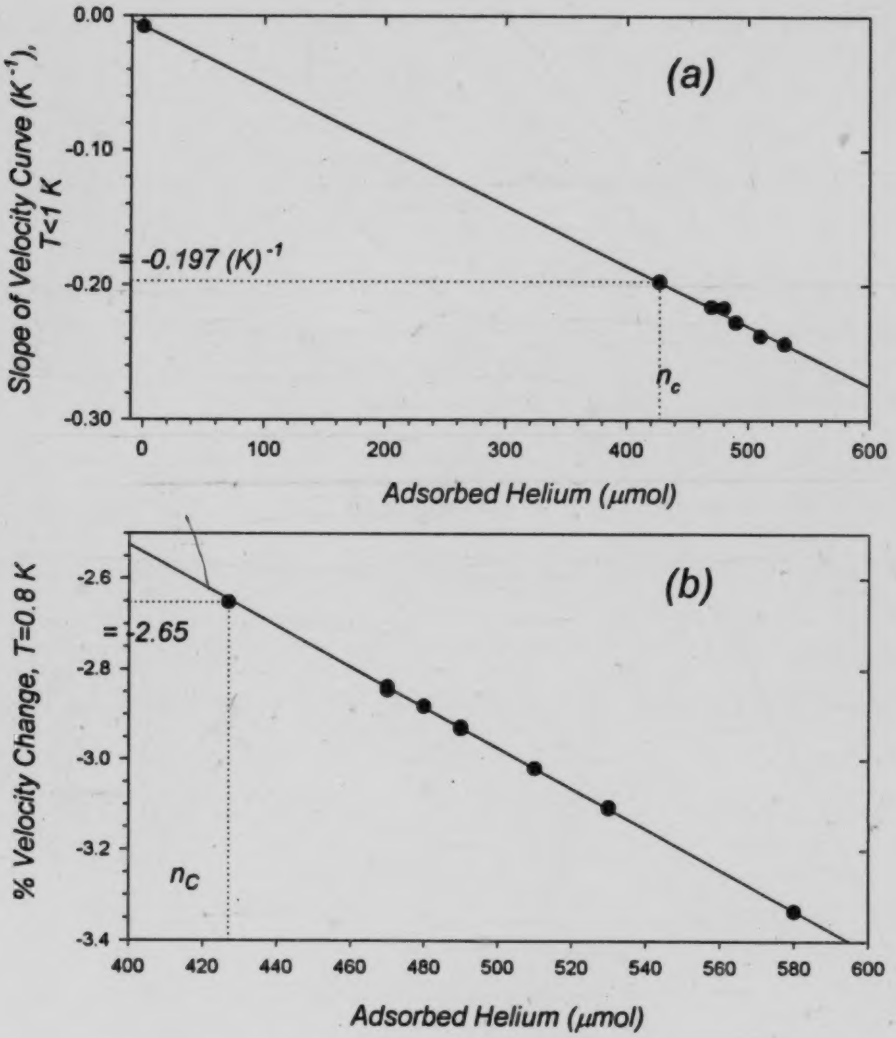

Figure 4.5.5a & b. Plots describing the determination of the inert layer velocity curve. (a) is the slope (d(Δv)/dT) of the inert layer velocity curve when T<1 K (b) is the change in the velocity at T=0.8 K as a function of adsorbed helium. Note the different scale on the graphs. All data is from 6.5 MHz shear mode.

can be extrapolated. A value of n_c=427 μmol returns a value of -2.65 for the inert layer velocity at T=0.8 K. From the slope and the offset at T=0.8 K a linear equation for the inert layer velocity was easily found:

$$\left.\frac{\Delta v}{v_o}\right|_{T<1K,\ n=n_c} = -0.197(K)^{-1}T - 2.49 \qquad (4.5.2)$$

which is shown in Fig. 4.5.1 as the connected filled circles. It is from this line that the values of Δ_1 and Δ_2 are measured.

The velocity change above T_λ that is plotted in Fig. 4.5.5b reflects the mass loading by the helium and can be used as a mass sensitivity calibration. From eqn. (4.4.3), the change in velocity should go as $\sim n_4 m_4/2m_a$. The slope in Fig. 4.5.5b provides a consistency check on the mass of the aerogel and gives m_a~44 mg, which is considerably larger than the measured 35 mg. This discrepancy is not surprising since the background is still evolving, presumably due to interaction of the aerogel TLS with the adsorbed helium; choosing a different temperature results in a different mass sensitivity. However, using the same calculation at a temperature (2 K) where the background is not evolving with adsorption, the mass of the bare aerogel (35 mg) is recovered.

While this change in mass sensitivity is small, it does introduce a correction into the above calculation of the surface tortuosity. Recall, the change in velocity at 0 K was plotted versus the change at 1 K under the assumption that the mass sensitivities at the two temperatures were equal, that is the addition of n moles of ^{4}He would change the background at 0 K by the same amount as at 1 K. As we see from the preceding analysis, due to an evolving background this is not the case. To correct for the disparity in mass sensitivities we note that instead of plotting Δ_1 and Δ_2 we should have plotted $m_{a1}\Delta_1$ and $m_{a2}\Delta_2$, where the masses are the "corrected" aerogel masses determined from plots similar to Fig. 4.5.5b, but for the respective temperatures. For example, Fig. 4.5.5b gives a "corrected" aerogel mass at T=0.8 K of 44 mg. Noting that the mass sensitivities are constant over a range of coverages, the tortuosity calculation is corrected by multiplying the slope of Fig. 4.5.3, 0.68, by m_{a2}/m_{a1} (=49mg/44mg) changing the surface tortuosity from 3.1 to 4.1±0.5.

One further correction was applied to the inert layer determination. It was mentioned earlier that the velocity curve of the 470 μmol film displayed a "roll off" at low temperatures. This deviation from linearity was corrected for at T=0.16 K in all calculations of Δ_2. If this correction is not made, the calculated values of Δ_2 and α are too large. For the lowest fillings (480 μmol), where there is not much superfluid to decouple in the first place, the calculated tortuosity is very sensitive to the precise value used for the inert layer velocity at T=0.16 K.

For films with transition temperatures above 1 K, Δ_1 had to be determined at 2 K instead of 1 K. In order to determine the velocity at 2 K, we first note that at this high temperature the background changes very little with coverage. Therefore, the background of the 470 μmol filling, which was measured to 2 K, was used to determine the velocity of the inert layer at 2 K by simply shifting the velocity axis so the two curves agreed at 1 K. A similar procedure was used for thicker films as well, allowing Δ_1 to be measured at 2 K for fillings up to 1100 μmol.

For thicker films, changes in the velocity became large and desorption occurred above T_λ so it was no longer practical to continue the above method of tortuosity calculation. Instead, the tortuosity was found by the background subtraction method. As outlined above, this requires a linear (in this case) extrapolation to T=0 K in order to determine the mass of helium that has decoupled. At higher temperatures the helium desorbs from the aerogel making background subtraction impossible. However, consistency was checked by comparing values of the tortuosity through an overlapping region of helium adsorption where both methods were employed.

A plot (Fig. 4.5.6) of α versus adsorbed helium shows the evolution from thin to thick films, and eventually α for completely filled aerogel. Adsorption of helium slightly above the inert layer, shown here by the vertical dotted line, shows large values of the tortuosity, $\alpha \sim 5$, but is within uncertainty equal to the surface tortuosity expected from Fig. 4.5.3, $\alpha \sim 4.1$. The tortuosity decreases with increased helium coverage, with considerable scatter in the data for coverages below 1000 μmol; however the different methods of calculation agree relatively well. For fillings greater than 1000 μmol the tortuosity decreases smoothly to its bulk value in aerogel of $\alpha = 1.5$.

The different symbols in Fig. 4.5.6 correspond to different methods of determining α. The dark circle represents the surface tortuosity $\alpha = 4.1$ as determined by Fig. 4.5.3; the grey filled circles represent calculations using the extrapolated inert layer and eqn. (4.4.6), with Δ_1 measured at 1 K; the open squares were also determined using the extrapolated inert layer, but with Δ_1 measured at 2 K; the triangles represent measurements of α by subtracting the background. Consistency between different measurements is displayed by the overlap of the data points.

With respect to the large values of the tortuosity when $n \sim n_c$, it should be recalled that for our measurement technique the measured tortuosity is larger than the real tortuosity of the system by a factor $\sim \rho_s/\rho_{He}$. While this factor may be important for fillings with $T_\lambda/2 < 0.16$ K (i.e. $\rho_s(T)/\rho_{He} \sim 1$ when $T < T_\lambda/2$) assuming 0.16 K is the 0 K approximation at which the velocity values were measured; for films with $T_\lambda \geq 0.3$K, ρ_n/ρ_4 should be close to zero. We also note for the lowest fillings the tortuosity is very sensitive to the exact value of the inert layer velocity at 0.16 K. However, the effect of this inert layer offset decreases as more helium decouples, so the tortuosity values for fillings above ~510 μmol are only slightly affected. Therefore, we take α at n_c to be equal to the value given by the slope of Fig. 4.5.4, corrected for the mass sensitivity, $\alpha = 4.1$. This is indicated by the filled circle on the dotted vertical line.

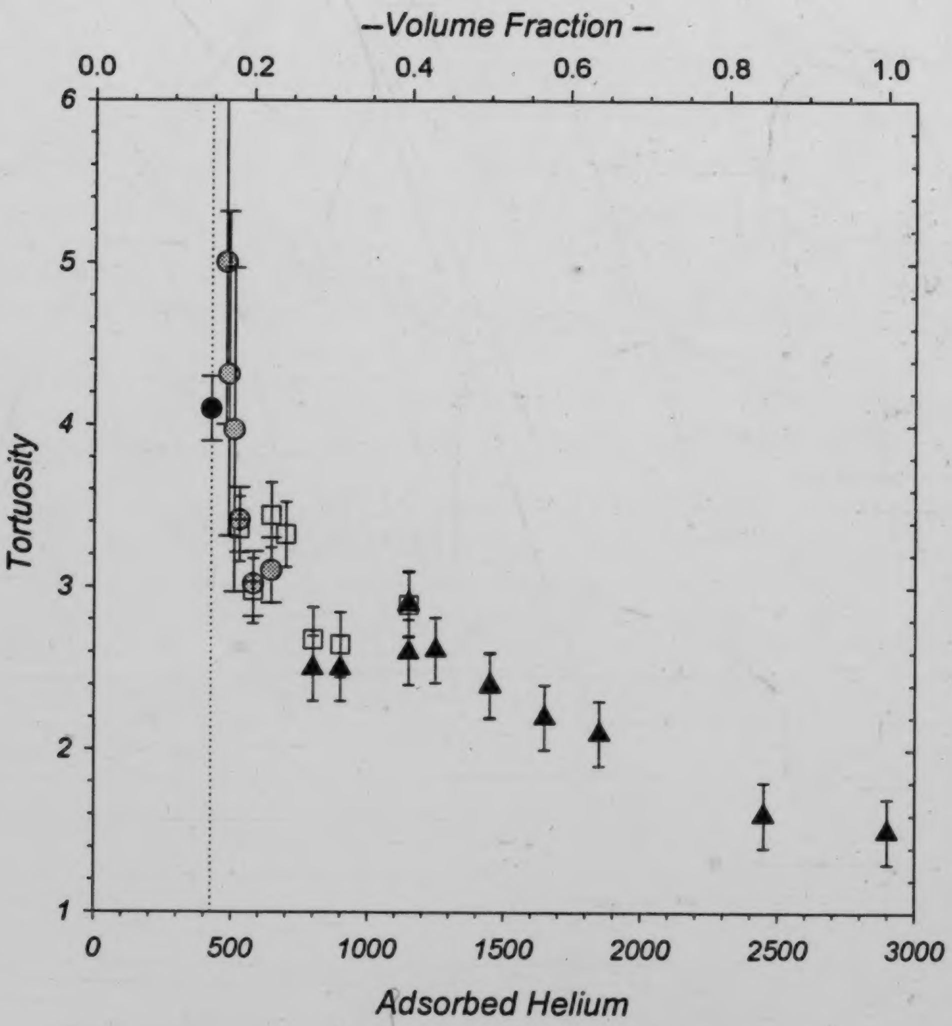

Figure 4.5.6. The tortuosity, α, as a function of helium adsorption. The vertical dotted line represents the inert layer adsorption, 427 μmol. The filled circle at 427 μmol is the surface tortuosity. The different symbols indicate different methods of calculation (see text). The upper scale represents the fraction of the pore volume the helium occupies.

Figure 4.5.6 also shows, on the upper horizontal scale, the volume fraction *f*, of aerogel occupied by the helium. The particular aerogel sample used here has a pore volume of ~0.08cc and therefore requires ~2900 µmol of ^{4}He (v_4 ~27.6 below 1 K) to fill. The introduction of *f* allows a comparison with the mixture data to be presented in the following chapter. We would like to compare mixtures with the "equivalent concentration" ^{4}He films, implying the two systems have the same amount of ^{4}He contained in the aerogel. The equivalent concentration is calculated by determining the amount of ^{3}He required to fill the pore space not occupied by the ^{4}He film assuming (bulk density values). The volume fraction is related to the ^{3}He concentration, $X = n_3/(n_3+n_4)$, via $X=(1-f)V_a/((n_4-n_c)v_3 +(1-f)V_a)$, where V_a is the volume of the aerogel.

4.6. Conclusions

Measurements of the ultrasonic velocity in an 87% porosity aerogel with adsorbed ^{4}He films were used to find the inert layer coverage, $\sigma_c = 30.7$ µmol/m^2, and to determine the tortuosity as a function of ^{4}He filling. More pertinent to the next chapter is the actual amount of ^{4}He, $n_c = 427$ µmol, needed to achieve superfluidity at T=0 K in this particular sample. The tortuosity decreased roughly linearly with increasing ^{4}He filling, from $\alpha=4.1\pm0.5$ for thin films to $\alpha=1.5$ when the aerogel pores were saturated with ^{4}He. Although barely resolvable from the noise, attenuation peaks, which grow with ^{4}He filling, were detected at the transition.

Chapter 5

Helium Mixtures in Aerogel

Two distinct phase transitions occur in bulk helium mixtures. The lambda transition is a continuous transition to a superfluid state. At temperatures below 0.87 K a solubility gap is found; mixtures phase separate into a less dense ^{3}He rich phase atop a ^{4}He rich phase. At T=0 K there is a finite solubility of ^{3}He in ^{4}He and the denser phase contains ~6% ^{3}He; however, the ^{3}He rich phase is pure at 0 K [38]. T_λ is 2.17 K in pure ^{4}He but decreases as ^{3}He is added. The resulting lambda line meets the phase separation curve at a *tricritical point* (X_{tr}=0.67, T_{tr}=0.87 K) which replaces the normal critical point found at the apex of the phase separation curve. Pressure also affects the phase diagram and generally decreases the width of the phase separation and the temperatures of both the superfluid and phase separation transitions. In this work we are only concerned with mixtures at saturated vapor pressure.

As will be discussed, ultrasonic velocity and attenuation measurements are sensitive to both phase separation and the lambda transition [66]. This chapter describes how these transitions affect the ultrasonic measurements of velocity and attenuation. As discussed in Chapter 3 the data were taken by first determining the ^{4}He inert layer, then filling the remaining pore space with ^{3}He. Lower ^{3}He concentrations were obtained by subsequently replacing some of the ^{3}He with ^{4}He. For pedagogical reasons, the data in this chapter are presented in reverse order, starting with the pure ^{4}He data and proceeding to high X. Comparisons are also made to the Penn State group's torsional oscillator and heat capacity measurement in 87% porous aerogel. A discussion and summary of the experimental measurements closes the chapter.

5.1. The Superfluid Transition in Aerogel

We start with saturation of the aerogel pores by pure ^{4}He. Figure 5.1.1 is a plot of the velocity and attenuation measurements for a 9 MHz shear wave propagating through 87% aerogel filled with ^{4}He. The aerogel sample was from the same batch as that used for the films and mixtures but was not encased in epoxy. The slight velocity increase above 2.2 K is due to thermal expansion of helium in the aerogel. The lambda temperature is slightly depressed due to confinement in the aerogel: $T_\lambda = 2.161$ K. Below T_λ decoupling of the superfluid from the aerogel matrix causes the velocity to sharply increase.

The increase in velocity at T_λ is accompanied by a critical attenuation peak. The critical attenuation peak in Fig. 5.1.1 seems sharp, but is superimposed on a Biot (viscous) background attenuation which has a kink at T_λ. The Biot attenuation in the high and low frequency regimes has been discussed in Chapter 2 and has been calculated here using the viscosity and (normal) density and is shown in Fig. 5.1.1 as the solid lines.

The inset in Fig. 5.1.1 displays the velocity and attenuation close to T_λ. The critical attenuation peak has a half width of about 5 mK and the velocity shows a few milli-Kelvin rounding above the attenuation maximum. These features could be either related to inhomogeneities in the aerogel sample or to the high frequency of ultrasonic measurements.

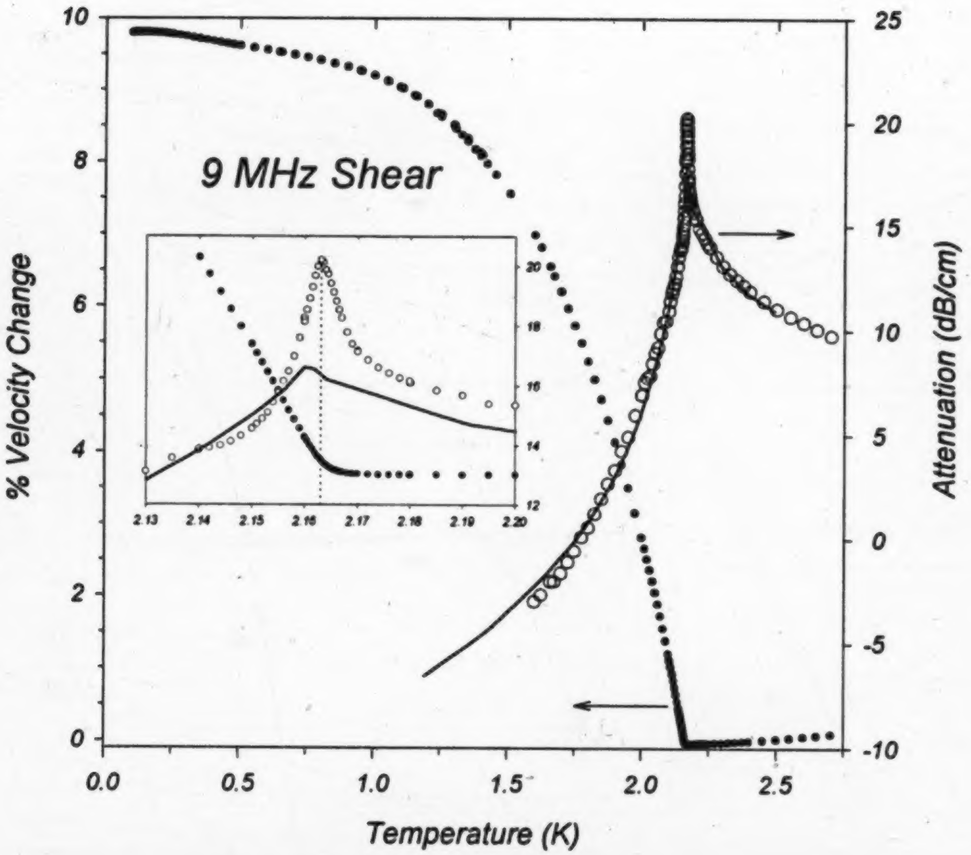

Figure 5.1.1. The superfluid transition in aerogel saturated with pure ^{4}He. The filled symbols represent the velocity change and the open symbols the attenuation change. The solid lines indicate the Biot attenuation.

Identifying T_λ from the attenuation maximum, the superfluid critical exponent and critical amplitude can be determined from the velocity data. Figure 5.1.2 shows the velocity change versus the reduced temperature on a log-log plot. The slope gives the superfluid density critical exponent, $\zeta \sim 0.89$, somewhat larger than the value 0.813 found in less dense (91% and 94%) aerogel [17, 18]. The critical amplitude, ρ_{so}, is found from the intercept of the linear extrapolation in Fig. 5.1.2, $A_o \sim 0.28$, and a rearrangement of eqn. (4.4.3)

$$\rho_{so} = \frac{\rho_o}{(1-1/\alpha)}\left(1-\frac{1}{(1+A_o)^2}\right) \qquad (5.2.1)$$

where $\rho_o = (\rho_a + n_c m_4/V_a) \approx 0.37$ g/cc and $\alpha \sim 1.5$. The result $\rho_{so} = 0.43$ g/cc is comparable to that found in 94% (0.41 g/cc) and 91% (0.37 g/cc) aerogel [18] and in bulk helium (0.35 g/cc).

5.2. Mixtures in Aerogel

We now proceed to mixtures in aerogel. Figure 5.2.1 shows changes in the 11 MHz longitudinal velocity and attenuation data for a mixture with $X \sim 0.05$. Considering first the velocity, the transition temperature in the mixture is suppressed, $T_\lambda \sim 1.97$ K, compared to 2.163 in the pure ^{4}He filled aerogel. There is no indication of phase separation for this mixture. The attenuation is also changed by the addition of ^{3}He. The Biot attenuation still plays a large part in the background and the peak in attenuation at T_λ is slightly smaller in mixture. The undulations in the attenuation below T_λ are an experimental artifact due to an amplitude dependence in the phase of the ultrasonic signal. No attempt has been made to correct for this phase dependence.

Figure 5.2.2 gives an overview of 11 MHz longitudinal velocity measurements for ^{3}He concentrations $X=0.12$ (top) to 0.69 (bottom). The velocity is measured in terms of

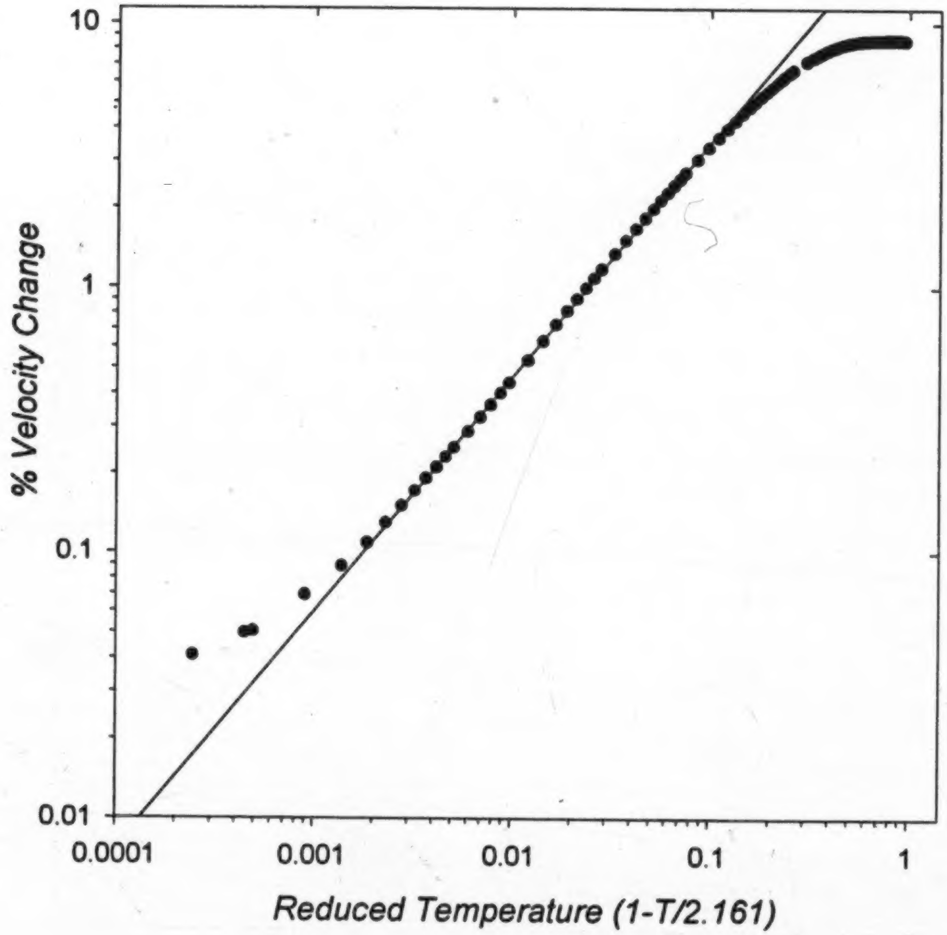

Figure 5.1.2. A log-log plot of the velocity below the superfluid transition versus the reduced temperature in 87% aerogel. The slope of the line is the critical exponent, 0.89; the critical amplitude is related to the intercept, A_o=0.28.

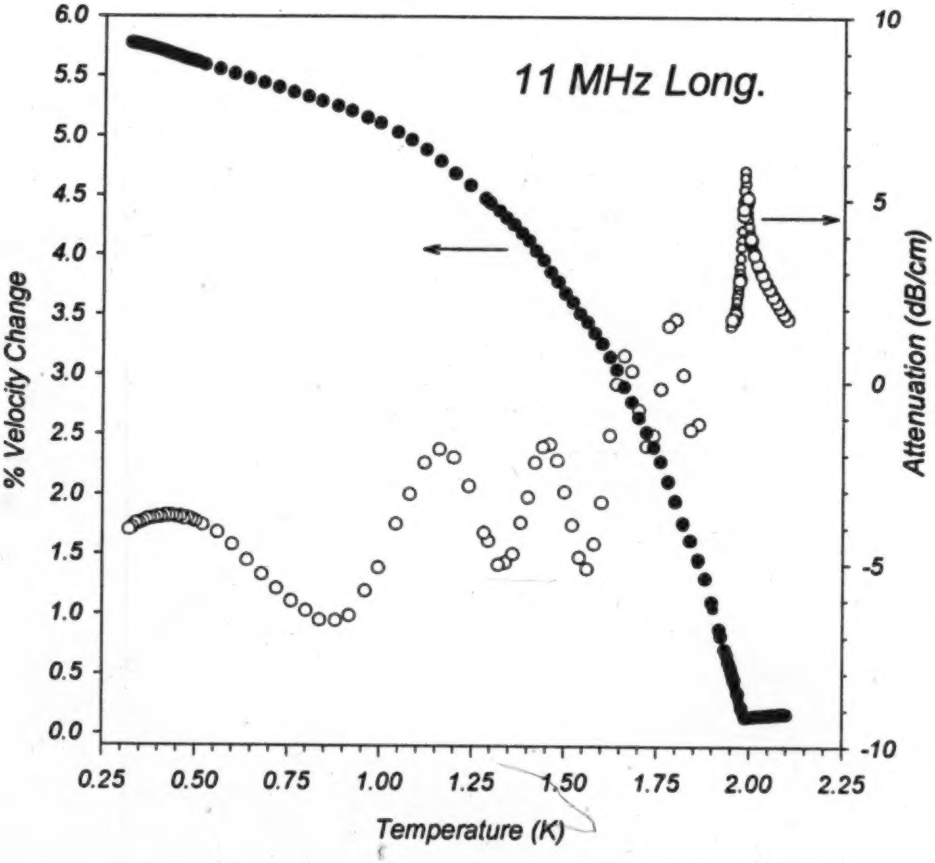

Figure 5.2.1. 11 MHz longitudinal velocity (filled symbols) and attenuation (open symbols) for a mixture of concentration X~0.08.

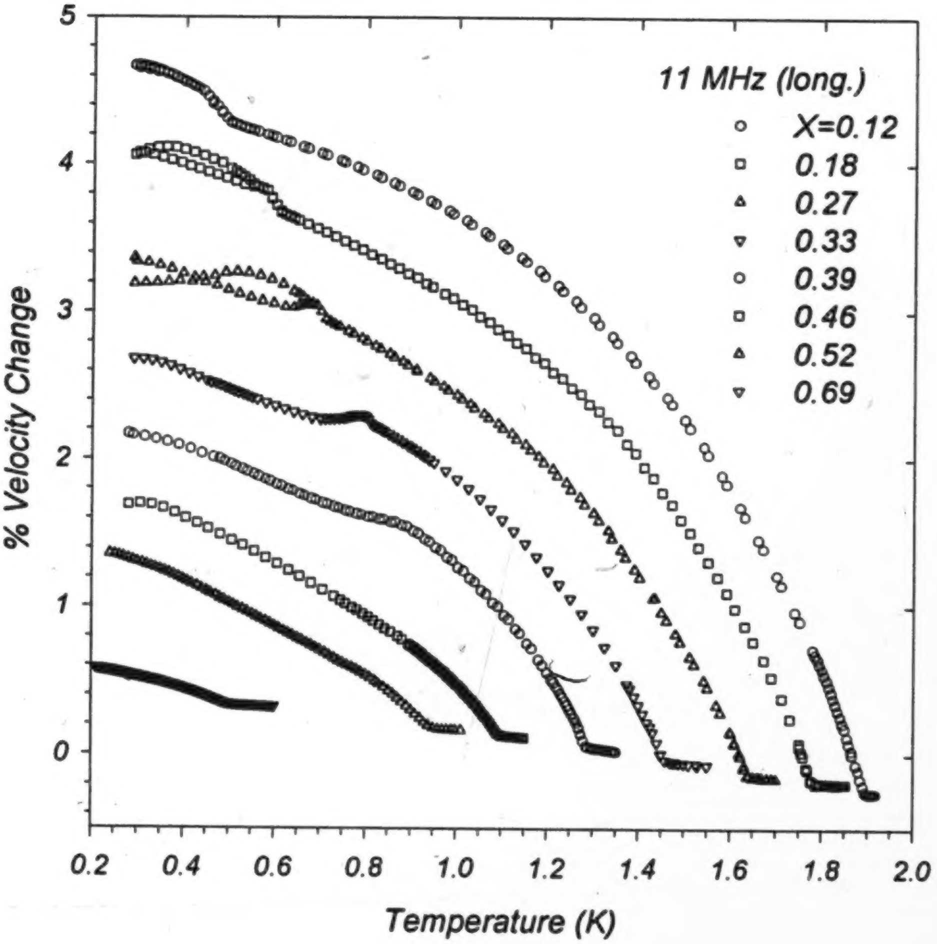

Figure 5.2.2. 11 MHz longitudinal velocity data for mixtures ranging from X=0.12 to 0.69. The onset of hysteresis is visible for the upper 3 curves (0.12 - 0.27). The phase separation signature vanishes as X approaches 0.4.

percent change and the curves have been shifted vertically for clarity (to compensate for the offsets due to mass loading). Fig. 5.2.2 shows a number of regimes which will be separately discussed below. Starting with the uppermost (lowest ^{3}He concentration X=0.12) curve, the lambda transition is further suppressed for increasing X. Unlike the pure ^{4}He (Fig. 5.1.1) and X=0.08 (Fig. 5.2.1) cases, the top curve has a second feature near 0.5 K which is associated with phase separation. At higher ^{3}He concentrations, e.g. X=0.27, phase separation results in hysteresis in the velocity on warming and cooling. However, when X increases further, X=0.39, the distinct signature of phase separation becomes "washed out". For still higher ^{3}He concentrations only a single lambda-like transition remains.

In order to study the transitions in more detail, we consider three concentration regions: first, concentrations where the phase separation marker is unambiguous (X<0.3); second, the region where the onset of hysteresis disappears (X~0.3); third, the region where the last indications in the velocity curves of phase separation disappear (X>0.4).

The first regime of interest is when the ^{3}He concentration is less than 30%, (Fig. 5.2.3). At low enough concentrations (X~0.06) only the lambda transition is detected, presumably because either the phase separation temperature is below the base temperature of the dilution fridge (300 mK for these mixtures) or, as in bulk mixtures, the dilute solution is miscible at all temperatures. Upon adding more ^{3}He, the slope of the velocity curve suddenly increases again at some temperature $T_s<T_\lambda$. In contrast to the lambda transition at high temperatures, the increase in slope at T_s persists over a small temperature range, ΔT. The result is a "jump" or "ramp" in the velocity. Below the jump, the velocity appears to vary much as it did above T_s, where it was governed by superfluid decoupling. Further addition of ^{3}He increases the phase separation temperature T_s but decreases both the size of the velocity jump and the temperature range ΔT over which it occurs. The bottom two curves (X=0.18, 0.27) also display hysteresis loops, which begin at a temperature slightly below T_s.

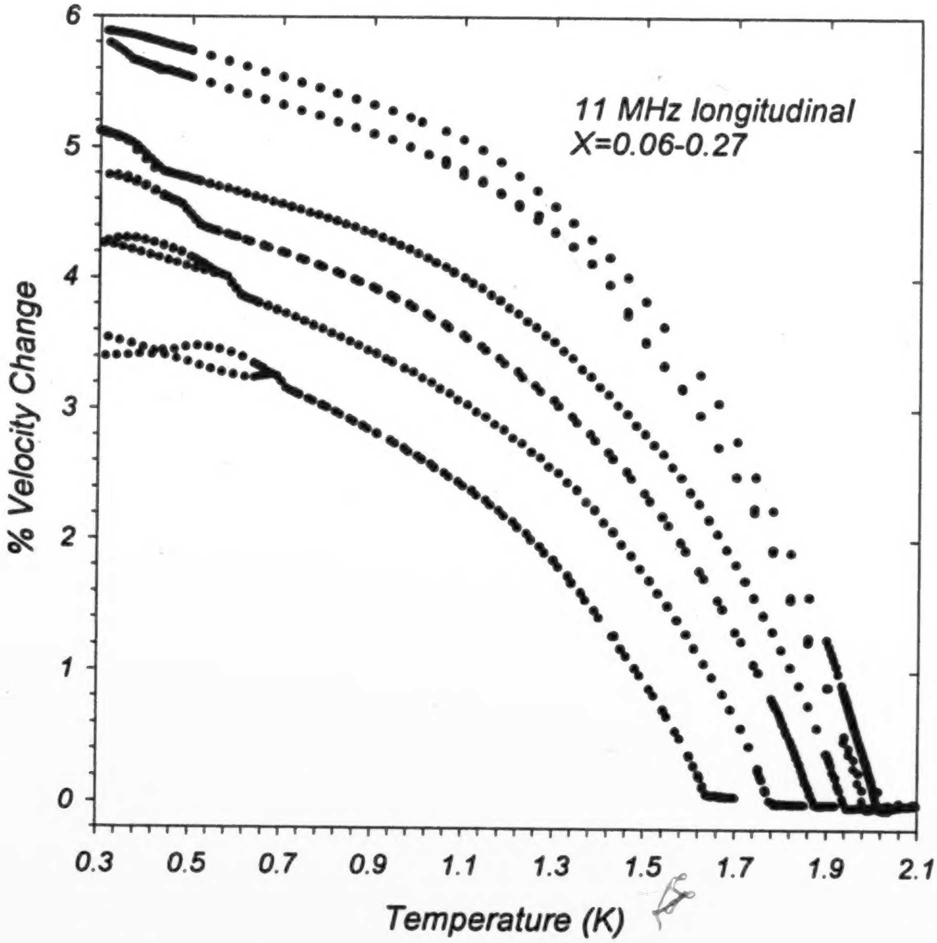

Figure 5.2.3. Velocity data for mixtures, from top to bottom, X=0.06-0.27. The data corresponds to 11 MHz longitudinal mode. The hysteresis disappears as X decreases further, however, the jump in velocity slighlty above T_S continues to increase.

The next concentration regime is X=0.27-0.4 where the jump and hysteresis due to phase separation give way to a broad dip in the velocity. Figure 5.2.4 displays the range of concentrations 0.27 (top curve) to 0.39 (bottom curve). T_λ continues to decrease and T_s increases with increasing ^{3}He concentration. The hysteresis loops are open at low temperatures because the sample was first cooled rapidly to the base temperature, then data were collected during slow warming and cooling. In runs where data were collected on cooling, then warming, the hysteresis loops were closed at low temperatures. Hysteresis was independent of the cooling/warming rate.

The magnitude and width of the velocity jump below T_s decrease with X until, at X=0.39, neither a distinct kink nor hysteresis remain. Phase separation appears as a broad dip in velocity beginning at ~0.9 K.

Figure 5.2.5 shows the range of concentrations over which the last obvious signature of phase separation disappears. The concentration ranges from X=0.4 (top curve) to 0.52 (bottom curve). For concentrations less than X=0.44, there is an inflection point in the velocity curve below which the second derivative with respect to temperature becomes positive. For the four lowest concentrations the approximate location of the inflection point is marked with an arrow. However, for concentrations X>0.44 (the lower curves, shown as open circles) the velocity is smooth, without a kink or inflection point. This "washing out" of the signature of phase separation is not surprising if the mixtures are close to a critical or tricritical point where there is no density difference between the two phases. Since the ultrasonic velocity is sensitive primarily to changes in density, the experimental phase separation signature should disappear at the critical point.

The lambda transition remains well defined and evolves smoothly to lower temperatures as X increases, even after the phase separation cannot be seen. This continues even beyond the bulk tricritical concentration. Figure 5.2.6 is a detailed temperature scan of the ultrasonic attenuation (open symbols) and velocity (filled

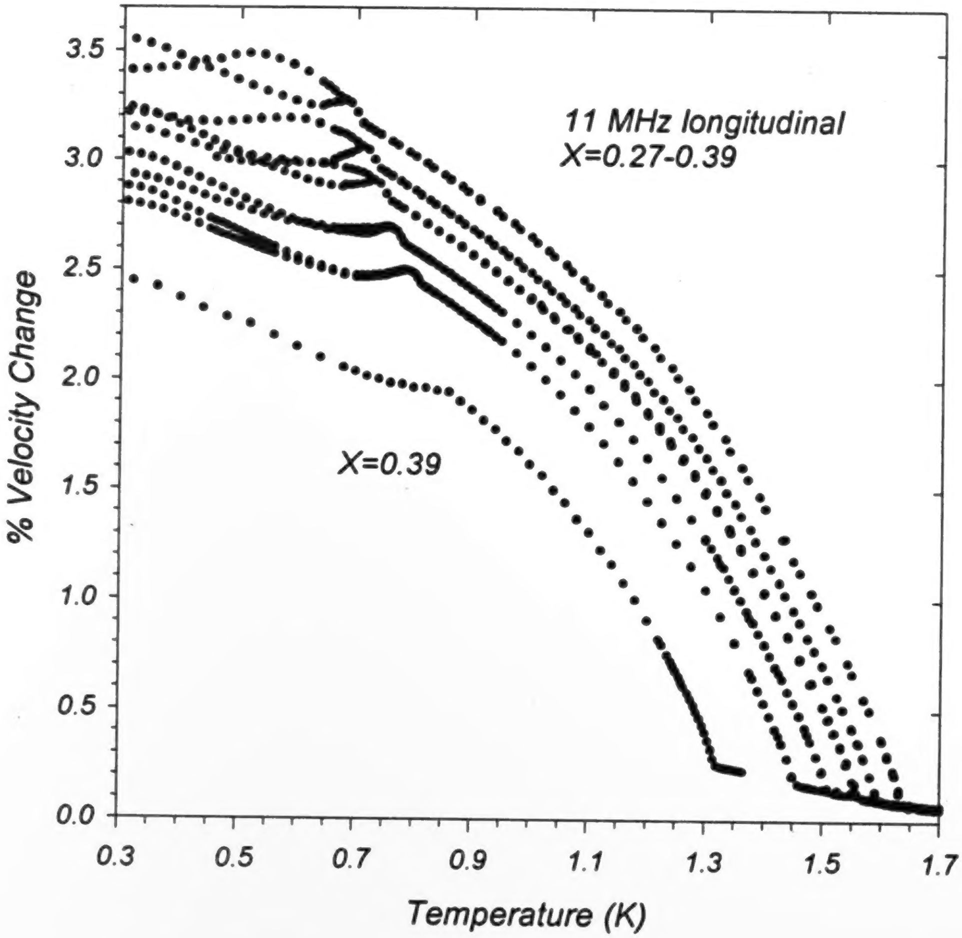

Figure 5.2.4. Velocity data for mixtures, from top to bottom, X=0.27-0.39. The data corresponds to an 11 MHz longitudinal mode. The onset of hysteresis is clearly visible in all curves except X=0.39 and is preceded on cooling by a slight increase in the velocity.

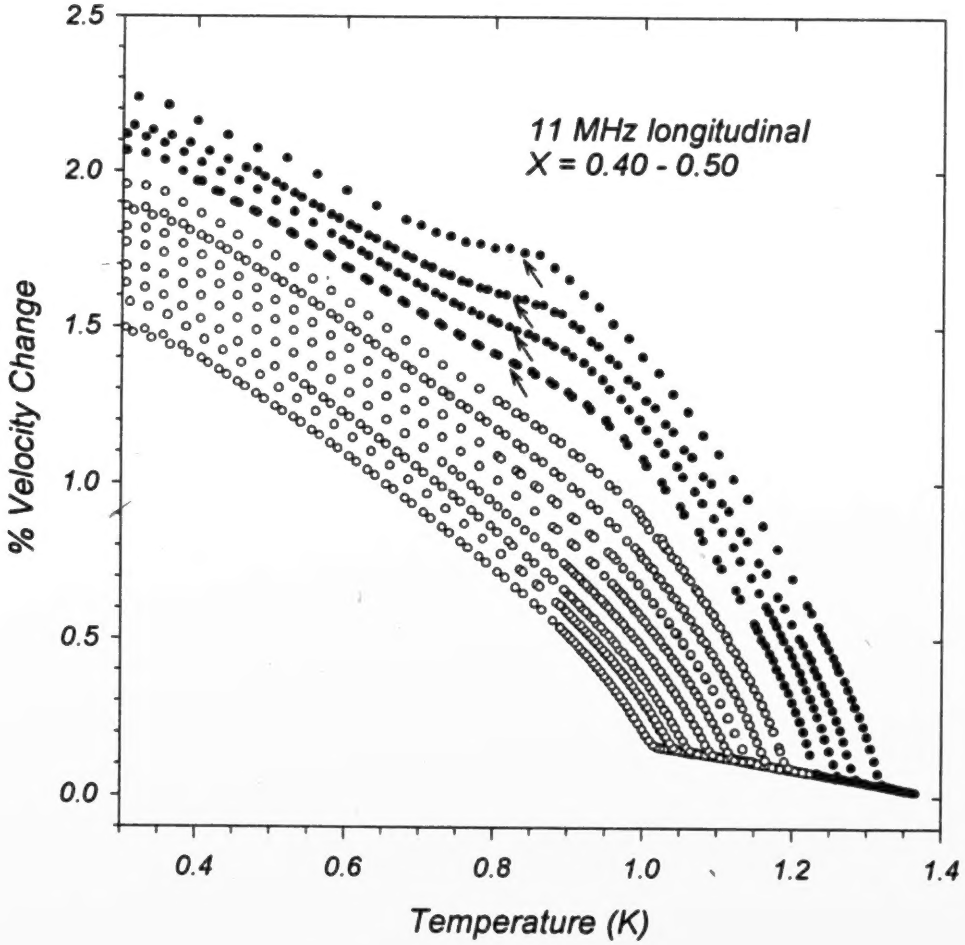

Figure 5.2.5. Velocity data for mixtures, from top to bottom, X=0.4-0.5. The data corresponds to an 11 MHz longitudinal mode. Arrows mark where the inflection point occurs, see text.

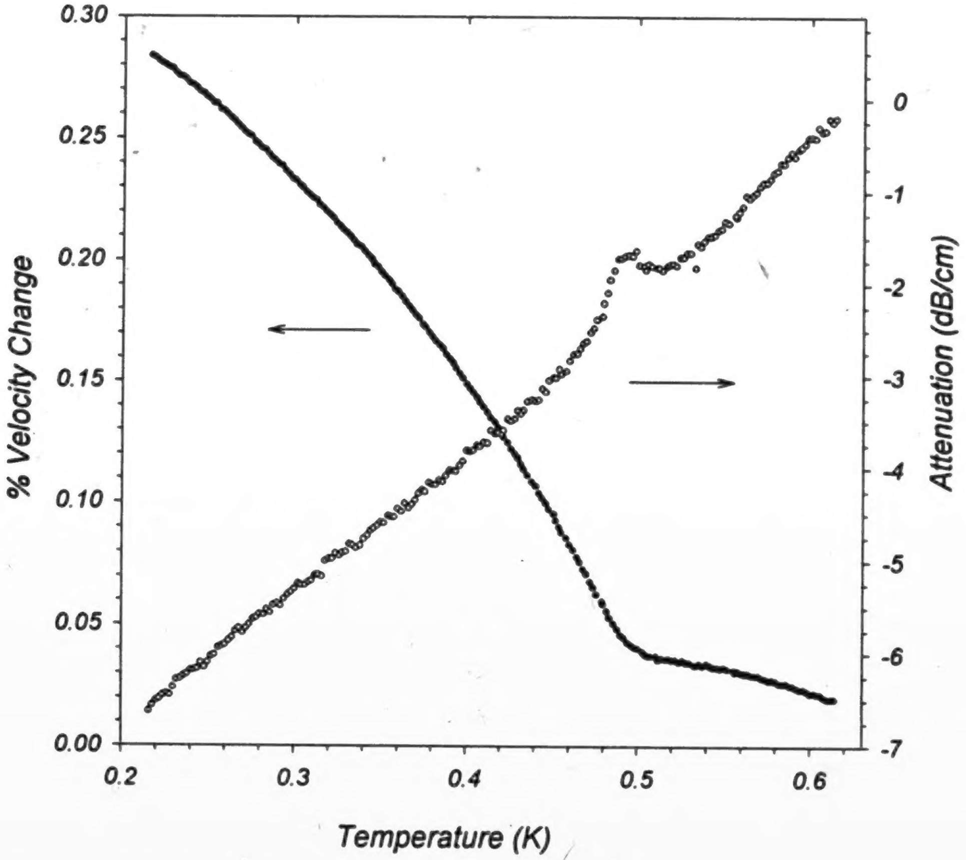

Figure 5.2.6. Changes in ultrasonic velocity (filled) and attenuation (open) of a helium mixture, X=0.69, 11 MHz longitudinal mode. As with pure helium saturating the pores, the velocity increases below T_λ, and there is a critical attenuation peak at T_λ.

symbols) of a 6.5 MHz shear mode for a mixture with X=0.69. The sudden velocity increase at 0.5 K and the accompanying attenuation peak resemble the superfluid transition seen in pure ^{4}He films in aerogel and in lower ^{3}He concentration mixtures (Figs. 5.1.1 and 5.2.1). Other than this lambda-like transition at T=0.5 K there is no indication of any other transition, either above or below T_λ.

The implications of Fig. 5.2.6 are the following. Bulk helium mixtures with ^{3}He concentrations greater than X_{tr} are not superfluid, but superfluid ordering drives a first order phase separation at T_s. In a bulk mixture with T_s=0.5 K and $X>X_{tr}$, phase separation occurs by the nucleation and growth of a superfluid phase minority phase with ^{3}He concentration X~0.2. At 0.5 K, this phase is far from its critical region (T_λ~1.9 K) and so we therefore do not expect to see critical behavior in the velocity or attenuation, in contrast to the behavior seen in Fig. 5.2.6. Instead, for mixtures above the tricritical concentration X_{tr}, phase separation would produce phases with quite different densities and a well-defined interface between them. We would then expect similar behavior to that seen in phase separation in the low X mixtures, i.e. hysteresis and jumps in the velocity. In fact, Fig. 5.2.6 shows no indications of hysteresis, in either the velocity or attenuation, that might indicate a first order phase transition. At X=0.69 the transition appears to be a *continuous transition* from a normal to a superfluid state at a concentration where a *first order transition occurs in bulk mixtures*. In fact, Fig. 5.2.6 is very similar to the superfluid transition at ~0.4 K in a pure ^{4}He film seen in Fig. 4.2.3.

General trends in the ultrasonic attenuation data are now presented. All data correspond to changes in 11 MHz longitudinal attenuation data are shown in Fig. 5.2.7. The mixtures span $0.12 \leq X \leq 0.69$ and have been shifted vertically for clarity. An attenuation peak appears at the lambda transition in all mixtures; T_λ decreases as X increases. Although it is difficult to see from Fig. 5.2.7 the peaks become sharper and larger as more ^{4}He is added. The attenuation oscillations seen at temperatures below T_λ in the mixtures with higher concentrations of ^{4}He (X = 0.12, 0.27) are the same artifacts

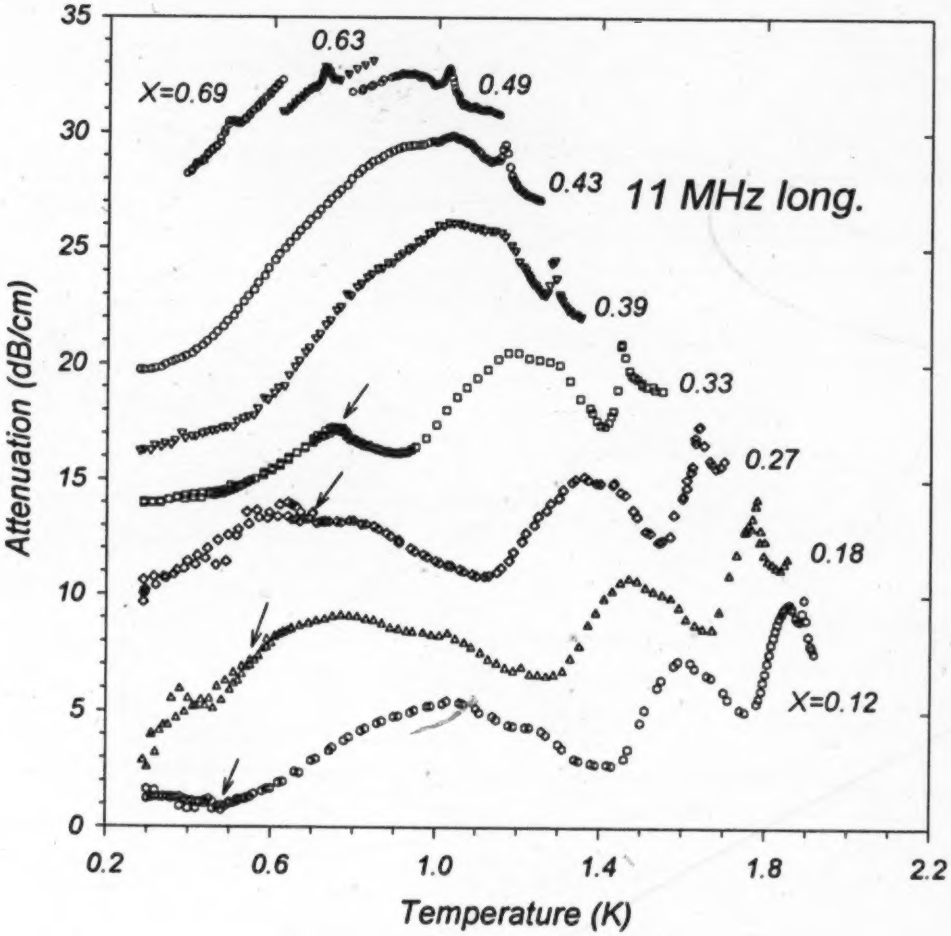

Figure 5.2.7. General trends in the ultrasonic attenuation for X<0.7. The peaks at high temperature correspond to the sharp rise in the ultrasonic velocity and the onset of superfluidity, while the arrows mark the phase separation transition. The undulations between the two transitions are artifacts of the measurement system.

seen in Fig. 5.2.1. They result from a slight dependence of the amplitude on the phase of the signal; a higher concentration of ^{4}He results in larger changes, and hence more oscillations. For the mixture $X=0.33$, an arrow marks a cusp in the attenuation which is associated with phase separation. At lower concentrations, phase separation is accompanied by hysteresis, marked by arrows in Fig. 5.2.7. There is no evidence of attenuation due to scattering, so we infer the domain sizes in the phase separated mixtures are much smaller than the acoustic wavelength (10's μm).

Figure 5.2.8 displays 9 MHz longitudinal attenuation and velocity data in the region where phase separation begins. The open circles are cooling, the filled circles are warming, and the mixture concentration is 0.26. Note the velocity axis is on the left, the change in attenuation is on the right, and the temperature span is 140 mK. At temperatures above 0.69 K there is no difference between warming and cooling in either the velocity or attenuation data; below $T=0.69$ K, the velocity and attenuation are larger on cooling than warming. However, the onset of phase separation occurs at slightly higher temperature than the hysteresis, first appearing as a kink in the velocity and attenuation at $T_s=0.71$ K. The velocity "jump" associated with phase separation in this mixture occurs between $T_s=0.71$ K and the onset of hysteresis at 0.69 K, a temperature span of $\Delta T \approx 20$ mK. As pointed out previously, this temperature span grows with decreasing ^{3}He concentration.

5.3. Helium Mixture Phase Diagram in 87% Aerogel

From measurements of the sound velocity for about 60 mixtures the T-X phase diagram can be inferred; Fig. 5.3.1 is the result. Open circles are determined from transitions corresponding to the onset of superfluidity (sharp increase in velocity and attenuation peak). The lambda transitions for pure ^{4}He and $X=0.05$ are at 2.16 K and 2.01 K. For concentrations $X>0.05$ two transitions are found. The high temperature transition is identified with the onset of superfluidity and T_λ is found to decrease with

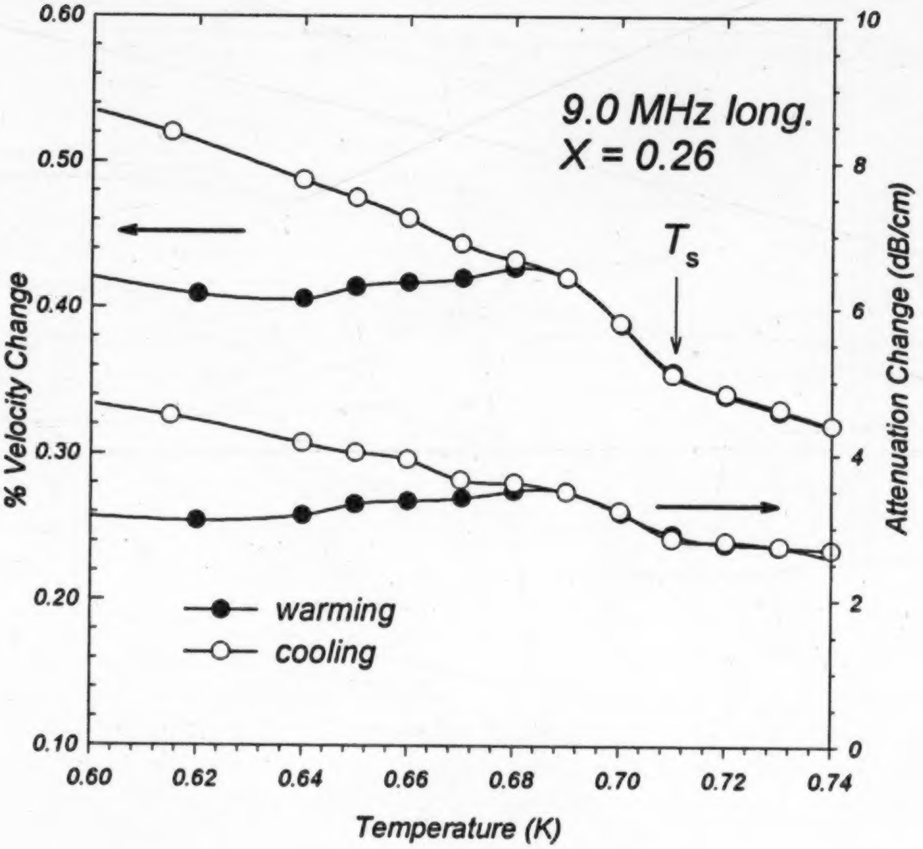

Figure 5.2.8. 9 MHz longitudinal velocity and attenuation displaying hysteretic behavior below T_s.

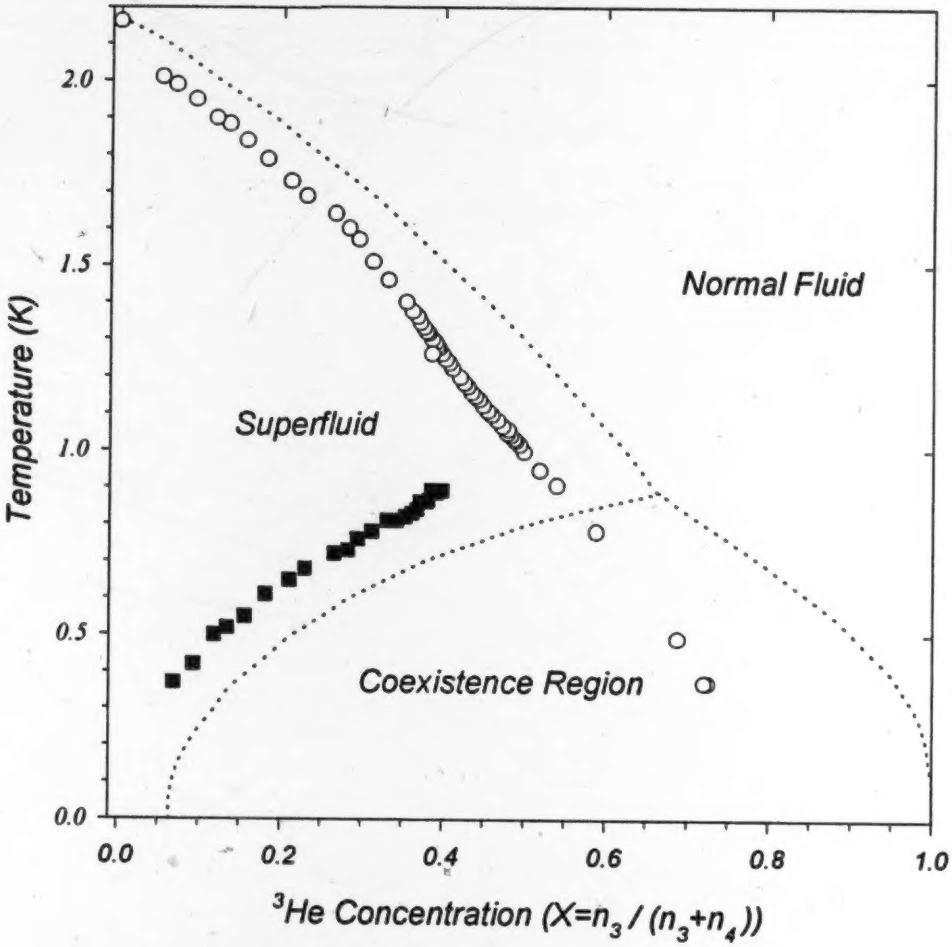

Figure 5.3.1. Phase diagram of helium mixtures contained in aerogel. Open circles indicate the superfluid transition as determined by the increase in velocity and the peak in attenuation. Filled squares are the locations of the phase separation transition.

increasing X. Phase separation is represented by filled squares in Fig. 5.3.1. T_s is found to increase with increasing X, up to X~0.4.

For mixtures with 0.4<X<0.8 there is a single transition which is identified as the onset of superfluidity and is marked with the open circles in Fig. 5.3.1. This is one of the main results of this thesis: *Helium mixtures in aerogel display a continuous superfluid transition for dilute amounts of ^{4}He in ^{3}He*. This behavior is in contrast to bulk mixtures where, for $X>X_{tr}$, a first order phase separation transition preempts the superfluid transition and bulk superfluidity is limited to concentrations X<0.667.

Above X~0.8, there is no discernable transition, presumably because a minimum amount of ^{4}He is required to form the tightly bound ^{4}He inert layer on the aerogel surface (^{4}He is expected to be preferentially bound to the aerogel surface as its zero point motion is lower than that of ^{3}He [50]).

One modification can be made to the above phase diagram. A ^{4}He inert layer resides on the surface of the aerogel [50] (427 μmol by extrapolating the coverage required for a superfluid transition in ^{4}He films, see Section 4.3). The phase diagram can be modified by assuming this inert layer plays no role in the mixture dynamics and is independent of the concentration. The corrected ^{3}He concentration, X^*, is

$$X^* = \frac{n_3}{n_3+n_4-427} \qquad (5.3.1)$$

where n_i (i=3,4) is the molar amount of an isotope in μmol. Equation (5.3.1) produces higher ^{3}He concentrations and provides a more appropriate comparison to the bulk phase diagram (dotted lines in Fig. 5.3.2). The corrected phase diagram is shown in Fig. 5.3.2. The lambda line now corresponds more closely to the bulk transition. The phase separation line below $X^*=0.5$ (filled squares) also lies closer to that of bulk mixtures.

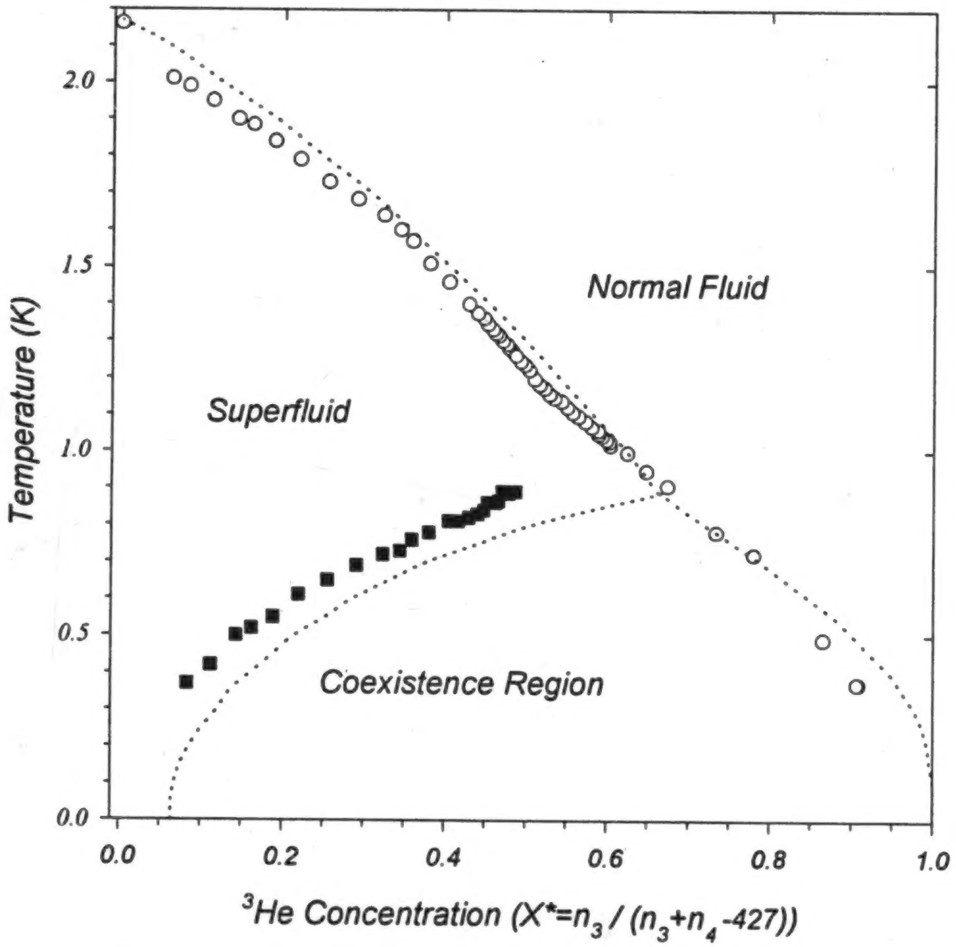

Figure 5.3.2. Corrected phase diagram of helium mixtures in aerogel. Open circles are the superfluid transition, filled squares are the phase separation. The dotted line represents the bulk phase diagram.

As these were in fact the last curves obtained, the uncertainty in the concentration is notably larger than in the previous mixtures. To get an estimate of this effect note for the 6% solution the transition temperature is ~2.03 K whereas aerogel saturated with ^{4}He displays $T_\lambda = 2.163$ K. Comparing with bulk mixtures, a transition temperature of 2.03 K is more consistent with a solution of ~11%. In fact, these curves are derived from a new mixture at X*~0.35 and there seems to be a systematic shift in the data: there is apparently more ^{3}He than was recorded.

Since we would like to compare our results to those of the bulk phase diagram *all further references to the concentration are to X**, which is the corrected ^{3}He concentration using the inert layer measured for pure ^{4}He films.

The apparent kink in the lambda line at X*~0.5 and T=1.15 K is clearer in Fig. 5.3.2. It coincides with the disappearance of the last signature of phase separation, namely the "dips" in the velocity. Figure 5.3.3 is a blow up of the concentration region X*=0.43 to 0.65. While there is some scatter in the data, a kink is seen at X*=0.53, T=1.15 K. The lines which intersect at X*=0.53 show that the transition temperatures vary linearly with concentration both above and below the kink.

In bulk mixtures the phase separation and lambda lines meet linearly at a tricritical point (X=0.67, T=0.87 K). In the aerogel phase diagram presented in Fig. 5.3.1, it is not clear where (or whether) the phase separation line meets the line of superfluid transitions. The disappearance of the phase separation signatures is not surprising if phase separation ends at a tricritical point as in bulk mixtures. In the tricritical region the interface between the two phases becomes diffuse, with a width which scales as $L \sim |\rho_4 - \rho_3|^{-2}$ (ρ_4 and ρ_3 are the densities of the ^{4}He and ^{3}He rich phases), so any distinction between the phases is lost as one nears the tricritical point. If this also happens in aerogels, the nature of the phase separation must change when the interfacial width becomes larger than the average strand and pore sizes. However, in Fig. 5.3.3 the kink in the superfluid phase transition

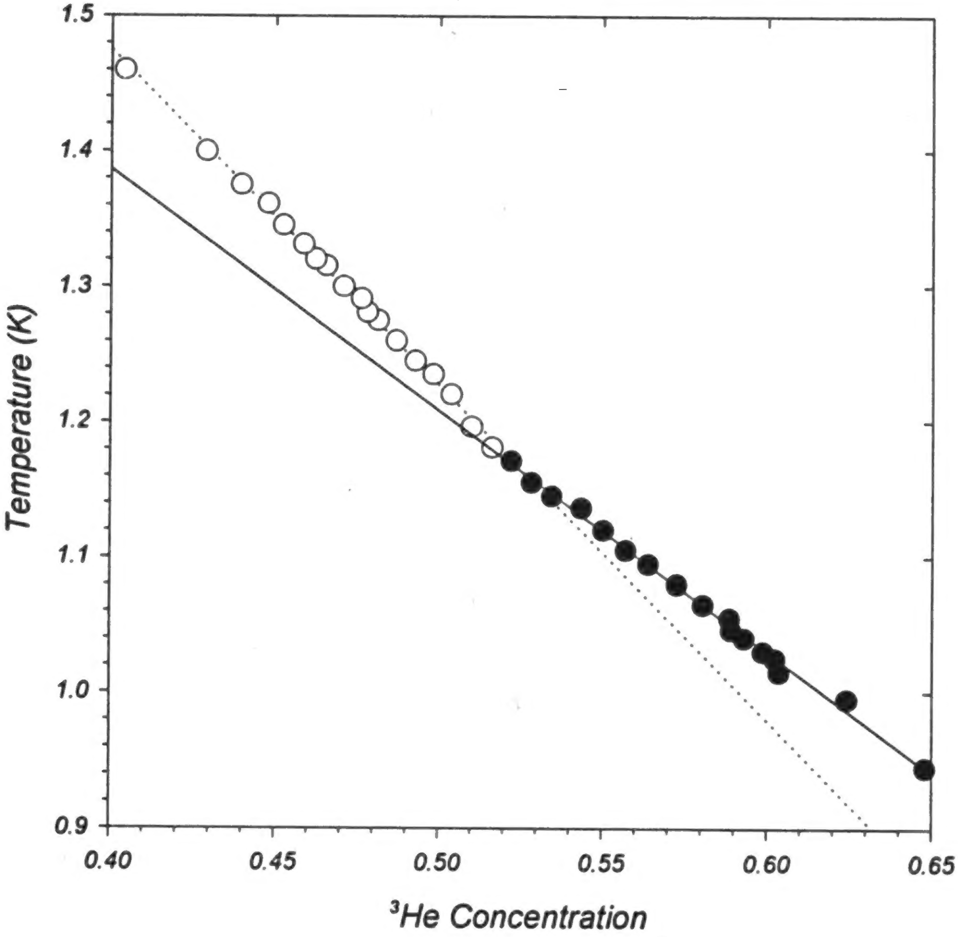

Figure 5.3.3. The "tricritical region" for the inert layer corrected phase diagram of helium mixtures in 87% aerogel showing the kink in the lambda line.

may indicate that the tricritical point is stable for mixtures in 87% aerogel, but at a higher temperature (1.15 K) than in bulk (T_{tr}=0.87 K).

In bulk mixtures the sound attenuation is known to be maximized at the tricritical point [28]. As the kink in the lambda line is suggestive of tricritical behavior we examine the attenuation data near $X^*=0.5$. Figure 5.3.4 is the raw data for a series of attenuation curves surrounding the region $X=0.5$. Once again the data represents an 11 MHz longitudinal mode and the attenuation curves have been offset for clarity; all concentrations are inert layer corrected. Qualitatively, adding ^{3}He decreases the peak heights and T_λ. Changes in the background accompany changes in X^*. A broad peak, presumably due to interaction of the aerogel two level systems and fluid, occurs at ~1.2 K for $X^*=0.4$ and moves to lower temperatures as more ^{3}He is added, displaying a maximum at ~0.9 K for $X^*=0.6$. To enable a more quantitative investigation, the background attenuation, as extrapolated from either side of the peak, can be subtracted. As with background subtraction of the velocity, the procedure is subjective, but does allow trends in the attenuation to be presented less ambiguously.

Figure 5.3.5 is the background subtracted attenuation data of the previous figure. With the background subtracted, the decrease in peak height with increasing ^{3}He concentration is clearly evident. While it is somewhat qualitative, there appears to be a change in the peaks on passing from below to above $X^*=0.5$. Below $X^*=0.5$, the data suggest the peak heights increase faster, and peaks are narrower than the corresponding high X^* attenuation peaks. There is no obvious asymmetry in the peaks on either side of $X^*\sim0.5$. With exception of the change in transition temperature with coverage, the behavior of these peaks mimics that found in thin films adsorbed onto Vycor [44]. Unlike bulk mixtures, however, where the tricritical point is associated with a maximum in attenuation [28], the attenuation decreases monotonically with increasing X^*.

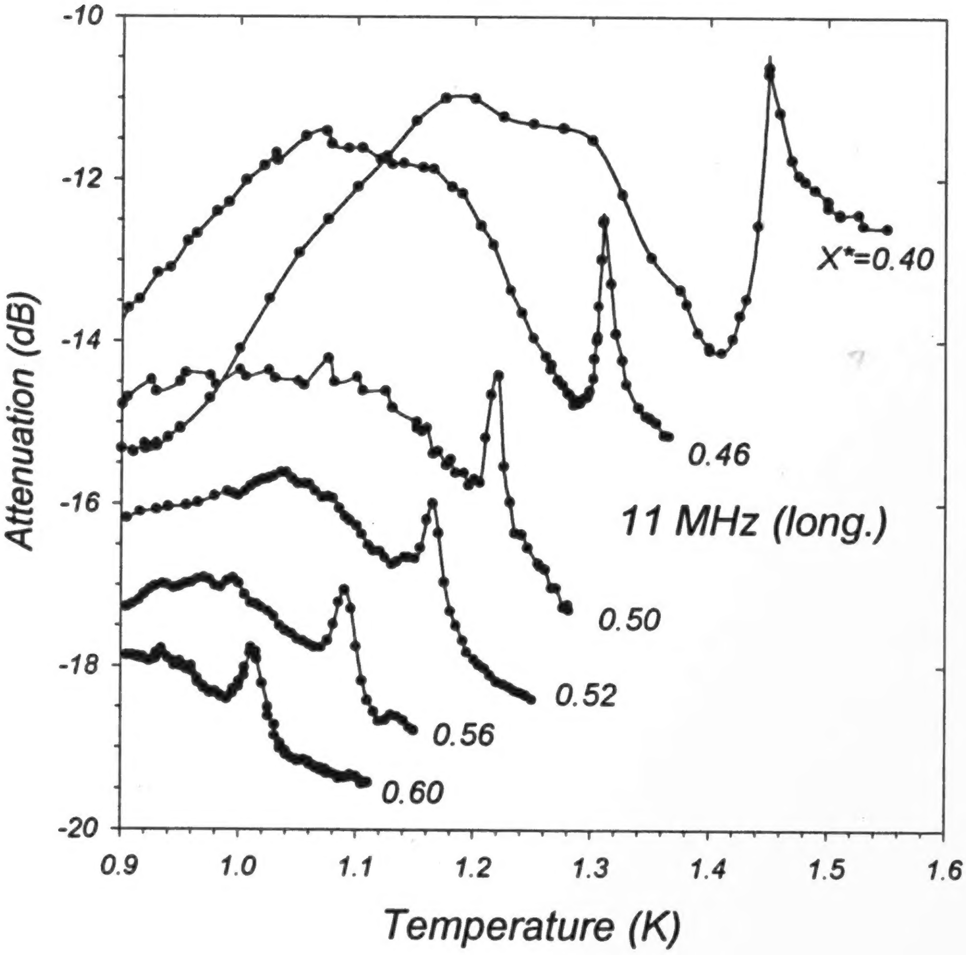

Figure 5.3.4. Raw attenuation data for 11 MHz longitudinal mode for concentrations on either side of the where the kink in the superfluid transition occurs. Note the concentrations quoted are inert layer corrected.

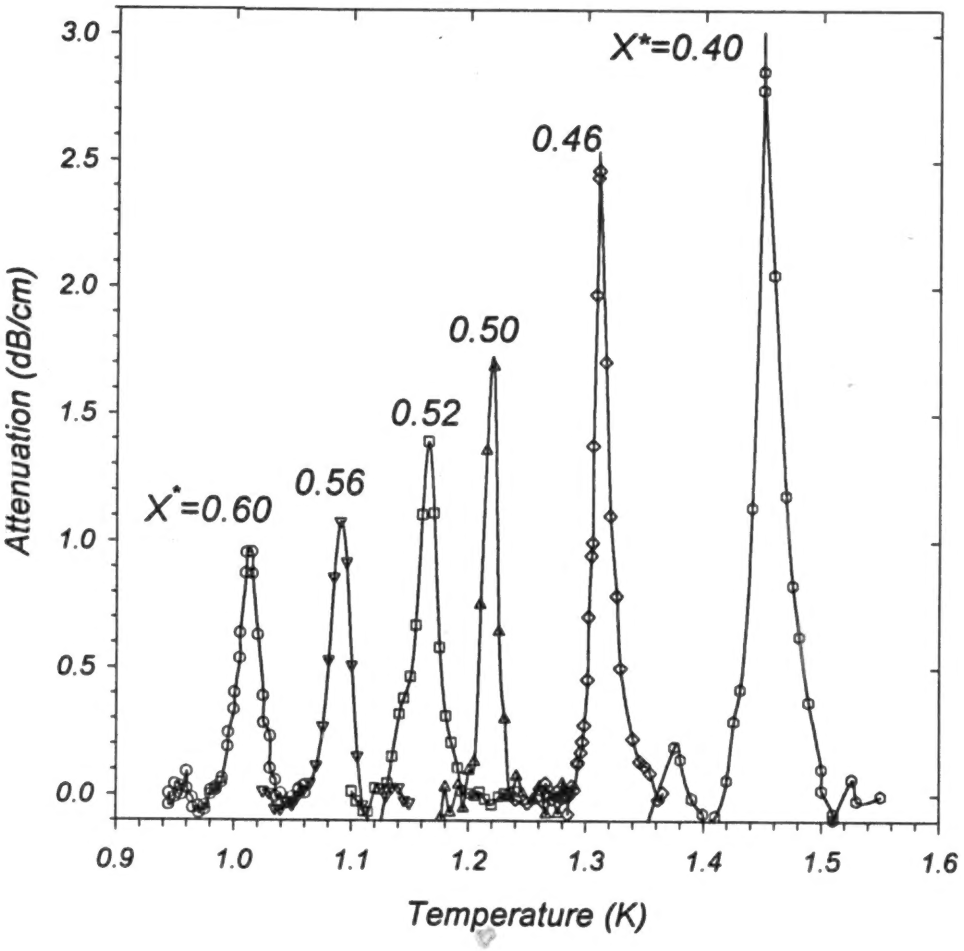

Figure 5.3.5. Attenuation near the kink in the superfluid transition. The quoted concentrations are inert layer corrected. The lines are guides to the eye.

5.4. Modeling the Density Effects in Helium Mixtures.

In this section we focus on the details of the phase separation in ^{4}He rich mixtures and from the analysis construct a model to aid in the interpretation of the high X* data. In particular we would like to investigate the possibility that the decoupling exhibited in the high X* velocity is due to a bulk-like phase separation.

There are two aspects to the velocity "jumps" at T_s: the first is that the magnitude of the velocity jump becomes smaller as ^{3}He is added; the second is that the velocity increase is short lived, occurring over a finite temperature span ΔT which also decreases with increasing X*. At first, these features might seem spurious and due, perhaps, to sample preparation or to the random configuration of the interface that forms during phase separation. However, the jumps are independent of frequency and ultrasonic mode (Fig. 5.4.1), vary systematically with X* and similar jumps are also found in torsional oscillator measurements on 98% aerogel, all of which suggests that the jump is due to a density change.

We now show that the magnitude of the jump can be semi-quantitatively understood in terms of the effective mass of ^{3}He atoms. When a ^{3}He atom moves through superfluid ^{4}He it contributes to the normal fluid density an effective mass m_3^* which arises from the backflow of superfluid [36, 60, 68]. Dash and Taylor [68] suggest the effective mass should decrease with the superfluid fraction, so that $m_3^*=m_3$ at the lambda temperature. This decrease is because the effective mass depends on the *relative* motion between the normal ^{3}He atoms and the (zero viscosity) superfluid component; if the superfluid density is zero, all the atoms move with the pore walls and there is no backflow. Dash and Taylor accounted for this correction by assuming $\Delta m= (m_3^*-m_3)\,\rho_s(T)/\rho_4$, which is the approach adopted here as well. Assuming the backflow contribution to the ^{3}He effective mass is proportional to $\rho_s(T)/\rho_4$, the change in the mass contribution when n_3^2 atoms move from the ^{4}He-rich superfluid phase, where each

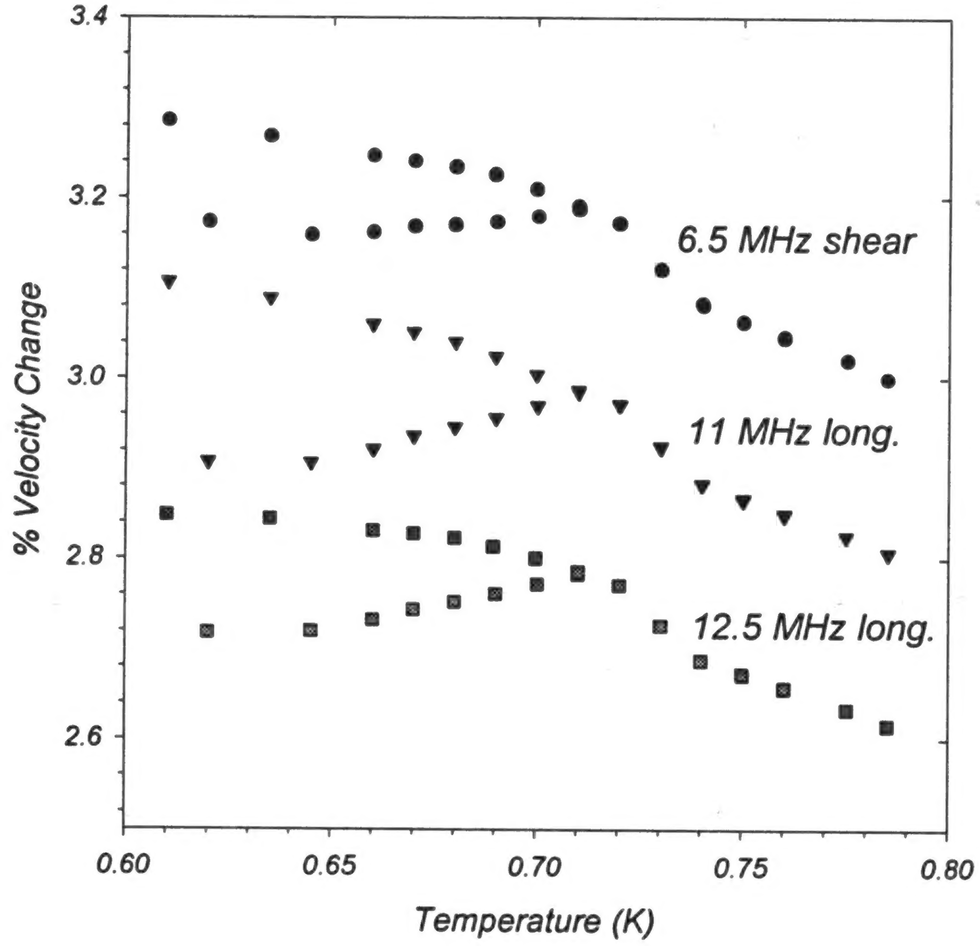

Figure 5.4.1. Comparison of the jump at phase separation in the ultrasonic velocity for three frequencies, 6.5 MHz shear, 11 MHz long., 12.5 MHz long.

contributes m_3^*, to the ^{3}He-rich normal phase, where each contributes m_3 is

$$\Delta m_3 = (m_3 - m_3^*)\frac{\rho_s(T)}{\rho_{4He}} n_3^2 \qquad (5.4.1)$$

and $n_3^2 = Nc_2x_2$, where x_2 and c_2 refer to the concentration and relative fraction of the ^{3}He-rich phase, respectively, and N is the total number of moles in the overall mixture. The sign of eqn. (5.4.1) is negative because as the ^{3}He atoms move out of the superfluid phase, their effective mass decreases from m_3^* to m_3; this is what gives rise to the jump in velocity at T_s. Note that c_2, as given by the lever rule, is zero at T_s and increases as the phase separation proceeds below T_s. Since the increase in velocity is proportional to the decrease in density (eqn. (4.4.9)), the velocity change below T_s is given by

$$\Delta\left(\frac{\Delta v}{v_o}\right) \approx (m_3^* - m_3)\frac{\rho_s(T)}{\rho_{4He}}\frac{Nc_2x_2}{2V_a(\rho_a + \phi\rho_f)} \qquad (5.4.2)$$

Equation (5.4.2) indicates the jump in velocity is proportional to the number density of ^{3}He atoms in the normal phase (n_3^2/V_a).

In order to apply eqn. (5.4.2) we need to determine the behavior of $c_2(X^*, T)$, for which we use bulk mixture properties. Figure 5.4.2 shows a plot of c_2, as determined by the lever rule, for a series of ^{4}He rich mixtures (X^*=0.15, 0.2, 0.3, 0.4). At phase separation c_2 is zero, but below T_s c_2 increases roughly linearly in T with a slope which increases with increasing X^*. A horizontal line in Fig. 5.4.2 indicates a particular fraction of atoms in the normal phase; here we have chosen, somewhat arbitrarily, the temperature where $c_2 = c_2^* = 0.03$. When $c_2 = 0.03$ the normal ^{3}He-phase is comprised of 3% of the total number of moles in the mixture. We point out that, due to the difference in molar volumes of the two isotopes, c_2 does not precisely correspond to the volume of the normal phase; however, over the range of concentrations (x_2) of interest, the variation

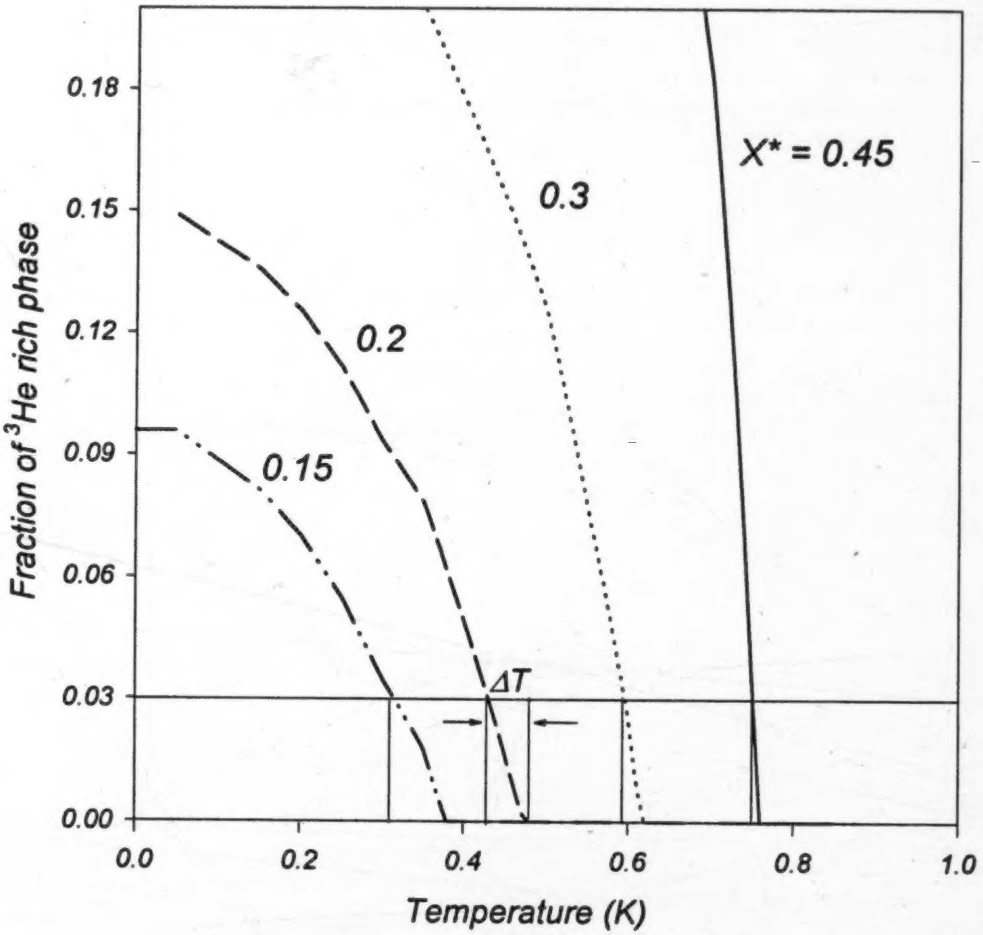

Figure 5.4.2. The relative fraction of the normal ^{3}He-rich phase as a function of temperature for mixture concentrations 0.15, 0.2, 0.3, and 0.45. The horizontal line represents the temperature where the normal fluid consists of 3% of the total molar fraction of the mixture. ΔT as defined by this line increases as X* decreases.

in volume is roughly 0.5%.

Figure 5.4.3 defines the measurements of ΔT and the velocity jump and shows a series of 11 MHz velocity curves. For this set of curves, as X^* increases, T_s increases while the magnitude of the velocity change and ΔT (the temperature span) decrease. The temperature span and the velocity jump are defined by changes in the slope of the velocity curve and in Fig. 5.4.3 are defined by the dotted vertical and solid horizontal lines, respectively. For example, the upper most curve corresponds to a concentration $X^*=0.08$. For this curve, the high temperature change occurs at ~0.44 K while the low temperature change in the velocity slope occurs at ~0.36 K. This temperature span is shown with the dotted vertical lines and is 80 mK. Using an identical procedure on the velocity axis, the velocity jump is ~0.22%. The above procedure allows the temperature span and the velocity jump to be determined as a function of the ^{3}He concentration spanning $X^*=0.05$-0.35.

In Figure 5.4.4 we compare the experimental values of the temperature span to the values of the temperature span required to achieve $c_2^*=0.03$ (from Fig 5.4.2). The experimental and calculated quantities are plotted in Fig. 5.4.4 as a function of ^{3}He concentration (X^*). The line is a guide to the calculated values. There is both qualitative and quantitative agreement between the two data sets, with some scatter in the calculated points due to inaccuracies in the values of the bulk mixture concentrations. The calculated (open circles) values are consistently lower. Increasing c_2^* would increase these, however, the exact value is not crucial and c_2^* appears to be between 3-4%.

The fact that the velocity increase below T_s does not continue to low temperatures, but rather stops when the ^{3}He-rich phase occupies about 3% of the volume, may be related to the aerogel structure. If nucleation of the normal phase occurs in the largest pores, i.e. as far from the aerogel surface as possible, then the 3% line might indicate the point at which the normal phase has filled these large pores and starts to

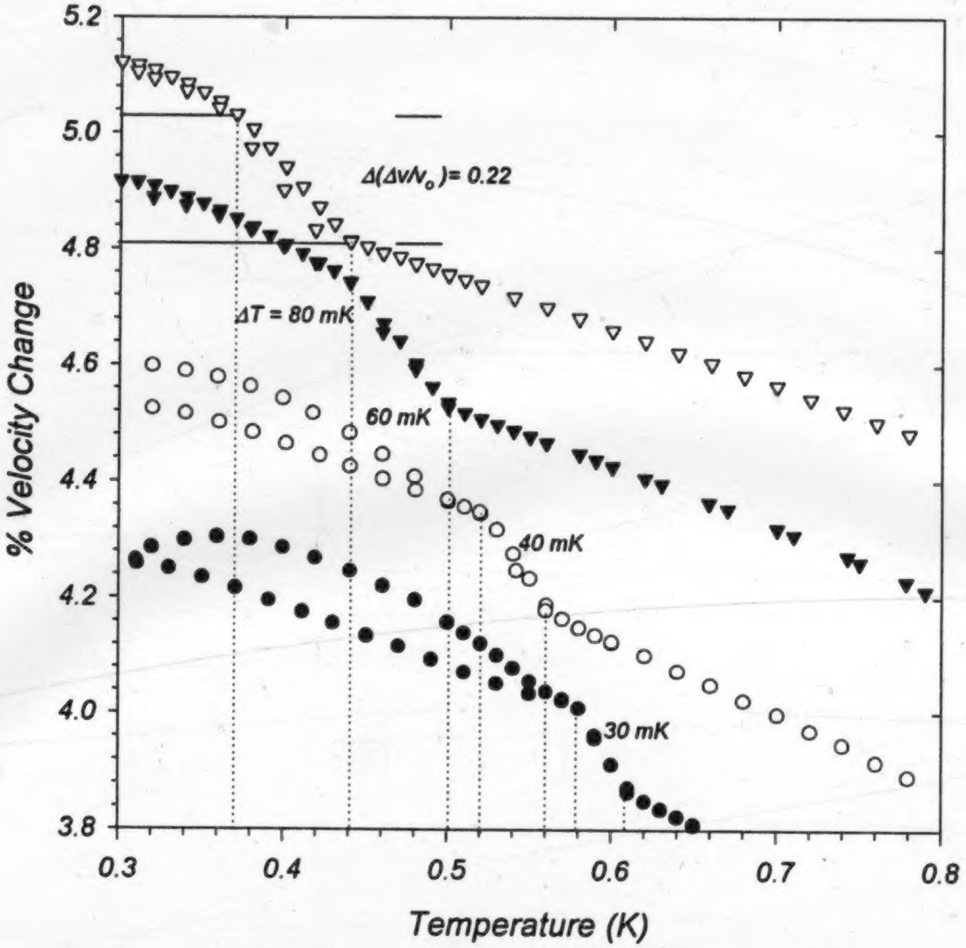

Figure 5.4.3. A series of 11 MHz velocity curves defining the experimentally determined values of the temperature span (ΔT) and the velocity jump occurring slightly above T_s.

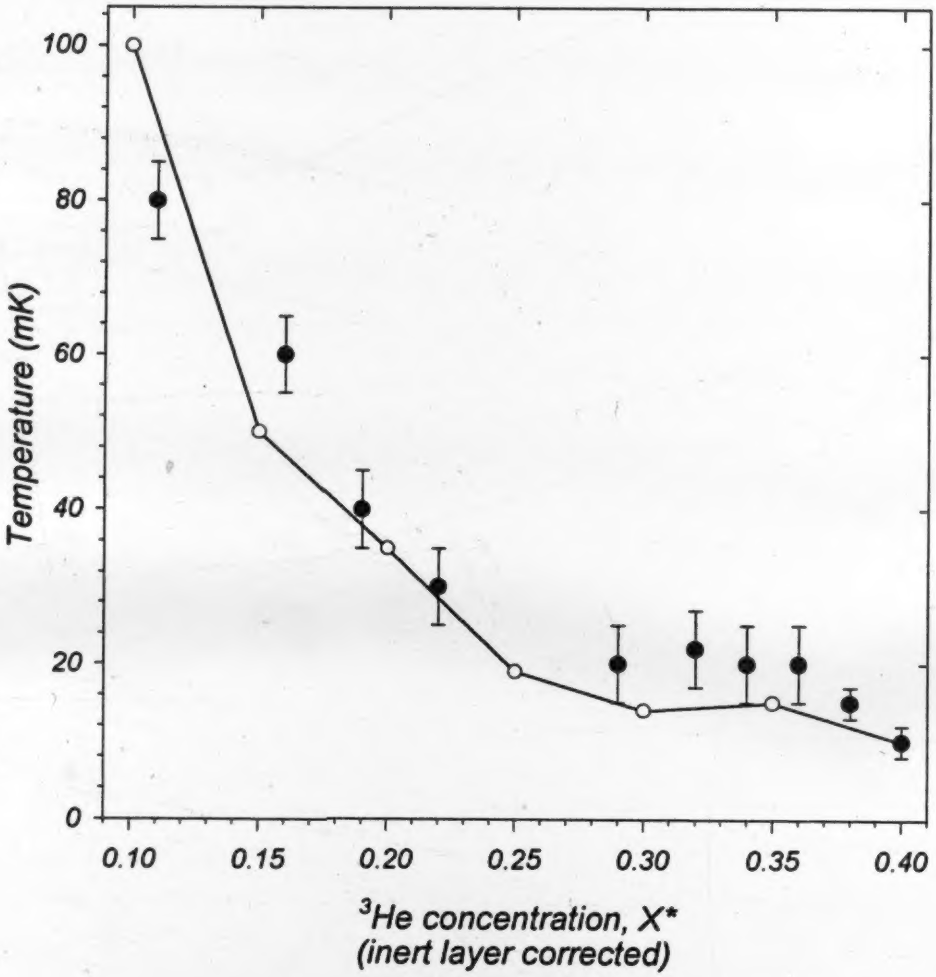

Figure 5.4.4. Temperature spans of velocity jump versus X. The experimentally (filled) determined temperature spans and those corresponding to nucleation of 3% of the normal phase, as predicted by the lever rule (open symbols).*

extend into smaller pore regions. At this point, the surface area between the phases would increase rapidly and the effective mass of the ^{3}He atoms at the interface would have to be taken into account. Since it has been suggested that the interface may be more than 10 Å thick [69, 72], the surface effective mass [60] may approach that of the fully immersed effective mass so there would be little change in the contribution to the density of a ^{3}He atom on further separation. This large pore model is consistent with hysteresis beginning when 3% of the mixture is in the normal phase rather than at T_s. Hysteresis is understood in terms of pinning of the interface between the two phases which would begin when the normal phase has filled the available large pore space. Torsional oscillator data on 98% aerogel data [16] show period jumps over temperature spans slightly larger than those found in 87% aerogel. This is reasonable since the larger pores in 98% aerogel would allow more normal phase before the interface reaches the aerogel, is pinned, and hysteresis begins.

Having determined the appropriate value of c_2 for eqn. (5.4.2), we plot the jump in the velocity at T_s versus $(\rho_s(T)/\rho)Nc_2x_2/2V_a(\rho_a+\phi\rho_f)$ in Fig. 5.4.5. The superfluid fraction $\rho_s(T)/\rho_{4He}$ is estimated by fitting the behavior in a filled aerogel at low X* to a 4th order polynomial and scaling the result in terms of the reduced temperature, T/T_λ (for $T_s<T_\lambda/2$ the superfluid fraction is roughly unity so this term is not very important over the range of concentrations where a "jump" is found); c_2x_2 is calculated from the lever rule using the bulk phase diagram. The data correspond to X* ranging from 0.4 to 0.1. Despite some scatter in the data, the jump in velocity is described reasonably as a linear increase.

From eqn. (5.4.2), the slope in Fig. 5.4.5 is related to the excess mass contribution of ^{3}He atoms in a superfluid mixture. The best fit to the data gives $m_3^*-m_3=4.4\pm0.6$ g/mol, or $m_3^*=(2.5\pm0.2)m_3$ with the uncertainty in the effective mass arising from the uncertainty in c_2^*, which is taken to be between 0.03 and 0.04 in accordance with Fig. 5.4.4. The value of $2.5m_3$ is in reasonable agreement with previous

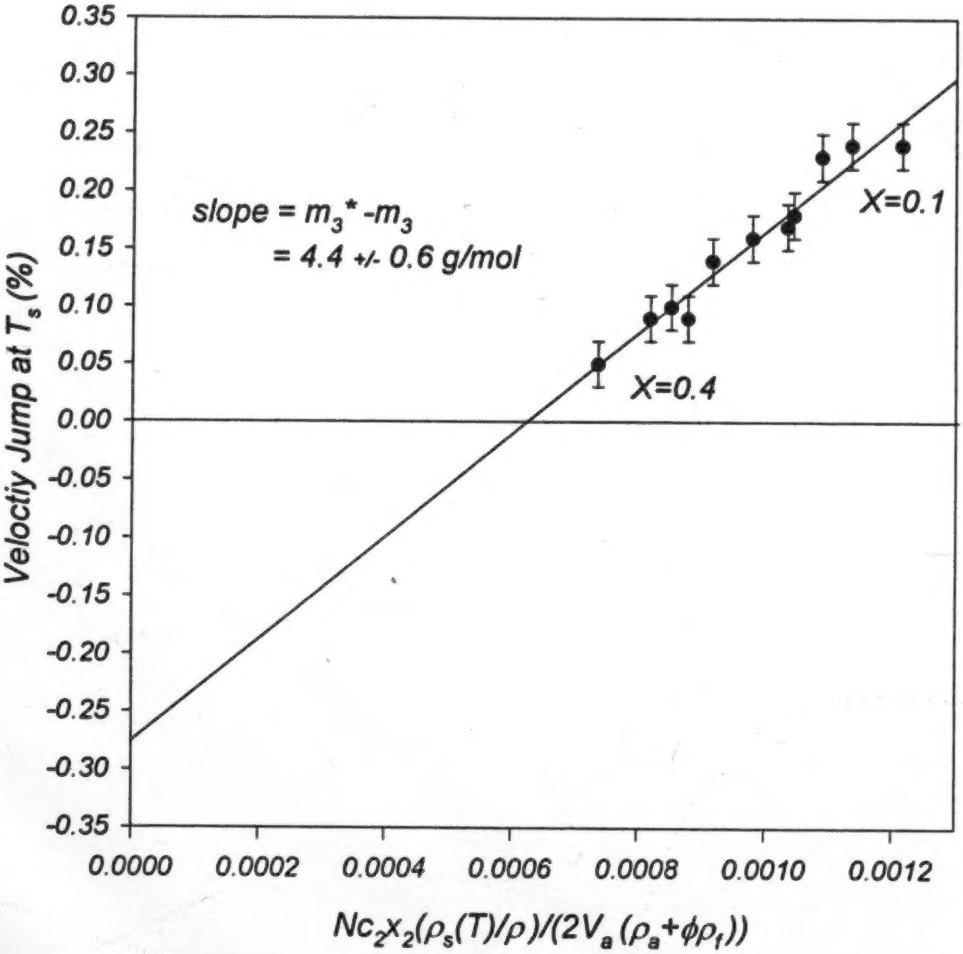

Figure 5.4.5. The magnitude of the velocity jump at T_s versus the number density of ^{3}He atoms in the normal phase when c_2 =0.035.

estimates of m_3^* in bulk mixtures; it is larger than the classical backflow estimation ($1.9m_3$) and the value from torsional oscillator methods above 1 K ($2m_3$) [68], but is close to the Fermi-liquid prediction of $2.3m_3$ [69, 70].

Note that the line in Fig. 5.4.5 has a negative intercept, −0.27%, and that the velocity jump magnitude decreases with increasing X^*. The negative intercept reflects the fact that if the phase separation was occurring from the high X^* side of the phase diagram, the velocity jump would be negative. This is reasonable since ^{3}He atoms then move from the normal phase to the superfluid phase and the resulting superfluid backflow would increase the effective density.

Moving to higher X^* (~0.45), the jump is replaced by a "dip" and the hysteresis disappears. The dip is attributed to a decrease in the superfluid fraction at phase separation. This can be seen as follows. We can model the superfluid density as being proportional to the number of ^{4}He atoms available to participate in superfluidity, $(N-n_c)(1-X^*)$. The temperature dependence of the superfluid fraction is estimated from that of filled aerogel at low X^*, scaled in terms of the reduced temperature, $t=1-T/T_\lambda(X^*)$, and normalized to unity at T=0 K. Note the lambda transition temperature is a function of concentration and $\rho_s(X=0, t)$ is a universal function for all ^{4}He concentrations. The assumed superfluid density, as a function of ^{4}He concentration and reduced temperature is

$$\rho_s(X^*,t) = \begin{cases} (1-X^*)\rho_s(0,\ t) & T_s<T<T_\lambda \\ c_1(1-x_1)\rho_s(0,\ t_1) & T<T_s \end{cases} \tag{5.5.3}$$

where c_1 and x_1 are the molar fraction and concentration of the ^{4}He-rich superfluid phase below T_s. The superfluid density T_s of the ^{4}He-rich phase below T_s is determined from a reduced temperature, $t_1=t_1(x_1(T))$, which is *concentration dependent* and leads to a slight increase in the superfluid fraction as the temperature is decreased. However, this increase is overcome by the decrease in the molar fraction c_1 with temperature. More intuitively, the decrease in the superfluid fraction on phase separation is due to ^{4}He atoms, a fraction of which are assumed to come from the superfluid portion of the mixture, contributing to the normal ^{3}He-rich phase, thus reducing ρ_s.

Having described the "dips" and the "jumps" in the velocity curves which occur at phase separation, a set of calculated velocity curves is presented in Fig. 5.4.6. The model generates velocity curves for a given concentration X* using the bulk mixture phase diagram parameters: T_λ, T_s, x_1, x_2; the superfluid fraction is obtained as described above. Equation (5.4.2) describes the "jump" in velocity at phase separation and eqn. (5.4.3) describes the continuous change in the superfluid fraction below T_s. The experimentally determined value of c_2=0.035 is the only adjustable parameter in the model and it is constant for all curves. Since the bulk properties were only calculated at a limited number of points, the change in the velocity at phase separation was modeled simply as a vertical shift (positive) calculated using c_2^*.

The calculated velocity curves in Fig. 5.4.6 mimic the experimental data in Fig. 5.2.1, reproduced here for convenience in Fig. 5.4.7. The period change from torsional oscillator measurements are also presented for comparison (Fig. 5.4.8). The generated curves correspond to inert layer corrected concentrations ranging from X*=0.2 to 0.89. For concentrations $X<X_{tr}$, the curves contain all the essential elements of the experimental curves: T_λ decreases with ^{3}He content; a jump in velocity at T_s occurs for X*=0.2−0.4, but at a concentration of X*=0.52, is replaced by a prominent "dip." This agreement is not surprising as the features have been "built in" to the model. The important point is that bulk mixture values (with the exception of the ρ_s dependence) have been used to model the aerogel-mixture curves. For $X^*<X_{tr}$, the ultrasonic velocity and torsional oscillator period are similar, phase separation causes jumps at low X* and dips at higher X*.

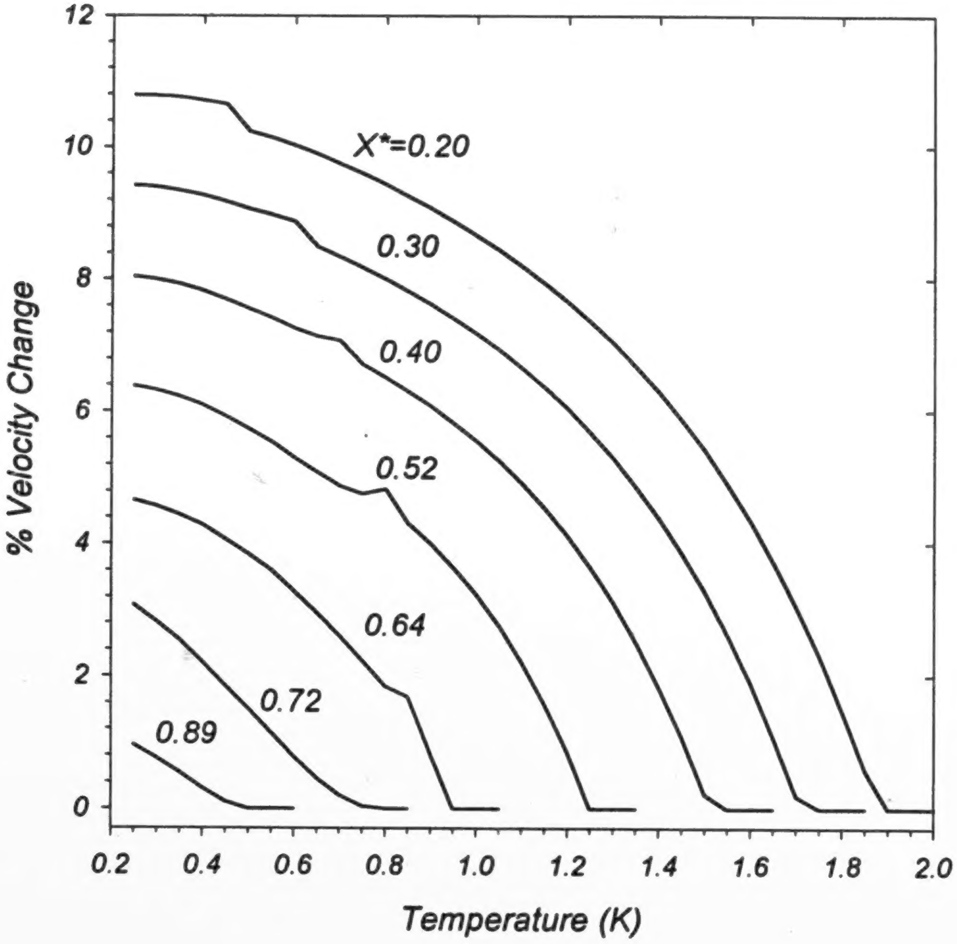

Figure 5.4.6. Computer generated velocity curves modeling the superfluid increase after bulk, the dips in velocity after the decrease in the superfluid fraction at T_s, and the jumps as the ^{3}He effective mass contribution. The concentrations are inert layer corrected.

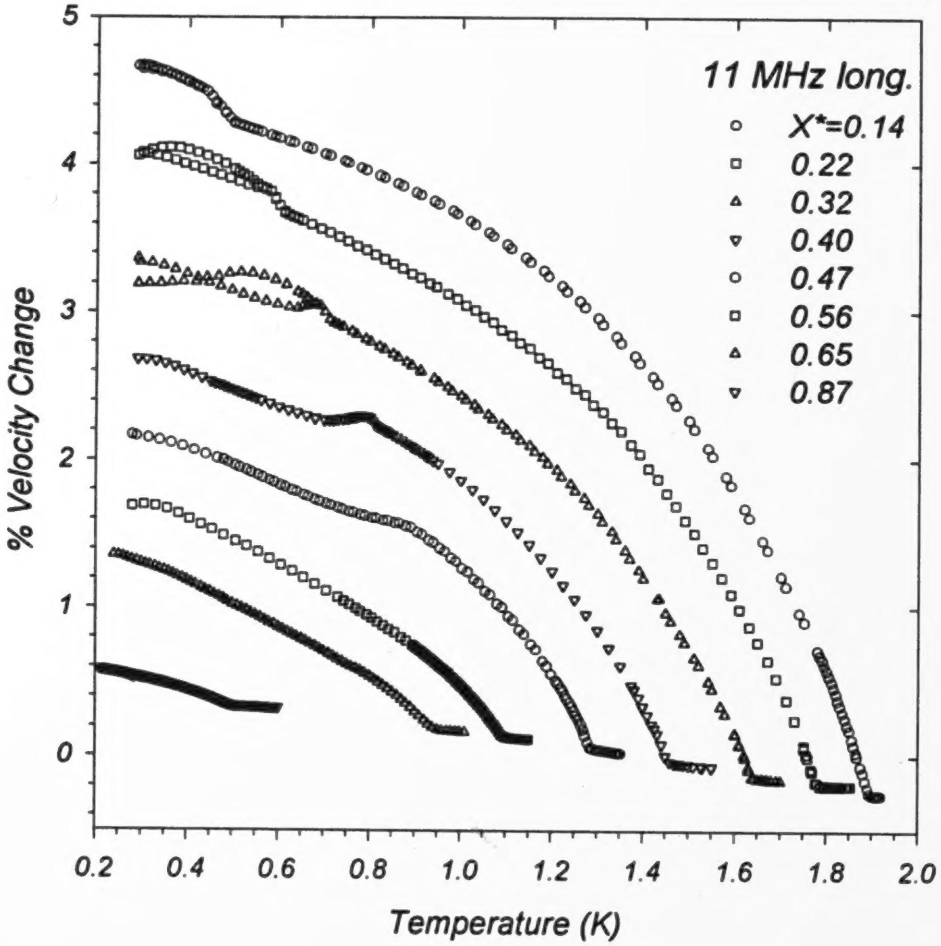

Figure 5.5.7. 11 MHz data for a series of mixtures. Concentrations are inert layer corrected to allow for comparison with the previous figure.

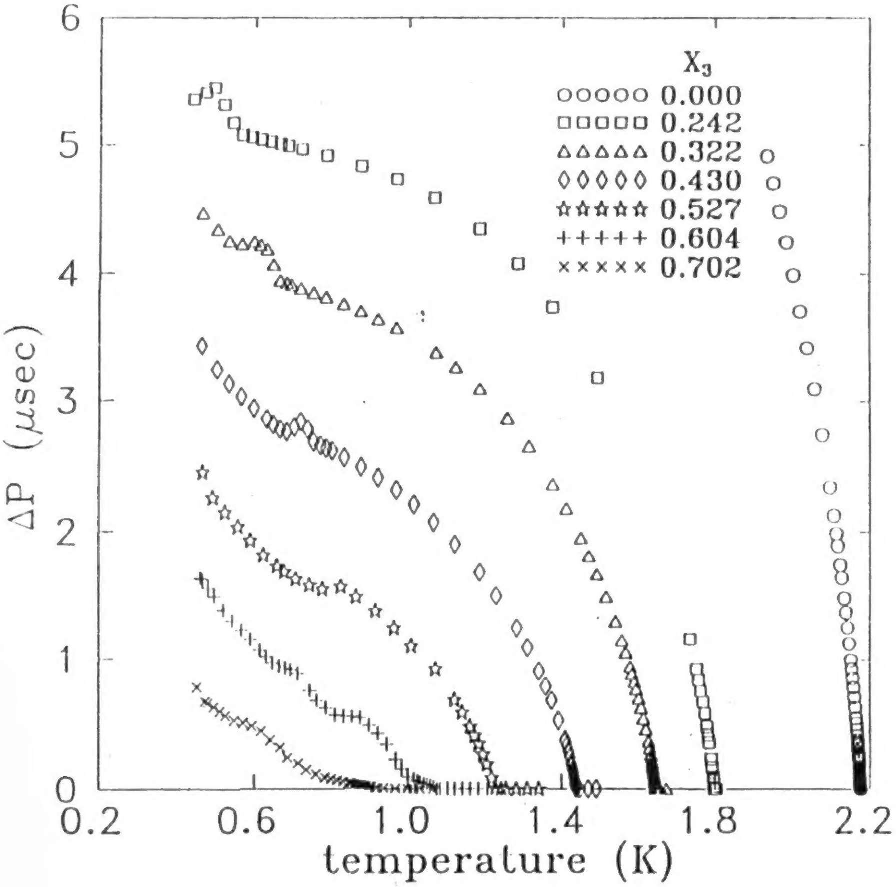

Figure 5.4.8. Change in period (ΔP) from torsional oscillator measurements on 98% aerogel. Data courtesy of M. Chan.

One rather large discrepancy between Figs. 5.4.6 and 5.4.7 is the magnitude of the velocity change associated with the superfluid decoupling. There are no adjustable parameters in the model, but it predicts an 11% increase in the sound velocity for a mixture of $X^*=0.20$; however, the experimental velocity change for a corresponding mixture is only 5%. The reason for this discrepancy is two-fold. The model does not take into account tortuosity effects and it neglects the modulus contribution of the liquid in a longitudinal mode. The latter effect was shown in Chapter 2 to reduce the velocity changes in a longitudinal mode by a factor of 0.8 compared to those for a shear mode. We have also seen that the inertial coupling described by the tortuosity is important for ^{4}He films; the discrepancy between the model and the experimental data suggests that this is true for helium mixtures as well. The tortuosity effects in mixtures are discussed further in Section 5.6.

Since the velocity curves in the $X^*<X_{tr}$ side of the phase diagram can be semi-quantitatively understood using bulk mixture properties, we extend the model to mixtures with concentrations $X^*>X_{tr}$ to explore the possibility that the lambda-like behavior found at high X^* might be produced by a bulk-like phase separation. The predictions of the model at high X^* are now compared to the experimental velocities in Fig. 5.4.9. This figure shows three velocity curves corresponding to two mixture measurements (open symbols) and a curve generated by the above phase separation model (line). The curves have been scaled in the usual manner with respect to their respective transition temperatures, T/T_λ, and normalized so that $\rho_s(T=0)=1$. The difference between the mixture and the model is apparent; from Fig. 5.4.9 the superfluid fraction generated using bulk mixture parameters increases more slowly than is found in experiment. The low density of data used for the model does not show this clearly, but the model predicts a linear increase in the superfluid fraction just below T_s. In the model, the increase in the superfluid fraction is governed by the increase of the molar fraction, c_1, as determined by the lever rule. In bulk phase separation, the superfluid fraction that appears is (at least for X^* away from X_{tr}) far from its critical region and so the transition is not a lambda

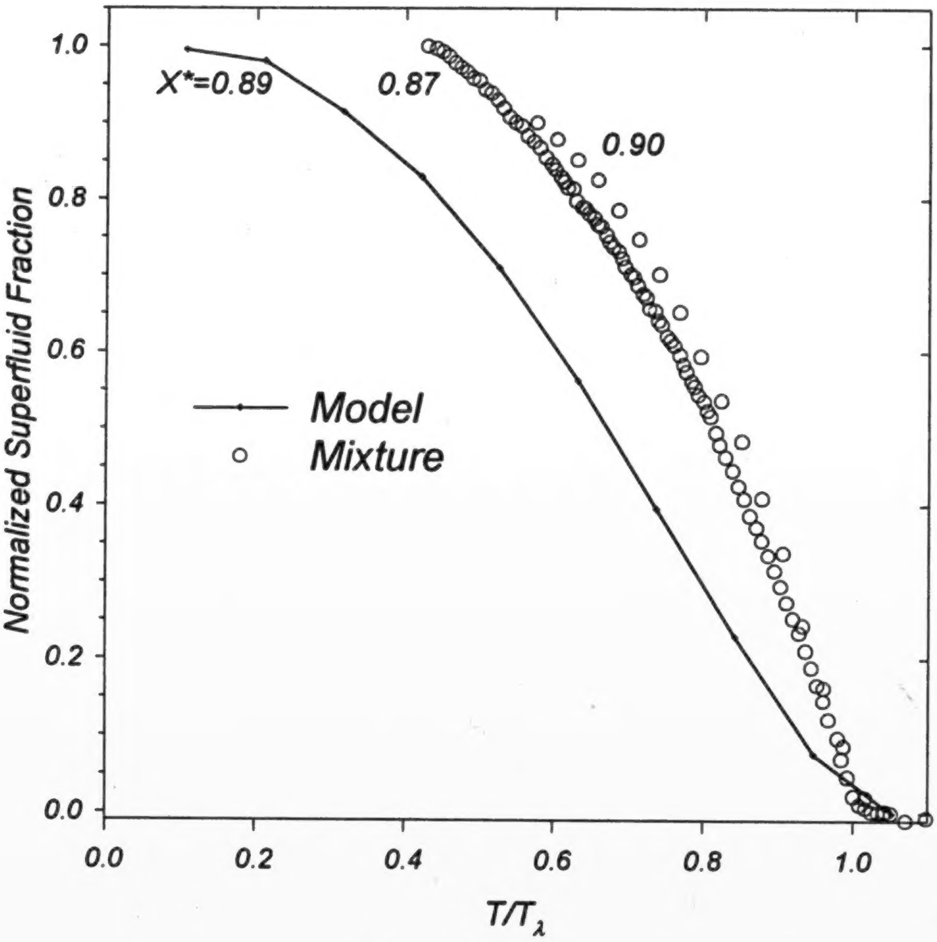

Figure 5.4.9. Comparison of velocity data for two mixtures (filled circles), corresponding to transition temperatures of 0.37 K and 0.49 K and data predicted by model (line) with T_λ=0.47 K.

transition, but rather a first order phase separation. If the $X^{*}>X_{tr}$ data could be described by a bulk phase separation type of transition, then we would expect decoupling of the superfluid phase, but the superfluid fraction would be governed by the lever rule. As Fig. 5.4.9 shows, a bulk-like phase separation is insufficient to explain the experimentally determined superfluid density behavior in the high X^{*} region.

Returning again to the torsional oscillator data on 98% aerogel, the high X^{*} data look different from both the model prediction (Fig. 5.4.6) and the ultrasonic velocity measurements in 87% aerogel (Fig. 5.4.7). This comparison suggest that the 98% aerogel phase diagram is different from the 87% system in the high X^{*} regions and that both are quite different from the behavior expected bulk mixtures.

Earlier we argued that the ultrasonic data at high X^{*} indicates critical behavior because of the attenuation peak accompanying the transition. As phase separation in bulk mixtures is a first order transition, the superfluid phase should nucleate well away from its critical temperature and thus should not display critical behavior. In this section we have compared the ultrasonically measured variation of the superfluid fraction to a model based on bulk mixture phase separation. Here we have also shown that a bulk-like phase separation is also not adequate to describe the temperature dependence of the superfluid fraction of high X^{*} helium mixtures in 87% aerogel.

5.5. Comparison with Film Data

We now consider whether the lambda-like transition at high ^{3}He concentrations, X^{*}, may be due to preferential localization of ^{4}He at the aerogel surface due to its lower zero point motion. The behavior of the mixtures might then be expected to parallel that of pure ^{4}He films with a coverage dependent superfluid transition and associated critical behavior. This possibility was discussed by Kim et al. for 98% aerogel where they found substantial differences in the superfluid behavior [16], most notably in how the transition temperature and superfluid decoupling varied with coverage. We take this procedure one step further and compare the tortuosities of the films and mixtures over the entire range of coverages.

In order to compare the film and mixture data, all the film data are converted to an "equivalent concentration". This calculation is based on the assumption that the ^{3}He in the mixtures resides on top of the ^{4}He film and occupies all the remaining pore space. All concentrations are corrected for the inert layer of ^{4}He, i.e. 427 μmol is subtracted from the value of all ^{4}He adsorptions. For example a film formed by adsorbing a total of n_4 moles of ^{4}He corresponds to an equivalent concentration

$$X^* = \frac{\phi V_a - n_4 v_4}{\phi V_a - n_4 v_4 + (n_4 - 427) v_3} \tag{5.6.1}$$

where v_3 and v_4 are the molar volumes of the isotopes at 1 K and ϕV_a is the pore volume of the aerogel.

Figure 5.5.1 is a comparison of the 6.5 MHz shear velocity of a series of mixtures (open circles) and pure ^{4}He films (filled circles). The background has been subtracted from all data shown. The mixtures, in order of increasing transition temperature, have corrected concentrations $X^* = 0.90, 0.87, 0.73, 0.65$. Equivalent concentrations of the films are 0.94, 0.85, 0.80, also with increasing transition temperature (the transition temperature for a film with 0.65 is at a much higher temperature and so is not shown). Note that a mixture and a film with the same (equivalent) concentration, would have the *same amount of ^{4}He*. In order to clearly distinguish between film and mixture data, we have underlined the film equivalent concentrations in Fig. 5.5.1.

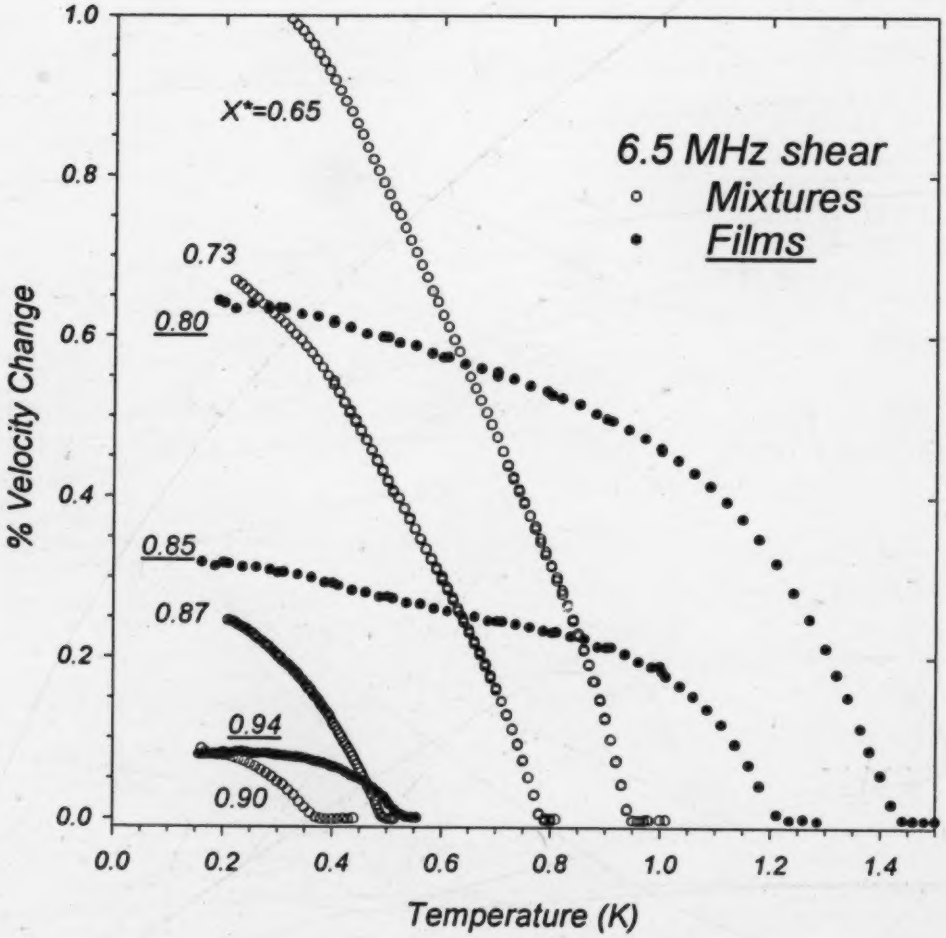

Figure 5.5.1. Comparison of ultrasonic velocity curves for ^{4}He films (filled circles) and helium mixtures (open circles). The mixtures correspond to X = 0.90, 0.87, 0.73, and 0.65 while the equivalent film mixtures are 0.94, 0.85, and 0.80.*

There are two points to note here. First, the transition temperatures of the films increase faster than those of the mixtures as ^{4}He is added. The X^*=0.87 mixture has T_λ~0.5 K while a comparable film, X^*=0.85, has a much higher transition temperature, 1.2 K. Second, the mixture X^*=0.87 has 8% less helium above the inert layer than the X^*=0.85 film, but the decoupling of the film is ~20% higher. This discrepancy could be due to a change in the inert layer over that of pure ^{4}He films [71].

The shapes of the velocity (superfluid fraction) curves in Fig. 5.5.1 are also qualitatively different. In the case of pure films decoupling is nearly completed by ~T_λ/2. This is seen most clearly in the X^*=0.94 data. In the mixtures however, the decoupling of the superfluid fraction continues to increase to the lowest temperatures.

Figure 5.5.2 compares shapes of the high X^* velocity curves for films and mixtures more directly by scaling the temperatures by the respective T_λ's and normalizing the superfluid densities to 1 at T~0. While the concentrations for the two sets of mixtures and films (grouped here as 0.87, 0.85 and 0.90, 0.94) are very similar, the transition temperatures are quite different. The mixture/film with X^*~0.87/0.85 are shown as the lower left curves with the superfluid density scale given by the left axis. The upper right mixture/film curves have slightly larger concentrations, 0.90/0.94, and have been shifted vertically for clarity; the right hand axis is for these curves. This comparison of the film and mixture data shows that the superfluid density of the films near T_λ increases faster than that of the mixtures, but that it levels off at lower temperatures while the superfluid density of the mixtures increases through the entire temperature range.

The effect of the temperature dependent background is quite noticeable in the film data. Below about 1 K this background is essentially linear. In films such as the X^*=0.94 one, the transition temperature is low enough (~0.5 K) that the background can be reliably extrapolated to T=0 and properly subtracted from the data. The resulting ρ_s is

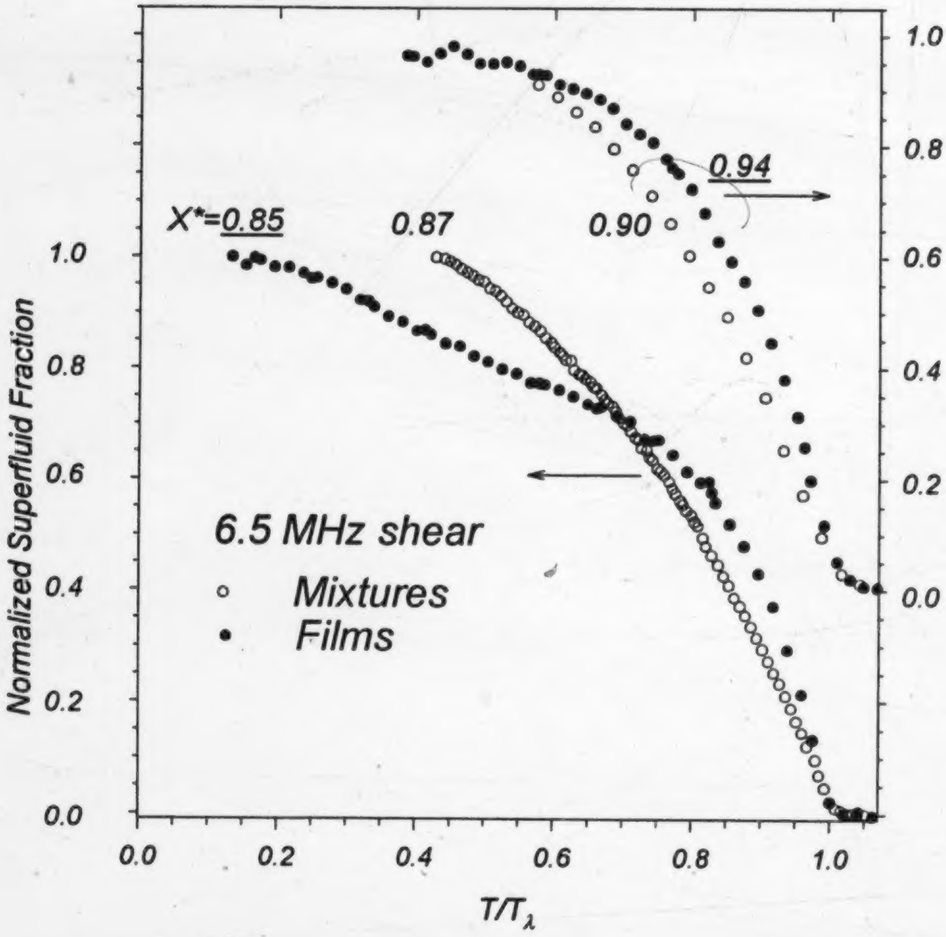

Figure 5.5.2. Comparison of velocity for ^{4}He films and mixtures. The temperature is scaled by T_λ and the superfluid density is normalized to 1 at T=0. The films are solid symbols, the mixtures are the open symbols. Mixtures are (X^*=0.87, T_λ=0.5 K) (0.9, 0.37 K), films are (0.85, 1.2 K) and (0.94, 0.52 K). The curves on the right have been vertically shifted for clarity.

nearly constant below about $T_\lambda/2$, as for pure ^{4}He and torsional oscillator experiments on films [48, 49]. However, for the film with $X^*=0.85$, T_λ is 1.2 K and the temperature dependent background below 1 K cannot be properly subtracted, distorting the apparent ρ_s. The mixtures do not suffer nearly as much from this problem since all the ^{3}He in the aerogel pushes the TLS background to lower temperatures.

A comparison of the transition temperatures of mixtures and films is displayed in Fig. 5.5.3. The entire gamut of concentrations is shown with all values corrected for the inert layer. Mixture data are the open circles showing a non-linear decrease in the lambda temperature as ^{3}He is added. The filled circles are the film data which show the linear decrease in T_λ near $X^*=1$ (i.e. the linear dependence on ^{4}He coverage shown in Chapter 4) and the approach to the full pore $T_\lambda=2.161$ K for small X^*. The disparity between the mixture and film data is evident from Fig. 5.5.3; T_λ in films increases very quickly with ^{4}He concentration ($=1-X^*$), whereas the mixture data has a much smaller slope, essentially that of the phase separation curve of bulk mixtures.

The difference between the superfluid behavior of pure ^{4}He films and helium mixtures in aerogel refutes the idea of a localized *pure* ^{4}He film when $T \sim T_\lambda$. The transition temperatures of pure films increase much faster than seen in mixtures in 87% aerogel and measurement of the superfluid fraction for mixtures in aerogel has shown that near the transition ρ_s/ρ falls in between films and bulk-like phase separation prediction. This latter finding suggests that the transition may be a combination of a film-like superfluid transition and a bulk-like phase separation where the ^{4}He "condenses" onto the aerogel strands, essentially thickening the film.

5.6. Tortuosity of Helium Mixtures

If a superfluid ^{4}He rich film has phase separated onto the strands, its tortuosity may differ from that of pure ^{4}He films because of the normal ^{3}He fluid in the pores. As

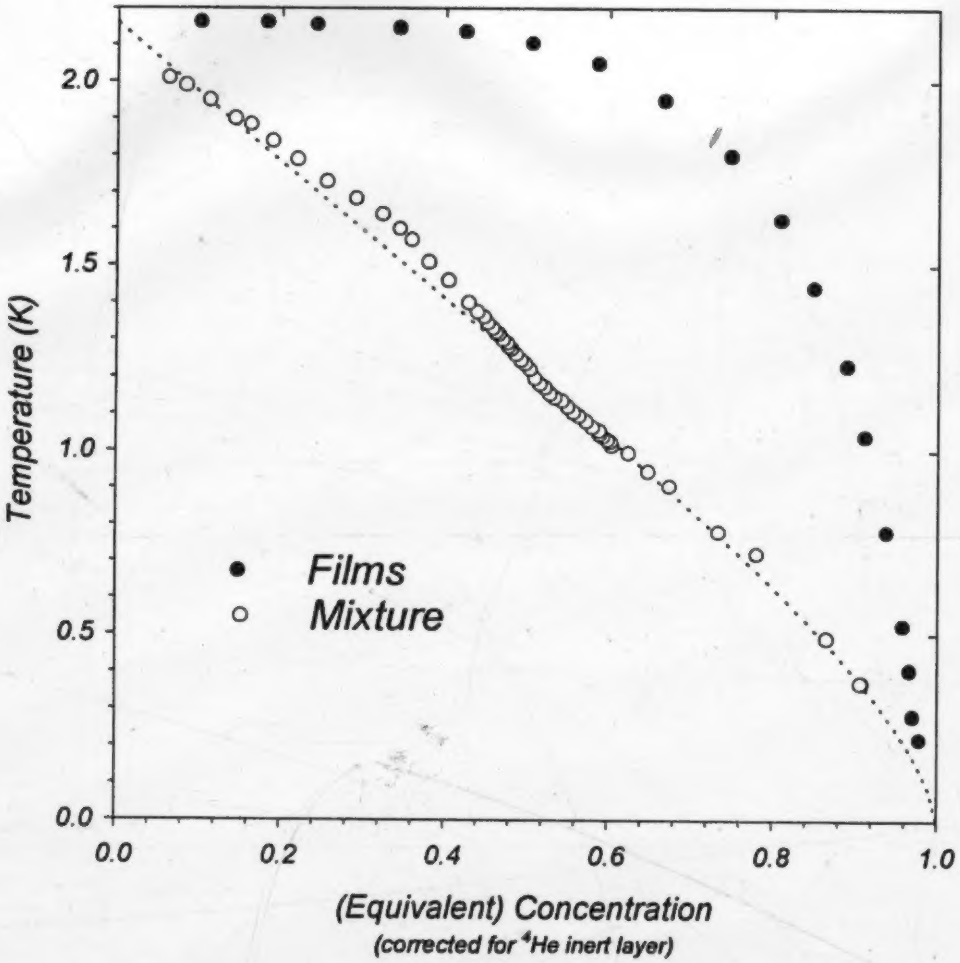

Figure 5.5.3. Comparison of the transition temperature for helium mixtures (open circles) and the corresponding pure helium films (filled circles). The dotted line is the expected transition temperature due to a decrease in the number density of bosons in the mixture.

previously discussed, the effective mass of ^{3}He in superfluid ^{4}He is about twice that of a bare ^{3}He atom and increases the effective density of the mixture. In pure ^{4}He the tortuosity is due to "pushing" of the superfluid by the pore walls; dissolved ^{3}He atoms allow additional inertial coupling through superfluid backflow. Adding ^{3}He atoms may increase the tortuosity, i.e. decrease the superfluid decoupling. Another way addition of ^{3}He may change the tortuosity is by effectively decreasing the porosity. In measurements in porous alumina, Bernard and Williams found that decreasing the porosity resulted in a large increase in the tortuosity [65]. Presumably the tortuosity becomes infinite when the percolation threshold is reached and the connectivity through the material is lost. We draw an analogy between measurements in porous alumina and high X* mixtures in an attempt to describe the change in morphology in the system.

5.6.1 Tortuosity Measurements

The tortuosities of helium mixtures are calculated using the background subtraction method discussed in Chapter 4. This requires the background velocity above T_λ to be extrapolated to T=0 K and subtracted from the data. The reason this method must be employed is illustrated by Figure 5.6.1.1 which shows 6.5 MHz shear velocity data for a series of concentrations X*=0.6, 0.57, 0.56, 0.54 and 0.53. As with previous velocity data, the transition temperature (T_λ), at which a sharp change in velocity occurs, increases with ^{4}He content (decreasing X*). The velocity above T_λ is linear but decreases systematically as ^{4}He is added. This is because the mixture density increases when ^{3}He (m~3) is replaced by ^{4}He (m~4). In contrast, the velocity at T=0 K increases with ^{4}He content due to the increased superfluid decoupling. In order to apply the other method used to calculate the tortuosity of films, namely the ratio of Δ_1 to Δ_2, the background due to the inert layer *and* that due to the current content of ^{3}He would have to be known for T~0 K and T=2 K; this would be very labor intensive. We instead apply the background subtraction method. All tortuosity calculations use the shear velocity data (6.5 MHz) to avoid bulk modulus corrections (Section 2.5.5).

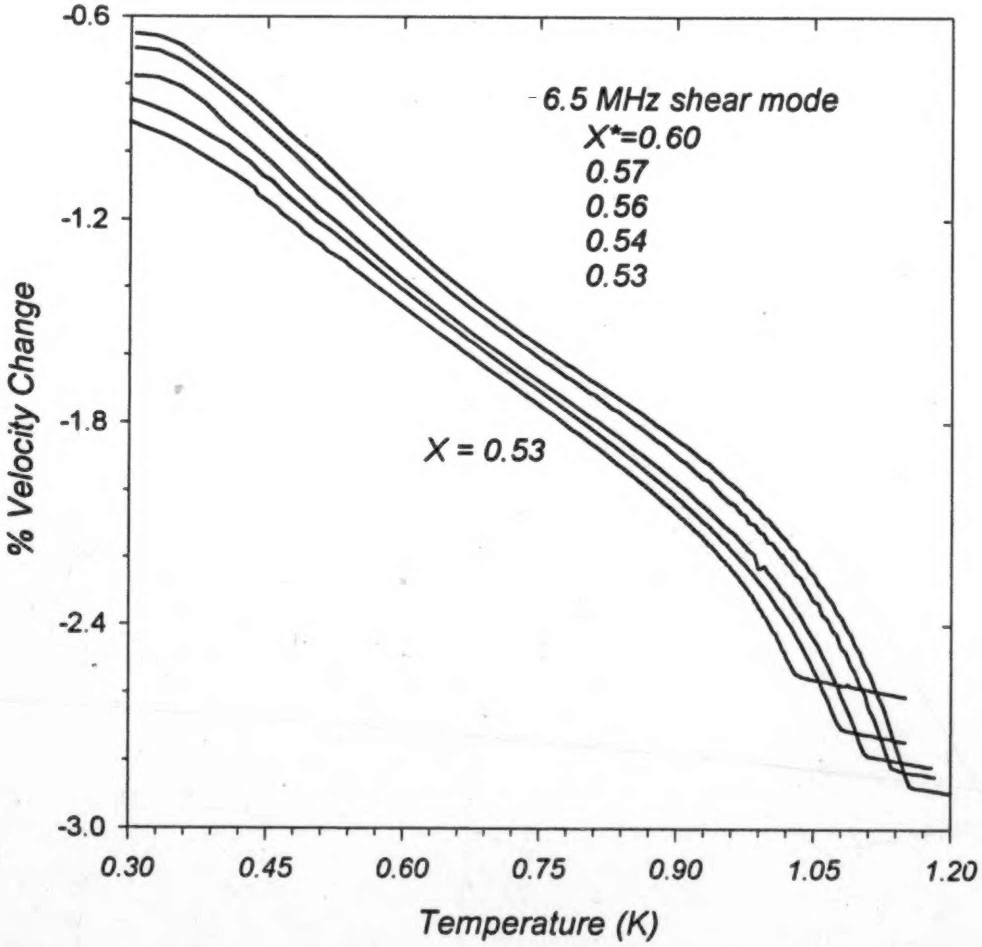

Figure 5.6.1.1 Raw velocity data for a 6.5 MHz shear mode for a series of mixtures with inert layer corrected concentrations X=0.6, 0.57, 0.56, 0.54, 0.53. Note the decrease in the velocity background above T_λ and the increase in the velocity at T=0 K with increasing ^{4}He content.*

Fortunately, the subtraction can be accomplished with some confidence in mixtures because the background is relatively linear over a wide range of concentrations and filling the pores has moved the TLS interactions to low temperatures. The tortuosity is then given by

$$\alpha \approx \frac{(n_4-n_c)m_4}{2(m_a+n_3m_3+n_4m_4)\Delta_3} \approx \frac{(n_4-n_c)m_4}{2m_a\Delta_3} \qquad (5.6.1.1)$$

where n_c is the assumed inert layer and Δ_3 is the change in velocity at T=0 K. We have made the assumption that the aerogel density is much larger than that of the fluid which, in the case of aerogel, is tenuous, but it does not qualitatively change data. The tortuosities of the mixtures are compared to those for ^{4}He films in Fig. 5.6.1.2. The ^{4}He film coverages are converted to the (equivalent) inert layer corrected ^{3}He concentrations, X*. The filled circles represent the film data and the open circles represent the helium mixture tortuosity. The film tortuosity data is abridged here to highlight the trends.

Starting with X*=0 (pure ^{4}He/full pores), the tortuosity is 1.5 which agrees with an extrapolation of the film data. At higher concentrations the tortuosity α_m parallels, but is offset from the film tortuosity, α_f. At a concentration X*~0.5 the mixture tortuosity increases sharply while the film tortuosity increases smoothly. At the highest ^{3}He concentration, X*~0.85, α_m is ~8, in contrast to films which are limited to α_f=4.1 for the thinnest films (highest X*). For helium mixtures, the tortuosities above and below X*=0.5 both increase roughly linearly with X* but with quite different slopes; the slope above X*=0.5 is about five times that below.

5.6.2 Tortuosity near T_λ

The sudden change in tortuosity at X*=0.5 and the large values for high ^{3}He concentration mixtures are intriguing. In order to investigate this behavior further, the

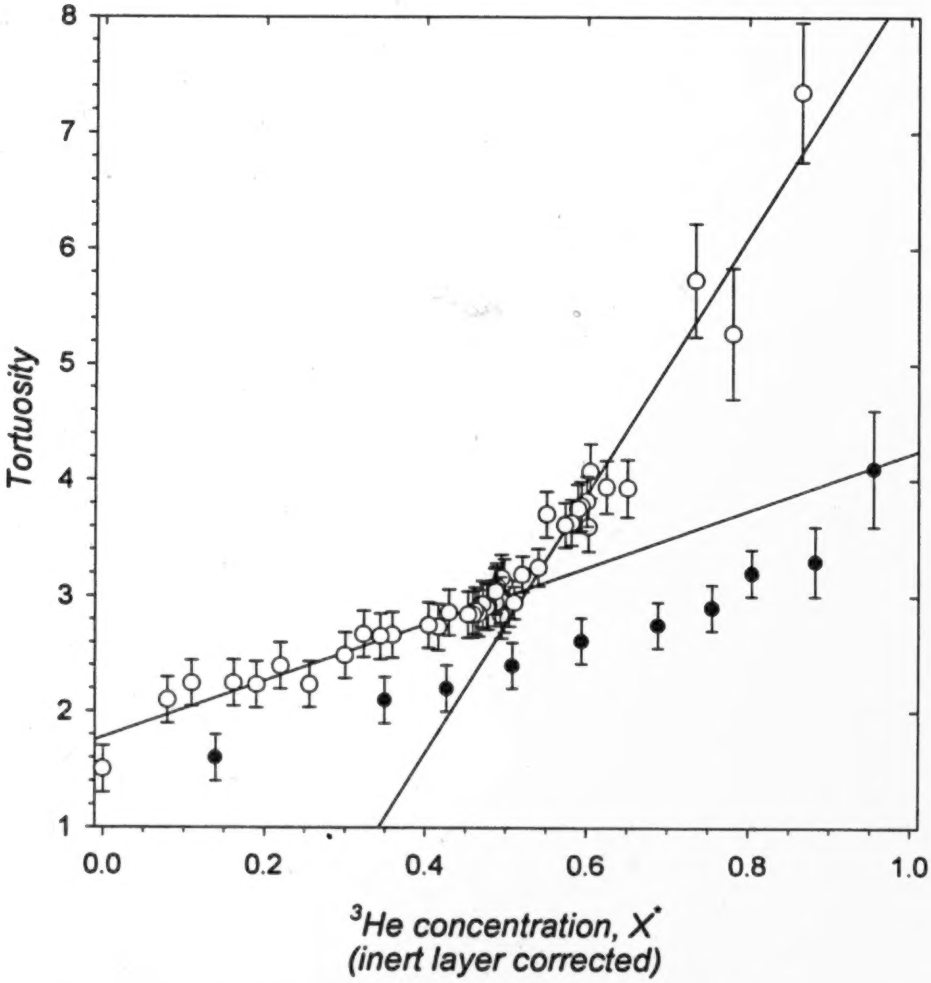

Figure 5.6.1.2. The tortuosity of helium mixtures (open circles) and pure helium films (filled circles) as a function of inert layer corrected ^{3}He concentration, X^*. The solid lines are fits to either side of X^*=0.5.

critical region was studied in more detail. As seen in eqn. (5.1.1), since the tortuosity is included in the measured amplitude (A_o) of the velocity-reduced temperature plot, any anomalous behavior in α should be reflected in the critical amplitude. Furthermore, in recent experiments, Crowell et al. found that the superfluid critical exponents for pure ^{4}He films on aerogel were quite different from that of full pore aerogel; $\zeta \approx 0.63$ for films compared to $\zeta=0.81$ for full pores [48]. This suggests that if there is a crossover from film-like to full-pore-like behavior in mixtures, it may show up as a change in the ρ_s exponent, specifically an increase. To this end the velocity change versus reduced temperature was plotted on a log-log plot (Fig. 5.6.2.1). As before, the transition temperatures are determined by the peaks in attenuation. Figure 5.6.2.1 shows such plots for a series of concentrations. These are linear over roughly an order of magnitude in reduced temperature ($0.01 \leq t \leq 0.1$). The data are 11 MHz longitudinal, used simply because they provided the most consistent results.

Figure 5.6.2.2(a) presents the critical exponents determined from the slopes. There is considerable scatter in the points and the uncertainty is due to fitting over slightly different temperature regions. The two solid horizontal lines indicate the bulk (lower, $\zeta=0.67$) and full-pore pure ^{4}He aerogel (upper, $\zeta=0.89$) exponents. The mixture data fall in between these two, with a (non-weighted) average value of by ~0.75.

Figure 5.6.2.2(b) compares the behavior on a semi-log plot of the total change in velocity at T=0K (open) to that of A_o (filled) defined by

$$\frac{\Delta v}{v_o} = A_o t^{\zeta} \qquad (5.6.2.1)$$

as a function of X* (inert layer corrected concentration). A_o is determined from a log-log plot of the velocity versus reduced temperature using data near T_λ. Both of these quantities should be (roughly) inversely proportional to the tortuosity. The quantities in 5.6.2.2(b) display very similar behavior over the entire range of concentration; on this

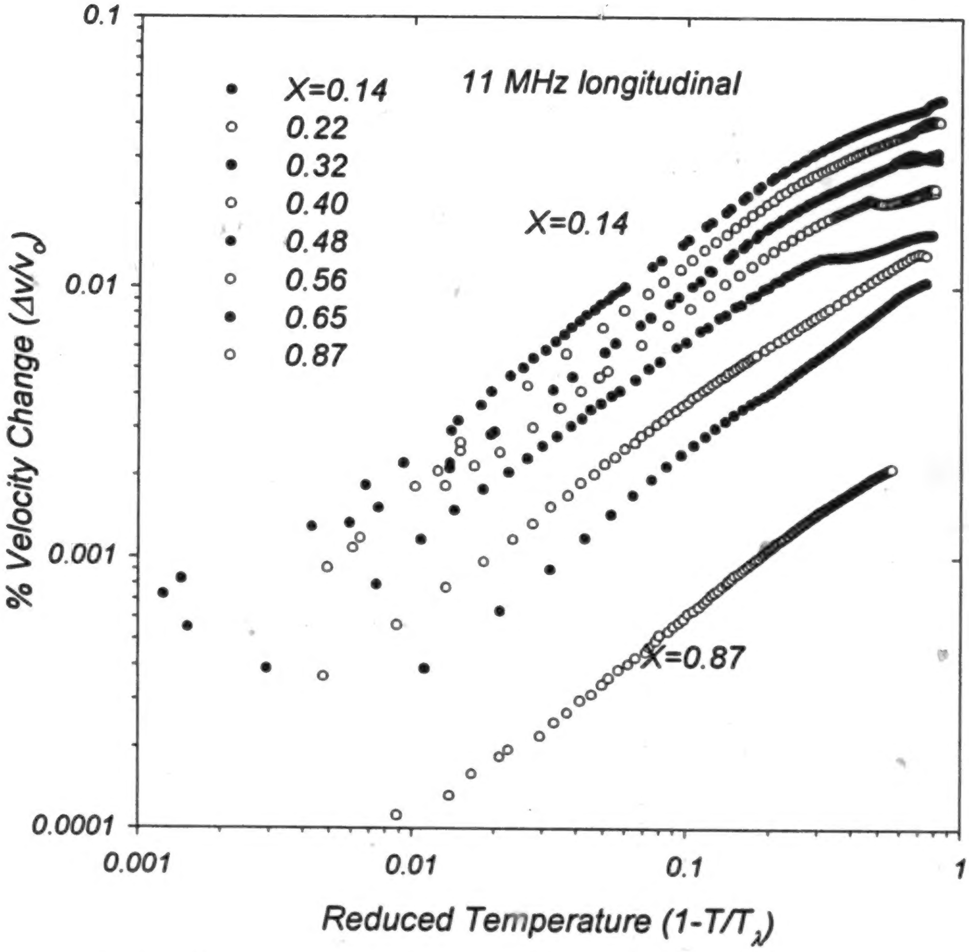

Figure 5.6.2.1. Log-log plots of the velocity versus the reduced temperature. The legend provides the concentrations from top to bottom. The corresponding T_λ (from top to bottom) are 1.9, 1.8, 1.65, 1.5, 1.3, 1.1, 0.95, and 0.5 K.

5

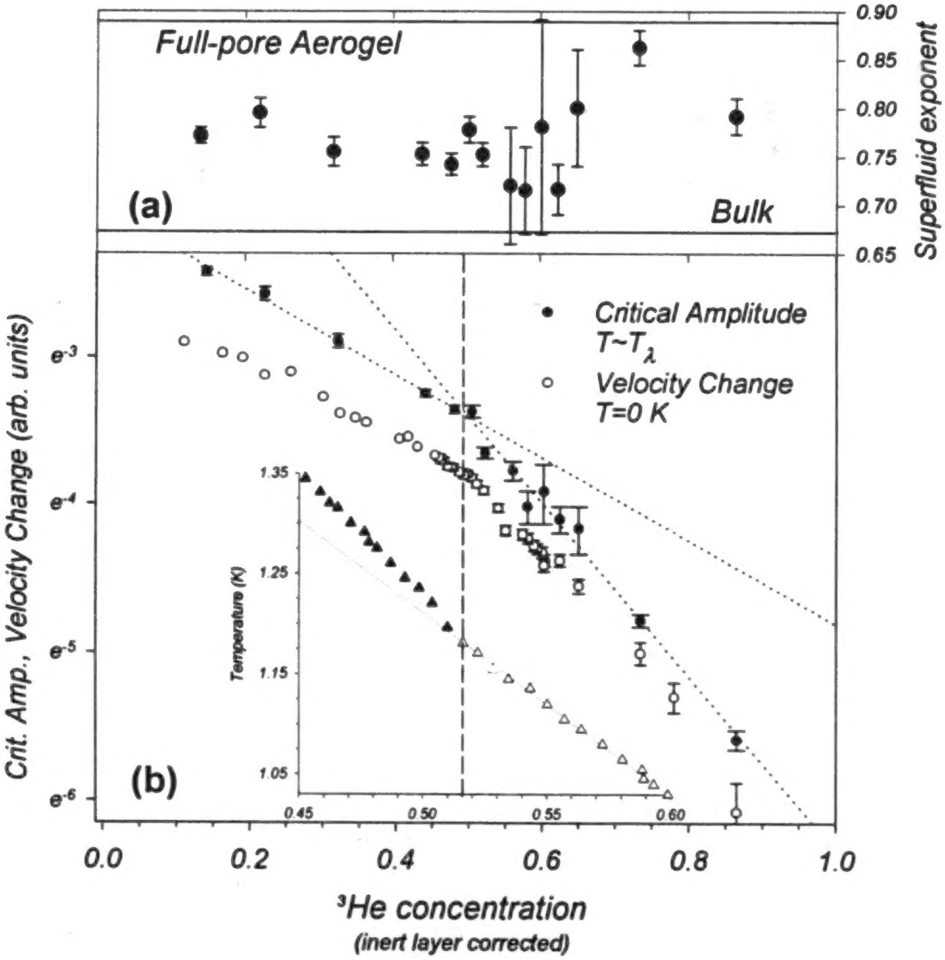

Figure 5.6.2.2. (a) The superfluid critical exponent (upper right scale, triangles) and (b) critical amplitude (filled) and velocity change (at T=0) (open circles). Inset shows location of kink in lambda line for comparison. Note the change in concentration scales.

semi-log plot there are two linear regimes that form a kink which coincides with the kink in the lambda line of the phase diagram (inset).

Figure 5.6.2.2 has the following implications. First, the absence of any systematic change in the exponent suggests there is no qualitative change in the critical behavior of the mixtures. Second, independent of their exact relationship to the tortuostiy, the kink in these two quantities suggest that the discrepancy between α_f and α_m at high X* is not due to a systematic error in the background subtraction. Third, the fact that the kinks in A_o and $\Delta v/vo(T=0\ K)$ and $T_\lambda(X^*)$ all coincide strongly suggests a change in the morphology of the superfluid at that concentration.

The two regimes of behavior in the decoupling of the superfluid suggest a crossover of behavior. For concentrations below X*~0.5 the difference between α_m and α_f is described well by additional coupling to the superfluid by ^{3}He atoms. However, for X*>0.5 this description is inadequate to describe the decrease in decoupling which is seen both near T_λ (where $m_3^*\sim m_3$) and at T=0 K (where m_3^* is maximized). There are two possibilities for this decrease in decoupling. The arrangement of the isotopes is such that either ^{4}He atoms are prevented from participating in the superfluid, which is equivalent to increasing inert layer, or there is additional coupling to the superfluid.

5.6.3 Discussion

We have shown that the tortuosities of mixtures and films differ significantly. While α_f increases smoothly across the entire range of X*, the mixtures show two regions of linearity, with a kink in α_m occurring at X*~0.5. This kink in the tortuosity corresponds with that seen in the lambda line in the T-X* plane. We consider three possibilities for these effects. First, in mixtures the ^{3}He contributes an effective mass, m_3^*, to the density and increases the apparent tortuosity. In this case, the tortuosity is due to the inertial coupling to the superfluid by "pushing" of the pore walls *plus* the inertial coupling due to the backflow created by a ^{3}He atom moving through the superfluid helium. A second possibility is that the inert layer, n_c, which we have assumed to be 427 µmol, is different in mixtures. McQueeney et al. found that 12 monolayers of ^{3}He atop ^{4}He films effectively increased the inert layer by approximately 20% [71]. As we need to know n_c in order determine the amount of "active" ^{4}He, any changes in it may have a considerable effect on the tortuosity calculation, particularly at high X*. The third possibility is that ^{4}He is localized at the surface of the aerogel and the ^{3}He increases the tortuosity by effectively decreasing the porosity of the aerogel. This description is complicated by the fact that the effective mass contribution due to ^{3}He at the surface of ^{4}He is approximately half that for a fully immersed ^{3}He atom, $m_{3s}^*\sim 1.4m_3$ [79]. In aerogels there may be large interfacial surface areas where this distinction is important, but the complexity of the aerogel structures makes it impossible to calculate such effects.

In bulk mixtures at T=0 the separated ^{4}He rich phase has a ^{3}He concentration X~0.064 and we have seen that ^{3}He moving through superfluid ^{4}He effectively increases the tortuosity by inertial coupling via superfluid backflow. As was shown in Fig. 5.6.1.2, α_m is larger than that of the pure ^{4}He film. We examine the possibility that this extra tortuosity is due to inertial coupling at T=0 by residual ^{3}He in the ^{4}He-rich phase. Recall for the background subtraction method the tortuosity is given by

$$\Delta_3 \approx \frac{(n_4-n_c)m_4}{2(m_a+n_3m_3+n_4m_4)\alpha} \qquad (5.6.3.1)$$

Assuming a residual ^{3}He concentration (X_{res}) exists in the ^{4}He rich phase and including the decrease in the velocity change due to the effective mass difference (m_3^*-m_3) between ^{3}He atoms in the superfluid and in the normal fluid, the velocity change due to decoupling can be written

$$\frac{1}{\alpha_f} = \frac{1}{\alpha_m} + \frac{m_3^*-m_3}{m_4}\left(\frac{X_{res}}{1-X_{res}}\right) \qquad (5.6.3.2)$$

The second term in the brackets is the number of residual ^{3}He atoms in the superfluid phase which is assumed to be comprised of all the active ^{4}He. Since the tortuosity of helium films is known, we can calculate the difference between the tortuosities of the pure films and of the mixtures containing a residual amount of ^{3}He. Denoting the mixture tortuosity as α_m, calculated via eqn. (5.6.2.1), and solving for X_{res}

$$X_{res} = \frac{\frac{m_4}{m_3^*-m_3}\delta}{1+\frac{m_4}{m_3^*-m_3}\delta} \qquad (5.6.3.3)$$

where $\delta = (1/\alpha_f - 1/\alpha_m)$. The fruits of this labor are shown in Fig. 5.6.3.1; the vertical axis is the residual concentration of ^{3}He in the superfluid at T=0 K, as calculated by eqn. (5.6.3.3), and the horizontal axis is the overall ^{3}He concentration, X*. While there is scatter in the data points the residual ^{3}He concentration is about 10%, as expected from the bulk phase diagram at our base temperature of 200 mK. The calculation is limited to the low X* side where there is a systematic offset between the mixture and film tortuosities. For X*>0.5 there may still be ^{3}He dissolved in ^{4}He, but we expect less since the larger zero point energy will tend to keep ^{3}He away from the aerogel surfaces where the ^{4}He rich phase resides. The curved interface between the phases also increases the chemical potential of ^{3}He atoms dissolved in the ^{4}He-rich phase and would also reduce the ^{3}He residual concentration of thin superfluid films. For these reasons we believe the sharp rise in the tortuosity for X*>0.5 is dominated by other effects.

Although the similar behavior between A_o and the change in velocity at T=0 suggests that a systematic error in the background subtraction is not responsible for the kink in the mixture tortuosity α_m at X*=0.5, a concentration dependent inert layer could

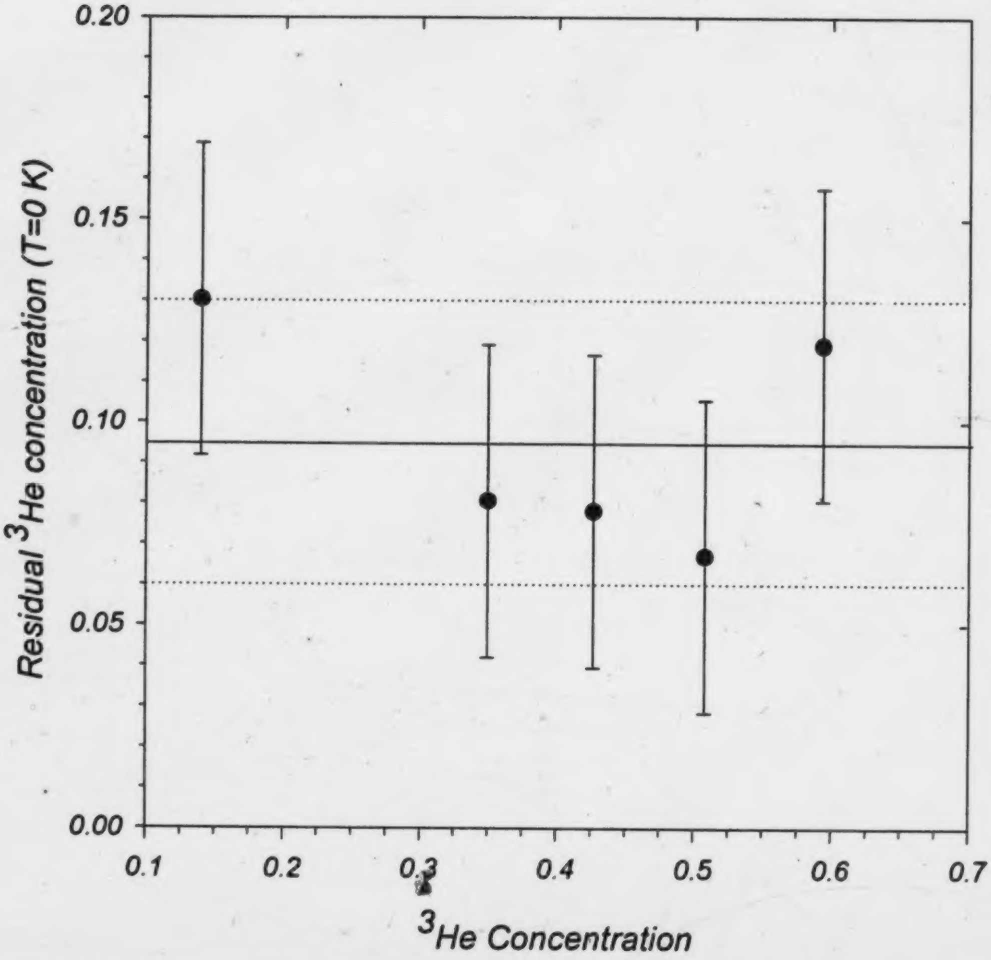

Figure 5.6.3.1. The residual ^{3}He concentration in the ^{4}He-rich phase at T=0 K.

change both quantities appreciably. McQueeney et al. found that 12 overlayers of ^{3}He effectively increased the inert layer by 20% over that measured for pure ^{4}He films. The effect of assuming a 20% increase beyond our measured film inert layer (n_c=427 becomes 515 μmol) is shown in Fig. 5.6.3.2. The open circles are the new calculations of the mixture tortuosities; the film tortuosities are again shown for reference. The modified inert layer (515 μmol) has been used to calculate both the (inert layer corrected) concentration X* and the tortuosity; the net effect of this correction is to decrease α_m and increase X*, particularly for mixtures with large X*. Apart from this, the curve is qualitatively unchanged. A kink is still found at X~0.5, and on either side α_m is roughly linear.

Continuing with the comparison of A_o and $\Delta v/v_o(T=0)$, the similar behavior for X*>0.5 is a strong indication that, while a 10% residual amount of ^{3}He may be present, residual amounts of ^{3}He diluted in the ^{4}He are not the cause for the anomalously high tortuosities in this concentration range. We consider now the possibility of the ^{3}He acting to effectively decrease the porosity of the system. Bernard and Williams examined how the tortuosity varied with porosity in sintered ceramics and reported that as the media became less porous the tortuosity increased dramatically [65]. An equivalent porosity (ϕ_{eq}) can be calculated by determining the pore volume not occupied by either ^{3}He or aerogel

$$\phi_{eq} = \phi - \frac{1}{V_a}\frac{Xn_4}{1-X}v_3 \qquad (5.6.3.4)$$

where X and n_4 are not corrected for the inert layer, V_a is the aerogel volume (0.1 cc) and v_3 is the molar volume of ^{3}He. Equation (5.6.3.4) predicts an equivalent porosity for X*=0.86 of ϕ_{eq}=0.27. Table 5.6.3.1 displays calculated equivalent porosities and the corresponding tortuosities for a number of the highest ^{3}He concentration mixtures. The mixture tortuosities for both inert layers have been presented in Table 5.6.3.1.

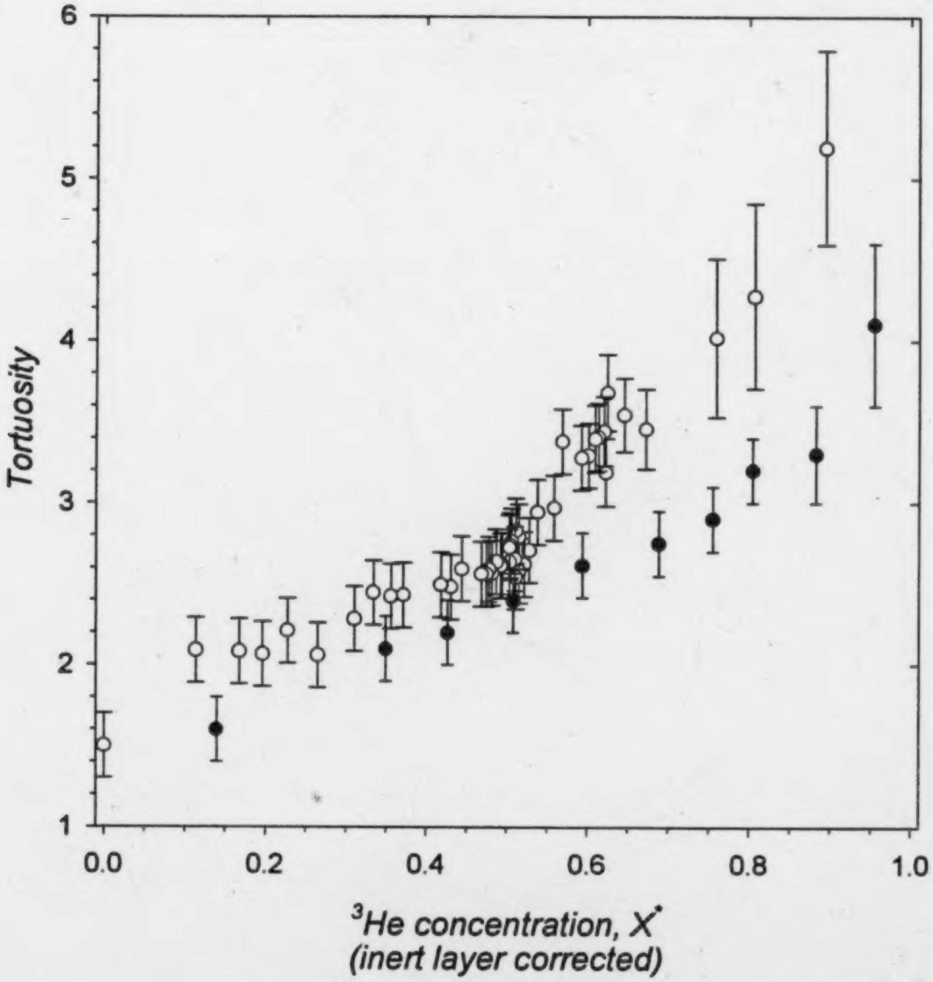

Figure 5.6.3.2. The tortuosity of helium mixtures (open circles) and pure helium films (filled circles) as a function of inert layer corrected ^{3}He concentration, X^*. The mixture data have been calculated using n_c=515 μmol, but the film data have not. Note the change in scale from Fig. 5.6.1.2.

While Bernard et al. measured both the 2-D and 3-D tortuosity [65], for the porosity range examined here they are the same. Note the values of the tortuosity determined by Bernard et al. of the first two mixtures in Table 5.6.3.1 are in reasonable agreement with ^{4}He film measurements on Vycor, ϕ~30%, and found α~4 [44]. The tortuosity data for the helium mixtures is consistently higher than the values obtained by Bernard and Williams, perhaps due to failure to include the ^{4}He inert layer in the calculation of the equivalent porosity, or the value of the inert layer used in the calculation is too small.

X (uncorr.)	X*	n_4 (μmol)	ϕ_{eq}	tortuosity α_m (n_c=427, 515)	tortuosity (Bernard et al. [65])
0.69	0.86	724	27%	7.4, 5.2 ±0.5	4-8(?)
0.59	0.73	986	34%	5.5, 4.3 ±0.3	4-4.2
0.52	0.65	1150	40%	4.0, 3.4 ±0.2	2.9-3.1
0.41	0.51	1500	48%	3.0, 2.6 ±0.2	2.3-2.6

Table 5.6.3.1. Comparison of Equivalent Porosity to Tortuosity. The tortuosities using two values of the inert layer (427, 515 μmol) for an equivalent porosity are compared to the interpolated data of Bernard and Williams. The range of porosities in the data of Bernard et al. is due to differences in sample preparation.

As to the mechanism of decreasing the decoupling (increasing the tortuosity) when the porosity is decreased, one might consider that, compared to pure helium films, the interface between the ^{3}He-rich region far from the aerogel and the localized ^{4}He-rich regions is diffuse. This effectively increases the coupling to the ^{4}He either by an effective mass like mechanism or by effectively increasing the inert layer (decreasing the amount of superfluid ^{4}He).

5.6.4 Conclusion

We have shown that the tortuosities of mixtures are different from those of pure ^{4}He films. For mixtures with $X^*<0.5$, α_m is parallel but offset from the film tortuosity; the offset is consistent with a ^{4}He rich phase containing 10% ^{3}He, in agreement with bulk mixtues. In mixtures, there is a sharp increase in the tortuosity at $X^*=0.5$ which was also seen in measurements of the critical amplitude, ρ_{so}. There is no corresponding systematic change in the critical exponent, ζ. Assuming a larger inert layer coverage in mixtures reduces α_m, particularly in the high X^* region, but a kink is still found at $X^*=0.5$. This sudden change in tortuosity coincides with the kink in the superfluid phase transition line at $X^*\sim0.5$, $T=1.15$ K (Fig. 5.3.3) which indicates that the nature of the superfluid state in mixtures in 87% aerogel changes quite suddenly at this concentration.

Considering the ^{3}He to effectively decrease the porosity of the aerogel, the high tortuosities at high ^{3}He concentrations have been compared to tortuosity measurements in porous alumina as a function of porosity. The two systems were found to agree relatively well, but we point out that the analogy is somewhat tenuous as the geometries of the aerogel-^{3}He and porous alumina should be quite different. The analogy does allow a representative picture, although the increase in α_m is probably related to the interaction of ^{3}He with the superfluid as opposed to the geometrical tortuosity effects found in porous alumina.

5.7. Discussion

Before further discussion of the ultrasonic measurements, we compare the results above with torsional oscillator (TO) and heat capacity measurements on 87% aerogel made at Penn State.

5.7.1. Torsional Oscillator and Heat Capacity Measurements

The Pennsylvania State University group of M.H.W. Chan and coworkers have made some torsional oscillator and heat capacity measurements on helium mixtures contained in aerogels with the same porosity (87%) as that used in the ultrasonic measurements reported in this thesis; in fact the torsional oscillator and ultrasonic measurements were made on samples cut from the same batch. Figure 5.7.1.1 shows the T-X diagram from their torsional oscillator (TO) measurements which is in good agreement with the one derived from ultrasonic measurements; the TO phase diagram corresponds to the corrected concentration and so should be compared to Fig. 5.3.2. The open circles are the superfluid decoupling transition and the filled circles are phase separation (identified from a sudden decrease in the dissipation). TO data show a steeper approach of the phase separation curve towards the superfluid line than the ultrasonic measurements, but that may be due to selection of the specific signature used to identify T_s. There may also be a slight kink where phase separation approaches the superfluid line but there are not enough data to be sure. The TO data are also shifted to higher concentrations compared with the ultrasonic data, probably due to differences in how the concentrations are corrected.

We also briefly discuss the results of heat capacity measurements made by N. Mulders et al. on a similar porosity aerogel [80]. The AC heat capacity technique is identical with that used to probe mixtures in 98% porosity aerogel. The results for ^{3}He concentrations (corrected for the inert layer) $0.4<X^*<1$ are displayed in Figs. 5.7.1.2 and 5.7.1.3. For $X^*=0.4$ (the open symbols connected by a line in Fig. 5.7.1.2) a heat capacity peak is visible at the superfluid transition ~1.3 K. Phase separation occurs in this mixture at a lower temperature, as indicated by the increase in heat capacity at 0.85 K. Increasing X^* moves the lambda peak to lower temperatures and the phase separation to higher temperatures. At $X^*\sim0.5$ the increase in heat capacity becomes a “shoulder” on the low temperature side of the lambda peak. As with the ultrasonic velocity data, the

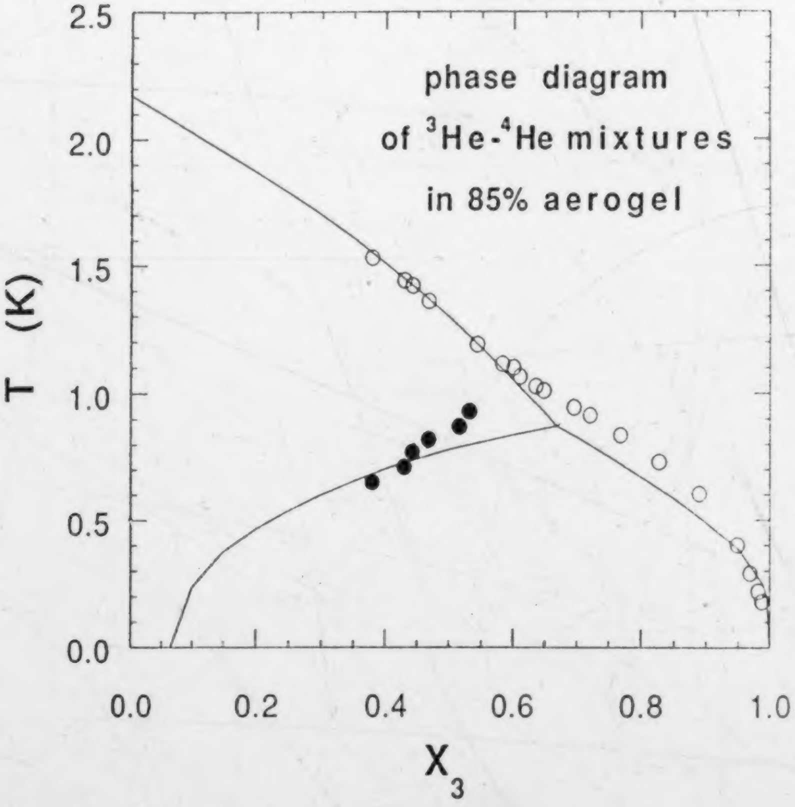

Figure 5.7.1.1. Phase diagram of helium mixtures in 85% aerogel. X_3 is the inert layer corrected concentration. Data courtesy of M. Chan.

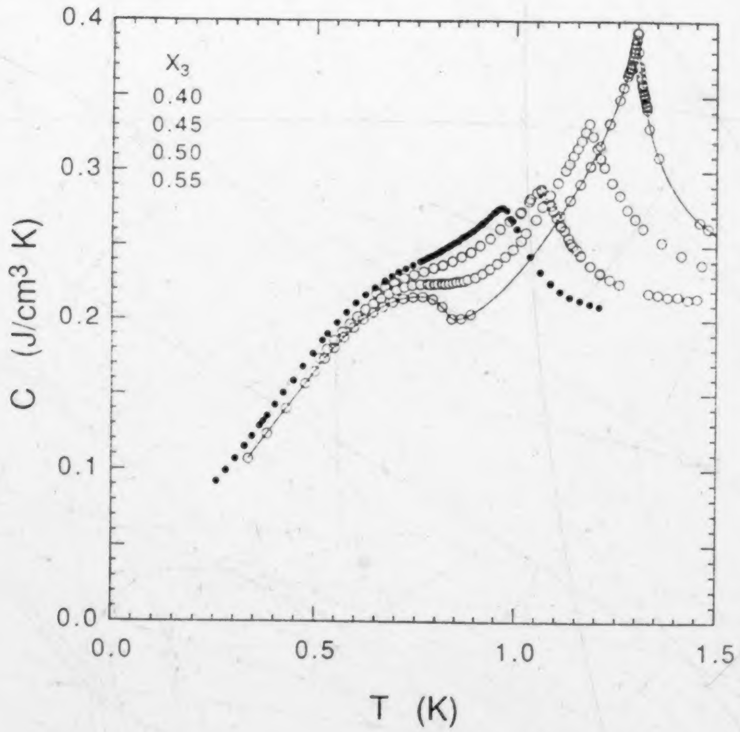

Figure 5.7.1.2. Heat Capacity of helium mixtures in 85% aerogel. X_3 = 0.40, 0.45, 0.50, 0.55 is the inert layer corrected concentration. Data courtesy of M. Chan.

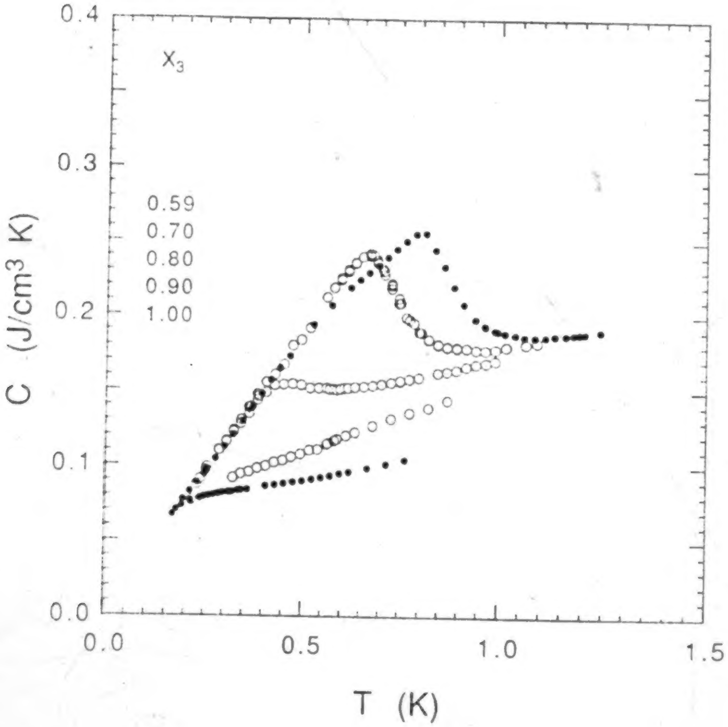

Figure 5.7.1.3. Heat Capacity of helium mixtures in 85% aerogel. X_3= 0.59, 0.70, 0.80, 0.90, 1.0 is the inert layer corrected concentration. Data courtesy of M. Chan.

characteristic feature identifying phase separation disappears at a concentration between $X^*=0.45$ and 0.55. Higher concentration data are shown in Fig. 5.7.13. The upper most curve is for a concentration of $X^*=0.59$ and shows only a single broad peak at about 0.8 K. At higher ^{3}He concentrations this peak shifts to lower temperatures and gradually disappears. This behavior is in contrast to the sharp heat capacity jump seen at the phase separation transition in bulk mixtures.

In agreement with the ultrasonic measurements presented here, the torsional oscillator and heat capacity techniques find that ^{4}He-rich mixtures display twotransitions, but only one transition is found in ^{3}He-rich mixtures.

5.7.2 Capillary Condensation and Higher Porosity Aerogel

Initially, it was suggested that the 98% aerogel suppressed phase separation at high X enabling the existence of a new homogeneous superfluid ^{3}He-rich phase [16]. This interpretation suggested that the presence of aerogel allowed a significant amount of ^{4}He to remain dissolved in ^{3}He at low temperatures so that a ^{3}He rich mixture could become superfluid without phase separating. This interpretation was supported by density functional calculations which predicted mixtures might be stabilized near a pore wall [22]. In a different theoretical approach, however, Falicov and Berker assumed that, based on zero point energy arguments, ^{4}He was preferentially adsorbed on the aerogel surface [23]. They "built" an aerogel-like structure into their BEG Ising model lattice and modeled it as a source of random chemical potential difference between the isotopes which simply means that ^{4}He prefers some aerogel sites to others. Using Monte Carlo methods they found a phase diagram very similar to the experimental one for 98% aerogel. In their model, superfluidity at low ^{4}He concentrations (high X) occurs as the ^{4}He atoms concentrate near the aerogel strands, much like the film-like behavior suggested by ultrasonic measurements [66]. Path integral Monte-Carlo calculations of bulk helium mixtures also indicated that the interface between the two phases was large

~10Å at T=0 [69].

These theoretical results, combined with measurements on different aerogel porosities have led to the following explanation of the detached phase separation line in higher porosity aerogel (98 and 99.5%). Mulders et al. [51] suggested that the detachment of the phase separation and superfluid transition lines at high X* was possibly due 'capillary condensation' of the ^{4}He film into superfluid domains connected by a diffuse ^{3}He-^{4}He interface [69]. That is, the coexistence boundary corresponds to creation of ^{4}He rich domains by the aggregation of ^{4}He formerly localized near the silica strands. Initially, at $T>T_s$, a concentration gradient exists in the mixture with ^{4}He atoms localized near the aerogel surface. However, there is no well-defined interface separating the ^{4}He film from the ^{3}He-rich liquid, effectively increasing the film thickness. This thick interface may also be responsible for the 3-D-like superfluidity. Continuing with the film description, as the mixture is cooled, it becomes superfluid, and then at a lower temperature T_s, ^{4}He-rich domains are created through "capillary condensation" of neighboring silica strands. In liquid vapor systems at constant pressure, capillary condensation results in hysteresis in the isobar on thermal cycling. For 98% porous aerogel, the condensation of the first region would occur at a ^{4}He concentration of 20%.

The idea of capillary condensation in mixtures can be compared to that seen in liquid-vapor adsorption isotherm data. With the large surface area of the areogel (~1000 m^2/g), then at T=0 K, as ^{4}He is added to ^{3}He one would expect the ^{4}He to be localized at the silica surface, based on the lower zero point motion of ^{4}He, and the ^{3}He to occupy the pore centers. This kind of layered phase separation was used to describe a series of third sound measurements in mixtures contained on a flat substrate [73]. When more ^{4}He is added at T=0 K, eventually a point is reached where capillary condensation of the ^{4}He rich phase occurs, in analogy with liquid-vapor isotherms on porous materials. For a 98% aerogel sample phase separation required 20% ^{4}He (X=0.8) even at T~0. Using bulk molar volumes, for X=0.8 means the ^{4}He occupies only 15% of the entire aerogel volume which is comparable to the filling at which capillary condensation begins in a ^{4}He liquid-vapor isotherm at 2.4 K [64]. Furthermore, capillary condensation is described by the Kelvin equation which depends on the ratio of surface tension to temperature (σ/T) (Section 2.3). Even though the surface tension in mixtures (σ_{34}) is lower than the liquid-vapor surface tension, the ratios σ/T are comparable (in the pure ^{4}He film case $\sigma_{lv}/T\sim$ (0.26 dynes/cm/2.5 K) [74]; for mixtures $\sigma_{34}/T \sim$ (0.022 dyne/cm / 0.2 K) [75]) which suggests a similar amount of ^{4}He (or at least comparable chemical potential) is required at $T=0.2$ K for the onset of capillary condensation in mixtures, i.e. a ^{4}He concentration of 20% as seen in experiment. Also more ^{4}He would be required for capillary condensation at higher temperatures, since the surface tension decreases, in agreement with the mixture phase diagram results. The argument becomes less clear as a critical or tricritical point is approached as the surface tension and therefore capillary condensation, should vanish.

Further experimental corroboration comes from simultaneous measurements of the concentration and torsional oscillator period in a low temperature experiment (~2 mK) designed to measure the onset of superfluidity in ^{3}He in 98% porous aerogel [76]. Measuring the concentration and the amount of decoupling allowed the tortuosity to be calculated and it was found to depend strongly on the history of the mixture. In high porosity materials the 2-D and 3-D tortuosities can be quite different, so hysteresis in the tortuosity implies a rearrangement of the superfluid in the aerogel. In this case, the ^{4}He might begin as a film with a 2-D tortuosity (high), but on thermal cycling, capillary condense to form bridges and three-dimensional connected regions resulting in a 3-D tortuosity.

The capillary condensation idea has also recently been tested in lower porosity (95%) aerogel [77]. Torsional oscillator measurements detected hysteresis just below the lambda line in high ^{3}He concentration mixtures. The onset of hysteresis just below T_λ is compatible with the idea of a ^{4}He film capillary condensing and driving phase separation since one would expect capillary condensation to occur for lower fillings in higher density aerogel where the strands are closer together. Furthermore, the authors suggest that for still lower porosity aerogel, capillary condensation precedes the superfluid transition at high ^{3}He concentrations. However, no hysteresis has been found above or below the superfluid transition in high ^{3}He concentration mixtures.

5.7.3. Summary

Based on the ultrasonic results and complementary measurements made elsewhere, we have developed the following picture for helium mixtures in 87% porosity aerogel. The difference in the zero point motions of the isotopes combined with the large surface area of the aerogel are the primary factors in deviations of the phase diagram of mixtures in 87% aerogel from bulk mixtures.

In the low ^{3}He concentration region the ^{3}He concentration is zero near the aerogel surface but increases as one moves away from the aerogel wall. The superfluid transition occurs in the nearly homogeneous mixture filling the pores, much as in bulk mixtures. The superfluid transition temperature, T_λ, parallels that found in bulk mixtures, it decreases as X^* increases. Ultrasonic measurements show superfluid decoupling and a critical attenuation peak at this transition. Phase separation in these ^{4}He rich mixtures occurs as a separate transition at a lower temperature T_s (slightly higher temperature than bulk mixtures). This transition is first order, as suggested by the hysteresis in the ultrasonic velocity and attenuation and by heat capacity measurements. It presumably occurs by nucleation of a ^{3}He-rich minority phase away from the aerogel surface. Phase separation draws ^{3}He out of the homogeneous superfluid and into a region of normal fluid. This appears in both torsional oscillator and ultrasonic data as a decrease in the effective density of the mixture (increase in velocity). The decrease occurs because the ^{3}He atoms in the superfluid contribute an effective mass (due to backflow) of $2.3m_3$ which decreases to the bare mass m_3 when the ^{3}He atoms move to the ^{3}He-rich normal phase. What is not fully understood is why the decrease in the effective density stops when the normal fluid reaches ~3.5% of the total fluid volume, but it is likely due to the structure of aerogel affecting the growth of the normal phase. This idea is supported by the fact that the onset of hysteresis, which presumably results from pinning of the interface by the aerogel matrix, coincides with the temperature at which the normal fluid reaches 3.5% of the fluid volume.

In the high ^{3}He concentration region, in contrast to higher porosity aerogel results, there is only one transition. This transition displays the characteristic features of a continuous transition to a superfluid state, similar to that of pure ^{4}He films, with a critical attenuation peak and a superfluid density exponent. However, the transition temperature follows the phase separation curve of the bulk mixture phase diagram. These results suggest the transition is driven by phase separation of ^{4}He onto the aerogel surface giving rise to film-like superfluid transition as the mixture is cooled. This is analogous to a superfluid transition in thick ^{4}He films adsorbed on porous media which occurs when the temperature is lowered and the film thickens due to condensation from the vapor, eventually becoming thick enough to support superfluidity. Furthermore, since ^{4}He in the mixtures has already concentrated at the aerogel surface and the interface is already been created, there is no nucleation barrier to overcome. This may account for the reversibility of the superfluid transition at high X^*. As discussed above, the "capillary condensation" model suggests that for lower porosity aerogel, due to the smaller pore size, capillary condensation may pre-empt the transition at high X^*; above the transition there is no hysteresis because the interface is not well defined.

The high porosity aerogels are comprised of silica strands that interconnect randomly forming a very tenuous structure. 87% porous aerogel is perhaps better described by "balls" of silica that may present a more uniform surface. The difference in structure is supported by TEM pictures of the different porosities and by the surface tortuosities; in 87% it is approximately 4.1 (similar to Vycor), while in 98% it is roughly twice that value [48]. The higher porosity aerogel exhibits a smooth, broad capillary condensation in 87% (again similar to Vycor), in contrast to the sharp change in 95 and 98% aerogel, possibly reflecting a change in the van der Waals potential of the aerogel. Since the van der Waals attraction is due to an electromagnetic interaction, the geometry of the substrate is important in determination of the overall strength. Since ^{4}He localized at the aerogel surface is an important factor in the capillary condensation description, the connectivity of the aerogel strands likely plays an important role in the transition found at low temperatures and high ^{3}He concentrations.

At intermediate concentrations, the superfluid transition line in the 87% aerogel has a kink at X_{tr}~0.5, T_{tr}=1.15 K. As in bulk mixtures, the phase transition curves approach this point linearly from high and low temperatures. At this concentration there is no signature for phase separation, but, since our measurement technique is sensitive to changes in density, this null result would be expected at a (tri)critical point. The critical attenuation peaks evolve smoothly through the critical concentration. However, the tortuosity and critical amplitudes show distinct changes in behavior at X*~0.5. Below this concentration, where the phase diagram is almost identical to bulk, the tortuosity indicates that, as in bulk, at low temperatures the phase separation is not complete but that the ^{4}He rich phase contains ~10% ^{3}He. The increase in tortuosity above X*~0.5 is attributed to the film-like behavior of the ^{4}He-rich phase, but the large values of tortuosity could also be a result of a ^{4}He inert layer which increases with ^{3}He concentration, coupled with some residual amount ^{3}He dissolved in the ^{4}He-rich phase. While it has not been possible to directly measure the phase separation temperatures for X*~X_{tr}, the kinks in the lambda line and in the tortuosity suggest the phase separation line meets the lambda line at X*~0.5, T=1.15 K. From ultrasonic measurements, a tricritical point at X*=0.5, T=1.15 K would require a sudden jump in the phase separation curve; however, torsional oscillator measurements suggest that the phase separation line continues to higher temperatures; the difference probably depends on what signature is used to identify phase separation.

Chapter 6
Summary

This thesis describes ultrasonic velocity and attenuation measurements on helium mixtures confined in an 87% porous aerogel. The aerogel sample was encapsulated with epoxy to minimize contact with bulk mixtures (liquid and vapor). For low ^{3}He concentrations, both the velocity and attenuation measurements were shown to be sensitive to the superfluid and phase separation transitions. Superfluidity was associated with a sharp rise in the velocity at T_λ, due to decoupling of the superfluid fraction, and also with a critical attenuation peak. A peak in attenuation, at the superfluid transition is indicative of a continuous transition. A superfluid density critical exponent was also found for this transition; in pure ^{4}He-filled pores it was ζ=0.89, whereas in mixtures smaller values were found, ζ~0.75. For ^{3}He concentrations $X^*>0.08$, a separate phase separation transition occurred at a temperature, T_s, identified from a "jump" in the velocity. At a temperature slightly below T_s, this transition resulted in hysteresis in both the ultrasonic attenuation and velocity.

Using these markers, the phase diagram for helium mixtures in an 87% porosity aerogel was determined. This diagram was then corrected for the ^{4}He inert layer, as obtained by extrapolation of the superfluid transition temperature to T=0 K for a series of pure ^{4}He films. The resulting phase diagram was similar to that found in bulk helium mixtures. For low ^{3}He concentrations, the superfluid and phase separation transition temperatures were similar to those in bulk mixtures. At an inert layer corrected concentration of X*~0.5 however, the phase separation signatures disappeared, while the markers for the superfluid transition (increase in velocity and attenuation peak) evolved smoothly to lower temperatures at higher X*.

Since the ultrasonic velocity measurement is sensitive primarily to changes in density, this "washing out" of the phase separation transition might be expected on approaching a coexistence critical point (or tricritical point). However, the lambda line $T_\lambda(X^*)$ displays a kink at X*~0.53 but at a temperature ~0.25 K higher than the last signature of phase separation. If this kink marks the tricritical point for mixtures in 87% aerogel then the ultrasonically determined phase separation line would have to rise more steeply to meet the lambda line at the kink. However, torsional oscillator measurements do indicate the phase separation line has a steeper slope; this difference may be due to the selection of different markers to identify phase separation. Other than this discrepancy, the two phase diagrams are in good agreement.

At concentrations X*>0.5, the superfluid transition continues to low temperatures, in agreement with measurements on mixtures in 98% porous aerogel. However, in the 87% porosity aerogel, only one transition is found at high X*, in contrast to the two transitions seen in 98%, and more recently in 99.5% and 95% aerogels [16, 77]. The tortuosities were determined from the ultrasonic measurements and also showed a sudden change at X*~0.5, suggesting a change in morphology of the superfluid at that concentration.

In an attempt to more fully understand the aerogel-mixture system we have paid close attention to the shape and changes in the velocity curves. There are two dominating effects of phase separation in ^{4}He rich mixtures. The first is a decrease in the overall superfluid fraction when ^{4}He atoms move from the dilute superfluid phase into the newly formed ^{3}He-rich normal phase. The second is a decrease in the ^{3}He mass contribution to the effective density when ^{3}He atoms move into the normal phase. By analyzing the velocity changes at phase separation, an effective mass of 2.5±0.2 g/mol was found, in agreement with measurements and calculations in bulk mixtures.

The hysteresis which appears below T_s at low X^* is ascribed to the ^{3}He-rich phase nucleating in the pores, creating an interface which then becomes pinned by the aerogel matrix. For low ^{3}He concentrations, the regions of normal phase appear at the center of the pores but eventually grow until they reach the aerogel matrix and effectively pin the interface. On warming, the interface must recede, but a different interface distribution causes hysteresis. The size of the hysteresis loop decreases at very low ^{3}He concentrations since the ^{3}He-rich phase constitutes a much smaller fraction of the total volume.

In an attempt to understand the superfluid transition for high ^{3}He concentrations, comparisons were made to pure ^{4}He films, which also exhibit a superfluid transition. The transition temperatures increased with ^{4}He content much faster for films than for the mixtures and the increase in the superfluid density was also quite different. These differences imply that above the transition the mixtures are not separated into a *pure* ^{4}He film localized at the aerogel surface and a pure ^{3}He liquid filling the rest of the pores. That is, the difference between the zero point energies is not so great as to keep all the ^{4}He film localized at the surface at all temperatures but a concentration gradient exists with ^{4}He localized at the aerogel surface.

The superfluid fraction was also compared to a model of bulk mixture phase separation. This model was found to be inadequate to describe the temperature dependence of the measured superfluid fraction which showed a much faster increase in

ρ_s near T_λ. Furthermore, in high X^* mixtures, phase separation would occur via nucleation and growth of a superfluid minority phase well away from the critical region at T_λ (at least for concentrations greater than X_{tr}), so no critical attenuation peak would be expected in a bulk-like phase separation, in contrast to those seen in ultrasonic measurements. The transition at high X^* thus includes aspects of both a film superfluid transition (critical behavior, attenuation peak) and of phase separation (the transition temperature follows that of the bulk high X^* phase separation line).

This duality of behavior leads to the following picture of the transition for high ^{3}He concentration mixtures. In 87% aerogel the mixture is nearly homogenous at high temperatures, except near the aerogel surface where the ^{4}He is concentrated due to its lower zero point motion. As the sample is cooled toward bulk phase separation, more ^{4}He condenses onto the strands, rapidly thickening the ^{4}He-rich film. It becomes thick enough to support superfluidity close to the bulk phase separation temperature. There is no hysteresis possibly because the interface already exists at the transition. The same thing occurs in higher porosity aerogel, but in those systems the superfluid ^{4}He film at the aerogel surface also undergoes "capillary condensation" at some temperature $T<T_\lambda$, resulting in hysteresis. In recent measurements on 95% porous aerogel, the onset of hysteresis was found to occur just below the superfluid transition, so in our even higher density 87% aerogel, capillary condensation may occur at or above the superfluid transition. We would expect such a capillary condensed system to exhibit a lower tortuosity since ^{4}He would form bridges between regions of ^{4}He films. This, however is not reflected in the measured tortuosities which are notably larger than those of films containing the same amount of ^{4}He.

REFERENCES

1. H. Kamerlingh Onnes, Leiden Comm. **108**, Prc. Sect. Sci. K. Ned. Akad. Wet. 11, 168 (1908).
2. The Properties of Liquid and Solid Helium. J. Wilks, Claredon Press, 1967.
3. F. London, Nature, Lond. **141**, 643(1938).
4. S.N. Bose, Z. Phys. **26**, 178(1924).
5. A. Einstein, sitzber. Kgl. Preuss. Akad. Wiss., 261(1924); 3(1925).
6. Progress in LowTemperature Physics Vol. XIII, F. Gasparini et al. Ed. D.F. Brewer,North Holland, 1992, p. 3.
7. S. Mehta, W.Y. Yu, A. Pe[illegible]ou, J. Lipa, D. Bishop, F.M. Gasparini, Czech. J. Phys. **46 S1**, 133(1996).
8. Eric B. Molz, M.Sc. Thesis (unpublished), University of Delaware (1991).
9. Eric B. Molz, Ph.D.. Thesis (unpublished), University of Alberta (1995).
10. M. Schindler, A. Dertinger, Y. Kondo and F. Pobell, Phys. Rev. B53, 11451(1996); M. Paetkau and J. Beamish, Bull. Am. Phys. Soc. **42**, 673(1997).
11. G.G. Litvan, J. Colloid and Interface Sci. **38**, 75(1972).
12. G. Beaudoin, P. Haljan, M. Paetkau, J.R. Beamish, J. Low Temp. Phys. **46**, 153(1996).
13. P.G. de Gennes, J. Phys. Chem. **88**, 6469(1984).
14. Z. Zhuang, A.G. Casielles, D.S. Cannell, Phys. Rev. Lett. 77, 2969(1996).
15. A.P.Y. Wong and M.H.W. Chan, Phys. Rev. Lett. **65**, 2567(1990).
16. S.B. Kim, J. Ma, and M.H.W. Chan, Phys. Rev. Lett. **71**, 2268(1993); J. Ma, S.Kim, M.H.W. Chan, Physica B **197**, 249(1994).
17. G.K.S. Wong, P.A.Crowell, H.A.Cho, and J.D. Reppy, Phys. Rev. Lett. **65**, 2410(1990).
18. M.H.W. Chan, K.I. Blum, S.Q. Murphy, G.K.S. Wong, and J.D. Reppy, Phys. Rev. Lett. **61**, 1950(1988).

19. E. H. Graf, D. M. Lee, and J.D. Reppy, Phys. Rev. Lett. **19**, 417(1967).

20. E.M. Ifft, D.O. Edwards, R.J.Sarwinski, and M.M. Skertic, Phys. Rev. Lett.**19**, 831(1967); D.O. Edwards, E.M. Ifft, and R.E. Sarwinski, Phys. Rev. **177**, 380(1969).

21. C. Ebner and D.O Edwards, Phys. Rep. **2C**, 77(1970).

22. L. Pricaupenko and J. Treiner, Phys. Rev. Lett. **74**, 430(1995).

23. A. Falicov and A. Nihat Berker, J. Low. Temp. Phys. **107**, 51(1997);
A. Falicov and A. Nihat Berker, Phys. Rev. Lett. **76**, 4380(1996);
A. Nihat Berker, J. of Appl. Phys. **70**, 5941(1991);

24. K. Uzelac, A. Hasmay and R. Jullien, Phys. Rev. Lett. **74**, 422(1995).

25. A. Maritan, M. Cieplak, M. Swift, F. Toigo and J.R. Banavar, Phys. Rev. Lett. **69**, 221(1992).

26. J.R. Beamish and E.B. Molz, Bull. Am. Phys. Soc. **39**, 660(1994).

27. R.A. Ferrell, B. Mirhashem, J.K. Bhattacharjee, Phys. Rev. **B35**, 4662(1987);
R.A.Ferrell and J.K. Bhattacharjee, Phys. Lett. **86A**, 109 (1981).

28. D.B. Roe, G. Ruppeiner, and H. Meyer, J. Low Temp. Phys. **27**, 747(1977).

29. M.H.W. Chan, 21st Conference on Low Temperature Physics, Czech. J. Phys. **46 S6**, 2915(1996).

30. L. Tisza, Nature **141**, 913(1938).

31. E.L. Andronikashvili, Zh. Eksp. Teor. Fiz. **16**, 780(1946).

32. C.E. Chase, Phys. Rev. Lett. **2**, 197(1959).

33. K.E. Herzfeld and F.O. Rice, Phys. Rev. **31**, 691(1928).

34. J.G. Daunt and C.V. Heer, Phys. Rev. **79**, 46(1950).

35. F. Uehara, J. Low Temp. Phys. **24**, 769(1976).

36. R.P. Feynman, Phys. Rev. **94**, 262(1954).

37. Mixtures, E.A. Guggenheim, Oxford, Clarendon Press, 1952, p.29.

38. D.O. Edwards and J.G. Daunt, Phys. Rev. **124**, 640(1961).

39. For example see Equilibrium Statistical Physics, Michael Plischke and Birger Bergersen, Prentice Hall, 1989.

40. R.B. Griffiths, Phys. Rev. Lett. **24**, 715 (1970).

41. M. Blume and V.J. Emery and Robert B. Griffiths, Phys. Rev. **A4**, 1071(1971).

42. Sol-Gel Science, C. Jeffrey Brinker George W. Scherer, Academic Press 1990 p. 97.

43. S.S. Kistler, J. Phys. Chem. **36**, 52(1932).

44. Helium in Vycor: An Ultrasonic Study, Norbert Mulders, University of Deleware, unpublished (1990).

45. S. Brunauer, P.H. Emmett, E. Teller. J. Amer. Chem. Soc. **60**, 309 (1938).

46. D.H. Everett and J.M. Haynes, J. Colloid and Interface Sci. **38**, 125(1972).

47. J.D. Reppy, J. Low. Temp. Phys. **87**, 205(1992).

48. P.A. Crowell, J.D. Reppy, S. Mukherjee, J. Ma, M.H.W. Chan and D.W. Schaefer, Phys. Rev. **B51**, 12721(1995).

49. P.A. Crowell, F.W. Van Keuls and J.D. Reppy, Phys. Rev. **B55**, 12620(1997).

50. D. Finotello, K.A. Gillis, A. Wong, M.H.W. Chan, Phys. Rev. Lett. 61, 1954 (1988).

51. N. Mulders and M.H.W. Chan, Phys. Rev. Lett. **75**, 3705(1995).

52. D.S. Fisher, G.M. Grinstein and A. Khurana, Physics Today **56**, No. 12 (Dec. 1988).

53. K.L. Warner and J.R. Beamish, Phys. Rev. **B36**, 5698 (1987).

54. K. Warner and J.R. Beamish, Phys. Rev. **B50**, 15896(1994).

55. J.R. Beamish, unpublished.

56. S. Wang, C. Howald, and H. Meyer, J. Low Temp. Phys. **79**, 151(1990).

57. M.A. Biot, J. Acoust. Soc. Amer. **28**, 168(1956), 179(1956).

58. J.R. Beamish, A. Hikata, and C. Elbaum, Phys. Rev. **B27**, 5848(1983).

59. K.W. Taconis and R. De Bruyn Ouboter, Progress in Low Temperature Physics,Vol. IV, Ed. C.J. Gorter, North-Holland Publishing, 1964.

60. Xingwu Wang and Francis M. Gasparini, Phys. Rev. **B38**, 11245 (1988).

61. J.M. Kosterlitz and D.J. Thouless, J. Phys. **C7**, 715(1973).

62. P.A. Crowell, F.W. Van Keuls and J.D. Reppy, Phys. Rev. B55, 12620(1997).

63. D.J. Bishop, J.E. Berthold, J.M. Parpia, J.D. Reppy Phys. Rev. **B24**, 5047(1981).

64. M.H.W. Chan private communication

65. M. Bernard and G.A. Williams Phys. Rev. Lett. **67**, 2585(1991).

66. M. Paetkau and J. Beamish, J. Low Temp. Phys. **101**, 391(1995).

67. Ultrasonic Absorption, A.B. Bhatia, Oxford Press 1967.

68. J.G. Dash and R.D. Taylor, Phys. Rev. **107**, 1228(1957).

69. M. Boninsegni and S. Moroni, Phys. Rev. Lett. **78**, 1727(1997); M.

70. R.A. Sherlock and D.O. Edwards, Phys. Rev. **A8**, 2744 (1973).

71. D. McQueeny, G. Agnolet, and J.D. Reppy, Phys. Rev. Lett. **52**, 1325(1984).

72. Boninsegni and D.M.Ceperley, Phys. Rev. Lett. **74**, 2288(1995).

73. F.M. Ellis, R.B. Hallock, M.D. Miller, and R.A. Guyer, Phys. Rev. Lett. **46**, 1461(1981).

74. Helium and the Rare GasesRare gas elements or History,Occurrence, and Properties:Argon, the elements of the helium group Vol I. Ed. Gerhard A. Cook, Interscience Publishers, New York, 1961.

75. A. Sato, K. Ohishi, and M. Suzuki, J. Low Temp. Phys. **107**, 165(1997); A. Sato and M. Suzuki, J. Low Temp. Phys. **99**, 727(1995).

76. A. Golov and J.M. Parpia, in press.

77. J. Yoon and M.H.W. Chan, Phys. Rev. Lett., in press.

78. G.M. Zassenhaus, A. Tyler, and J.D. Reppy, Czech. J. Phys. **46 S1**, 147(1996).

79. D.O. Edwards and W. Saam in Progress in Low Temperature Physics Vol. VIIa, ed. D.F.Brewer (North-Holland, Amsterdam, 1978), p. 283.

80. D.J. Tulimieri, N. Mulders, M.H.W. Chan, Czech. J. Phys. **46-S1**, 199(1996).